Structural Studies of Amorphous Materials



Yu-Jen Chou

Department of Materials

St. Catherine's College

University of Oxford

A Thesis Submitted for the Degree of

Doctor of Philosophy

Hilary 2018

Abstract

Amorphous materials have attracted interest due to their unique properties as many common objects and industrially important components are made of amorphous materials. To understand their properties, building structure-property correlations is an important step. Typically, amorphous materials are investigated by X-ray or neutron diffraction, but due to the relatively large interaction volumes for both probes, these techniques are not suitable for studying materials with nanovolumes. In contrast, electron probes can be focused on specifically chosen nanoscale areas and data from electron diffraction patterns can be transformed into a reduced density function (RDF) which describes the distribution of nearest-neighbour distances at high precision.

In this thesis, using electron diffraction based RDF techniques I have studied the effects of various factors on the RDF. In addition, Density Functional Theory (DFT) simulations and Reverse Monte Carlo (RMC) refinements were performed to support the interpretation of the experimental RDF results.

Finally, two industrial important materials, bioactive glass and metallic glass, were examined. A possible structure-property correlation in bioactive glasses is proposed while an analytical RDF technique was developed for the construction of metallic glass models.

Statement of authorship

Parts of the thesis I am submitting are of a collaborative nature and the contributions that are not my own are detailed below.

eRDF Analysis software

The eRDF Analysis software used in the thesis was written by Dr Janaki Shanmugam.

Modelling software

The software for geometry optimisation, Fourier filtering, RMC refinement were written by Dr Konstantin Borisenko.

Chapter 3

Section 3.2: The software for the multislice calculations was written with the help of Dr Konstantin Borisenko.

Sections 3.3 to 3.5: Experiments on the JEOL Grand-ARM300F at the electron Physical Science Imaging Centre (ePSIC), Harwell Campus, were performed with the assistance of Dr Hidetaka Sawada, Dr Christopher Allen, Dr Emanuela Liberti and Dr Mohsen Danaie.

Chapter 4

Section 4.1: The bioactive glass samples were synthesized and bioactivity tests were performed by Prof Shao-Ju Shih and colleagues.

Section 4.2: The metallic glass samples were prepared by Dr Jefferson Bettini and colleagues.

Candidate's Signature: Date: 29/ 03/ 2018

Acknowledgements

First and foremost, I would like to thank my supervisors Professor Angus Kirkland and Dr Konstantin Borisenko for their continuous and generous support during the course of my DPhil study. They have spent a great deal of time working with me to form the scientist and person I am today. Angus has been a faithful source of wisdom, and Konstantin has helped me with countless discussions throughout the years.

I would like to thank our collaborators Professor Shao-Ju Shih and Dr Jefferson Bettini for providing the samples for this study and other forms of support, and I am indebted to all the members of the Electron Image Analysis group, Dr Hidetaka Sawada, Dr Christopher Allen, Dr Mohsen Danaie and Dr Emanuela Liberti for their assistance in various research problems. I am also thankful to many of my peers, Dr Janaki Shanmugam, Dr Chen Haung, Mr Aakash Varambhia, for their invaluable advice and discussions. I thank all my friends, Ayumi, Yujiro, Sewook, Bo-Shiuan, Ren-Jie, Wing, Yi-Sheng, Yung-Kang and more, for all your companions and the joyful moments throughout these years.

Last but not least, to my family, thank you for your endless support and encouragement.

Contents

Abstract i

Statement of authorship ii

Acknowledgements iii

Chapter 1 Introduction 1

1.1 Example Applications of Amorphous Materials 1

1.1.1 Optical Fibres 1

1.1.2 Random Access Memory 2

1.1.3 Transformer Cores 2

1.1.4 Biological Scaffolds 2

1.2 The Structure of Crystalline and Amorphous Materials 3

1.3 Characterisation of Amorphous Materials 4

1.3.1 Raman Spectroscopy 4

1.3.2 Nuclear Magnetic Resonance 5

1.3.3 Diffraction 7

Chapter 2 Reduced Density Function (RDF) Analysis 9

2.1 Scattering Theory and the Reduced Density Function 9

2.2 Comparison with X-ray and Neutron Diffraction 14

2.2.1 X-ray Diffraction 14

2.2.2 Neutron Diffraction 15

2.2.3 Electron Diffraction 16

2.3 The Historical Development of electron RDF Analysis 18

2.3.1 Energy Filtered Diffraction 18
2.3.2 Convergent Beam Diffraction 20
2.3.3 Multiple Scattering 23
2.3.4 RDF Analysis in Material Science 24
2.4 RDF Analysis of Amorphous Materials 25
2.4.1 Experimental RDF Analysis 25
2.4.1.1 Acquisitions of Diffraction Patterns 25
2.4.1.2 Calculation of the Calibration Factor 28
2.4.1.3 Background Fitting 33
2.4.2 Factors Affecting the RDF Calculation 37
2.4.2.1 Effect of the Calibration Factor on the RDF 37
2.4.2.2 Effect of Centre Location in a Diffraction Pattern on the RDF. 40
2.4.2.3 Effect of Data Range on the RDF 42
2.4.2.4 Effect of Chemical Composition on the RDF 46
2.4.2.5 Effect of a Damping Factor on the RDF 49
2.4.2.6 Summary 56
Chapter 3 Factors Affecting Experimental RDF Analysis 58
3.1 Experimental and Simulation Setup 58
3.1.1 RDF Acquisition 58
3.1.2 DFT Simulations 59
3.1.3 RMC Refinements 62
3.2 Effect of Sample Thickness on the RDF 69
3.3 Effect of Noise on the RDF 82

3.4 Effect of Coherence on the RDF 87
3.5 Effect of Dose on the RDF 99
3.6 Robustness of RDF Analysis 104
Chapter 4 Structural Analysis of Amorphous Materials 106
4.1 Bioactive Glasses 106
4.1.1 Introduction 106
4.1.1.1 Bioactivity 108
4.1.1.2 Synthetic methods 109
4.1.2 Structural Analysis of Bioactive Glasses 113
4.1.2.1 Experimental RDF Analysis of Bioactive Glasses 113
4.1.2.2 Simulated DFT Models and RMC Refinement of Bioactive Glasses 117
4.1.3 Structure-Property Correlations in Bioactive Glasses 121
4.2 Ti-Si Metallic Glasses 124
4.2.1 Introduction 124
4.2.1.1 Bulk Metallic Glasses 124
4.2.1.2 Thin Film Metallic Glasses 126
4.2.2 Structural Analysis of Ti-Si Metallic Glasses 128
4.2.2.1 Experimental RDF Analysis of Ti-Si Metallic Glasses 128
4.2.2.2 Simulated DFT Models of Ti-Si Metallic Glasses 135
4.2.2.3 Characterisation of the Oxidation Level 139
4.2.2.4 Construction of atomic models 144
4.3 Summary of Key Findings 152
4.3.1 Bioactive Glasses 152

4.3.2 Metallic Glasses 154

Chapter 5 Conclusions and Future Work 156

5.1 Conclusions 156

5.2 Future Work 158

References 159

Chapter 1 Introduction

1.1 Example Applications of Amorphous Materials

Many common objects and industrially important components are made of amorphous materials. Some typical examples are given in Table 1.1.1 below.

Table 1.1.1 Amorphous materials with industrial importance.

Type	Compositions	Application	Special properties
Oxide glass	SiO_2, GeO_2	Optical fibres	Transparency/ Purity
	SiO_2, CaO	Biological scaffold	Biocompatibility
Chalcogenide glass	$Ge_2Sb_2Te_5$	Random Access Memory	Photo-induced rapid phase transformation
Metallic glass	Au-Si, Fe-B	Transformer cores	Ferromagnetism/ Low power loss

1.1.1 Optical Fibres

An optical fibre is a flexible, transparent fibre made from silica glass or polymer with a diameter slightly thicker than that of a human hair used for transmitting optical signals. These fibres now often replace copper for transmitting the signals used in telecommunications. Optical fibres are immune to electromagnetic interference and thus, they can be used as a medium for telecommunications and computer networking and are especially advantageous for long-distance communications [1]. In addition, such fibres are also used for a variety of other applications, including sensors and lasers [2].

1.1.2 Random Access Memory

Chalcogenide glasses exhibit several non-linear optical effects such as photo-induced refraction and electro-induced permittivity modification [3, 4]. Some chalcogenide materials exhibit an amorphous to crystalline phase-change under thermal treatment where the two phases have different optical properties. This allows them to be used for encoding information in thin films which forms the basis of phase-change memory [5].

1.1.3 Transformer Cores

Transformer cores are typically iron-rich amorphous solids with compositions such as $Fe_{0.8}B_{0.2}$ and $Fe_{0.8}B_{0.1}Si_{0.1}$. These ferromagnetic glasses are mechanically hard materials, but they are magnetically soft, meaning that they can be easily magnetized by small magnetic fields. Hence these materials can be magnetically cycled with only a small energy loss. The disordered structure also gives a higher electrical resistance than conventional crystalline magnetic materials. The three attributes of ease of manufacture, magnetic softness, and high electrical resistance make these materials suitable for use in the magnetic cores of electrical power transformers [6].

1.1.4 Biological Scaffolds

An important application for amorphous materials is in the development of biocompatible structures. As an example, bioactive glasses and Apatite/Wollastonite glass ceramics have been shown to be to be biocompatible and biodegradable and have been studied extensively for use as implants [7, 8].

1.2 The Structure of Crystalline and Amorphous Materials

All solids can be categorised as either crystalline or amorphous which are differentiated by their atomic structure. Figure 1.2.1 illustrates the two dimensional arrangement of crystalline and amorphous structures [9], showing the essential difference in the order of atomic positions within the structure. Crystalline structures exhibit long-range order, also called translational periodicity, which gives rise to a regular lattice as indicated in Figure 1.2.1 (a). In contrast amorphous structures, as shown in Figure 1.2.1 (b), have no long-range order but may have short-range order. However, both crystalline and amorphous structures exhibit short-range and medium range order as a consequence of the chemical bonding between atoms.

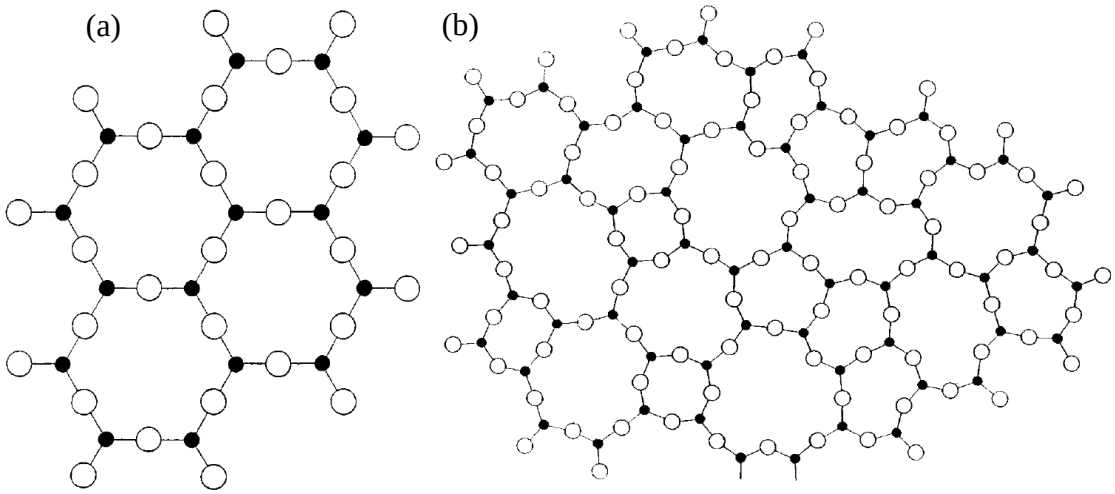


Figure 1.2.1 Atomic arrangements in (a) crystalline and (b) amorphous materials [9].

1.3 Characterisation of Amorphous Materials

The structures of amorphous materials are not necessarily “without a clear shape or form” due to the presence of short and medium range order. Investigation of the structure of amorphous materials is in general carried out using several methods of which diffraction (as used in this thesis) is the most common.

1.3.1 Raman Spectroscopy

Raman spectroscopy is a technique used to observe vibrational, rotational, and other low-frequency modes and is commonly used in chemistry to provide a structural fingerprint by which molecules can be identified [10]. The technique relies on inelastic scattering of laser light in the visible, near infrared, or near ultraviolet. The light interacts with phonons in the system which results in a shift of the energy of the photons that gives information about the modes in the system.

Figure 1.2.2 shows a typical Raman spectra of compositionally identical crystalline, fused quartz and a glass microscope slide [11]. Significant differences can be seen due to the presence or absence of long-range order. The spectrum of crystalline quartz consists of sharp peaks while fused quartz shows broad peaks with widths of up to several hundred wavenumbers.

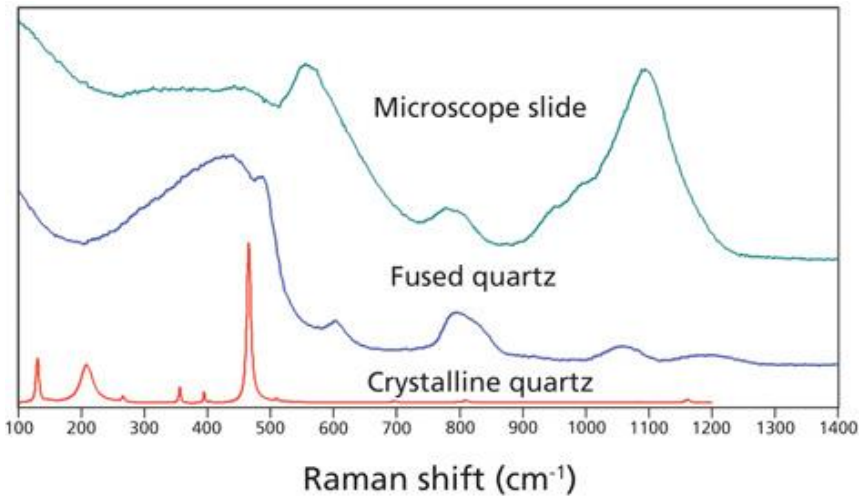


Figure 1.2.2 Raman spectra of crystalline, fused quartz and a glass microscope slide [11].

Although Raman spectra can be used to probe the vibrations of bonds in the material system which allows comparison between various specimens and confirmation of the amorphous state, the vibrational information is hard analyse quantitatively at a level sufficient to reconstruct the amorphous structure.

1.3.2 Nuclear Magnetic Resonance

Nuclear Magnetic Resonance (NMR) is a measurement based on the interaction of the nuclear magnetic moment with an external magnetic field. Importantly, however, the technique can only observe isotopes containing an odd number of protons (e.g. ^{1}H, ^{13}C, ^{29}Si) since nuclei with even numbers of protons have a total spin of zero.

Figure 1.2.3 shows two example ^{29}Si NMR spectra of (a) $Na_2O–SiO_2$ and (b) $K_2O–SiO_2$ glasses. Figure 1.2.3 (a) shows that the chemical shift of ^{29}Si with changes with increasing Na_2O content [12] and Figure 1.2.3 (b) shows quantitative analysis of Q^n specifications which indicates the level of bridging oxygen (see Figure 1.2.4). With increasing K_2O ratio, the level of bridging oxygen decreased from Q^4 (four bridging oxygens) to Q^1 (one bridging oxygen) [13].

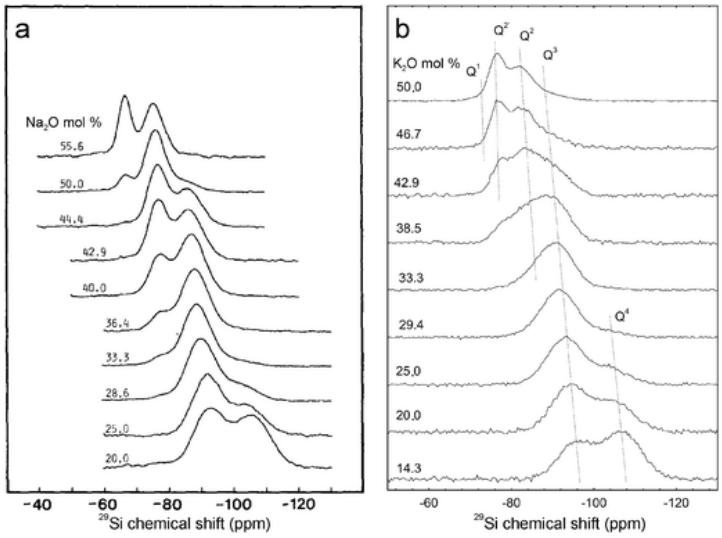


Figure 1.2.3 ^{29}Si NMR spectra recorded from (a) $Na_2O–SiO_2$ and (b) $K_2O–SiO_2$ glasses, revealing network re-polymerisation as the M_2O content decreases [12, 13].

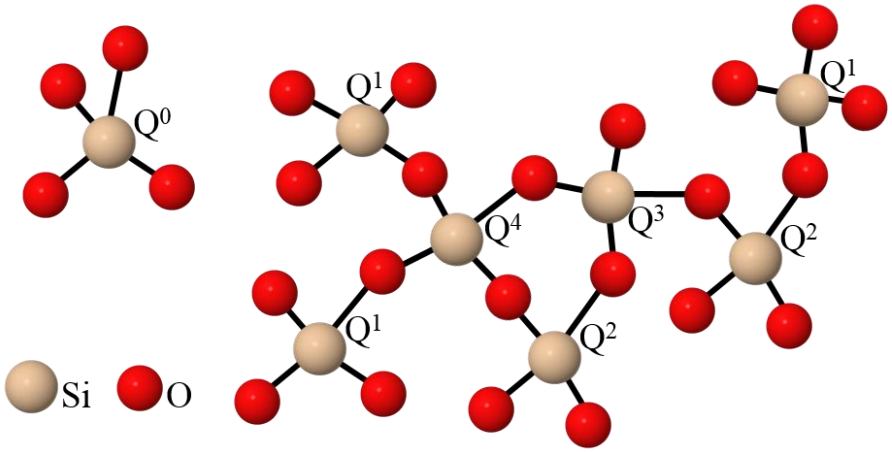


Figure 1.2.4 Q^n specification in the silicate chain structure.

Advantages of NMR are that it is a non-destructive technique with high sensitivity to small structural changes. However, elements with zero spin cannot be observed which limits its application.

1.3.3 Diffraction

Diffraction technique have been used extensively to determine the atomic structure of materials using X-rays, neutron and electrons. Figure 1.2.5 shows X-Ray Diffraction (XRD) patterns of amorphous and polycrystalline Si together with a corresponding reference crystalline silicon specimen [14]. For characterisation of a crystalline structure, the positions of the diffraction peaks depend on the dimensions of the unit cell of the material and are given by Bragg's Law, $n\lambda = 2dsin\theta$, where λ is wavelength of the incident wave, d is the spacing between a set of atomic planes and θ is the scattering angle [15]. The intensities of the diffraction peaks depend on the symmetry of the arrangement of atoms in the crystal structure. However, for amorphous specimens, a broad band is generally observed due to a lack of long-range order.

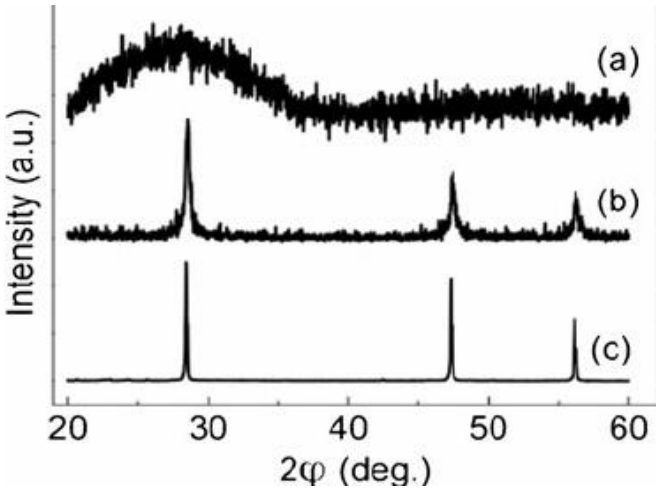


Figure 1.2.5 XRD patterns from (a) amorphous, (b) polycrystalline silicon and (c) reference single crystal silicon [14].

A more detailed discussion of scattering theory and a comparison of X-ray, neutron and electron and RDF analysis is given in Chapter 2.

Chapter 2 Reduced Density Function (RDF) Analysis

2.1 Scattering Theory and the Reduced Density Function

It has been shown that atomic structure can be probed by scattering various types of radiation from materials [16]. In this section the theory underpinning the use of electron scattering to characterise amorphous materials will be discussed.

The atomic scattering factor, f can be defined as the amplitude of a single electron scattered by an atom. Following Kirkland [17], Figure 2.1.1 plots f calculated for atoms and ions with different numbers of electrons as a function of a scattering vector $\boldsymbol{q} = 4\pi\sin\theta/\lambda$, where 2θ is the scattering angle and λ is the wavelength. The scattered intensity obtained from a single atom is given by the square of the scattering factor f^2. As more atoms are added to the sample being irradiated, the scattering intensity will increase [18, 19].

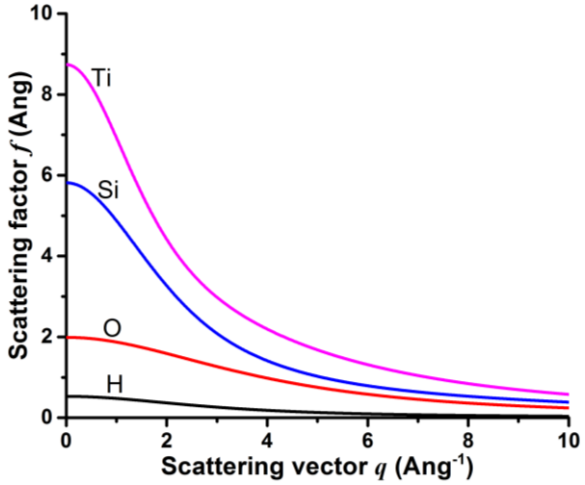


Figure 2.1.1 Electron scattering factor f as a function of scattering vector $\boldsymbol{q}$ calculated for isolated single atoms of various elements [17].

In case of an assembly of identical atoms, if the atoms scatter electrons independently without any interference, the intensity distribution will be equal to scattering of an individual atom multiplied by the number of scattering atoms N as shown in Figure 2.1.2.

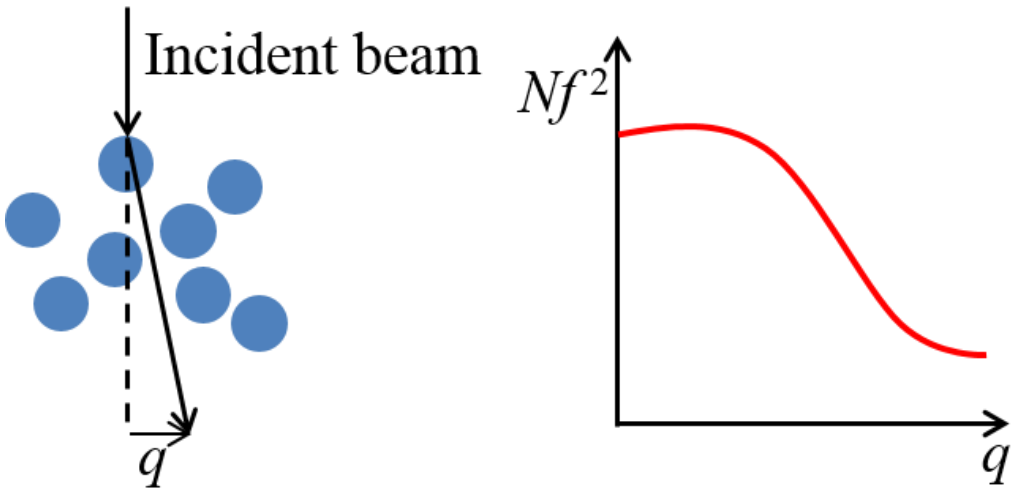


*Figure 2.1.2 Change in scattering intensity Nf^2 with scattering vector **q** for an assembly of independent identical atoms.*

If the atoms are completely ordered as in crystalline or polycrystalline materials there will be both destructive and constructive interference of the diffracted beams and the intensity distribution will show peaks at certain characteristic distances defined by Bragg's law as shown in Figure 2.1.3.

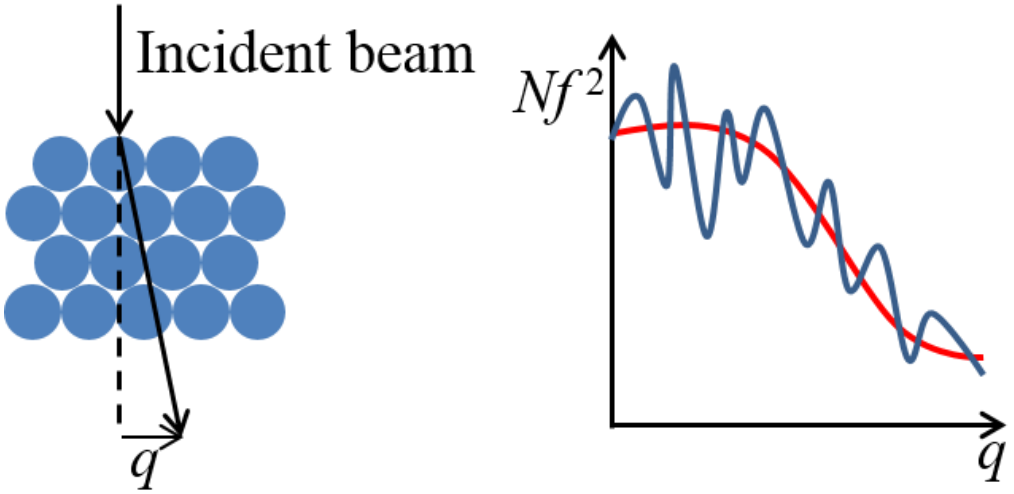


*Figure 2.1.3 Change in Nf^2 with **q** for a crystalline material.*

Finally, if the atoms are arranged in a topologically disordered structure, such as an amorphous material, there will be a small deviation from the independent atom intensity distribution as shown in Figure 2.1.4.

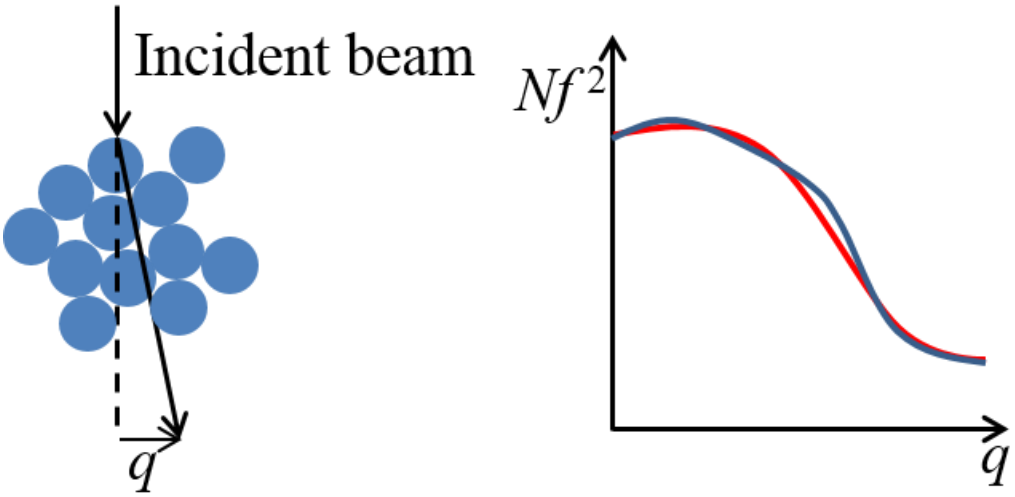


*Figure 2.1.4 Change in Nf^2 with **q** for an amorphous material.*

Due to their structural complexity, the structural information of amorphous structures cannot be simply predicted as for crystalline materials, instead, it is better described statistically. Using reduced density function (RDF) analysis, statistically averaged structural information can be extracted from experimental diffraction patterns. Subsequently in this section, general equations for RDF analysis are discussed.

The total scattered intensity, $I(\boldsymbol{q})$ for a particular assumed atomic arrangement for all orientations of the sample relative to the incident beam can be calculated following Warren [20, 21] using a Debye scattering function, where, $f(\boldsymbol{q})$ is the atomic scattering factor, $\boldsymbol{q}$ is the scattering vector and $\boldsymbol{r}_{ij} = |\boldsymbol{r}_i - \boldsymbol{r}_j|$ is the distance between two atoms.

$$I(\boldsymbol{q}) = N\langle f^2\rangle(\boldsymbol{q}) + \sum_{i\neq j}\sum_{j}\langle f\rangle^2(\boldsymbol{q})\sin(\boldsymbol{q}\boldsymbol{r}_{ij})/(\boldsymbol{q}\boldsymbol{r}_{ij}) \qquad (2.1)$$

Following Cockayne [22, 23], by introducing a pair distribution function, $g(\boldsymbol{r}) = \left[\sum_{i\neq j}\sum_{j} N\langle f\rangle^2(\boldsymbol{q})\rho_{ij}(\boldsymbol{r})\right]/N\langle f\rangle^2(\boldsymbol{q})$ where $\rho_{ij}(\boldsymbol{r})$ is the averaged density over all atomic pairs, the scattered intensity $I(\boldsymbol{q})$ can be rewritten in

$$I(\boldsymbol{q}) = N\langle f^2\rangle(\boldsymbol{q}) + 4\pi N\langle f\rangle^2(\boldsymbol{q})\int_0^\infty [g(\boldsymbol{r}) - \rho_0]\frac{\boldsymbol{r}}{\boldsymbol{q}}\sin(\boldsymbol{q}\boldsymbol{r})\, d\boldsymbol{r} \qquad (2.2)$$

Equation 2.2 shows that there is a mean intensity term, $Nf^2(\boldsymbol{q})$, which arises from the atoms scattering independently and a second term that describes the deviation from this mean intensity when the local density at $\boldsymbol{r}$ deviates from the mean density ρ_0.

To extract the RDF, a reduced scattered intensity function $\varphi(\boldsymbol{q})$ is defined as below [23],

$$\varphi(\boldsymbol{q}) = \frac{[I(\boldsymbol{q}) - N\langle f^2\rangle]\boldsymbol{q}}{N\langle f\rangle^2} \tag{2.3}$$

The function $\varphi(\boldsymbol{q})$ can be regarded as a scaled intensity $I(\boldsymbol{q})$ fitted with a function $N\langle f^2\rangle$, which is then Fourier transformed to give the RDF, $G(\boldsymbol{r})$.

$$G(\boldsymbol{r}) = 4\int_0^\infty \varphi(\boldsymbol{q})\sin(\boldsymbol{qr})d\boldsymbol{q} = 4\pi r[g(\boldsymbol{r}) - \rho_0] = \frac{J(\boldsymbol{r})}{\boldsymbol{r}} - 4\pi r\rho_0 \tag{2.4}$$

Using these equations, $G(\boldsymbol{r})$, $J(\boldsymbol{r})$, and the pair distribution function $g(\boldsymbol{r})$ can all be readily obtained from a diffraction pattern. An immediate benefit of using $G(\boldsymbol{r})$ instead of $J(\boldsymbol{r})$ is that $G(\boldsymbol{r})$ can be computed from $\varphi(\boldsymbol{q})$ without any knowledge of ρ_0.

2.2 Comparison with X-ray and Neutron Diffraction

According to the scattering theory described in previous section, the RDF analysis can be carried out using a measured scattered intensity. This is also valid for other sources of radiation. Therefore, in this section, a brief comparison of RDF analyses using X-ray, neutron and electron sources is given.

2.2.1 X-ray Diffraction

X-ray diffraction is versatile and is commonly used for structure determination. The wavelength of X-rays lies between the γ-ray and ultraviolet regions of the electromagnetic spectrum. For a laboratory diffraction experiment, X-rays are typically generated by bombarding a metal target, usually copper or molybdenum, with high-energy electrons. This generates X-rays when the incident electrons have sufficiently kinetic energy to eject core electrons from the metal atoms. However, for RDF analysis of amorphous materials, basic X-ray diffractometers do not provide sufficient scattered intensity at high scattering angles leading to poor signal to noise ratio in the recorded data. This lack of intensity range leads difficulties in accurate fitting while the poor signal to noise ratio can cause artefacts in the RDF curves. To avoid this synchrotron radiation is used as a powerful source of X-rays. The facility uses electrons accelerated to relativistic energies that change direction periodically, allowing X-rays to be emitted and directed toward a beamline.

2.2.2 Neutron Diffraction

Although the basic principles of diffraction are the same, neutrons and X-rays interact with materials differently. X-rays interact with the electron cloud around each atom and the contribution to the diffracted X-ray intensity is therefore larger for atoms with larger atomic number Z. In contrast, neutrons interact with the nucleus of the atom where the contribution to the diffracted intensity depends on the composition of the nucleus. For this reason, neutron diffraction is sensitive to elements with low atomic number such as hydrogen and can distinguish isotopes. Thus it is often the case that light atoms (low Z) contribute strongly to the diffracted intensity even in the presence of heavy atoms (high Z).

Two significant advantages for neutron diffraction can be identified. Firstly it is sensitive to the positions of the nuclei of the atoms and can show strong diffraction peaks even at high angles, which means that atomic positions in the structure can be determined with high precision [24]. Secondly, neutrons penetrate condensed matter strongly. Multiple scattering effects are, therefore, insignificant, which can greatly simplify the interpretation of the results. However, the technique requires a source of neutrons provided by either a nuclear reactor or spallation source, which may not be widely available. In addition, due to a low typical neutron flux a large sample volume is needed for acquisition compared to X-ray and electron diffraction.

2.2.3 Electron Diffraction

Unlike other types of radiation used in diffraction studies of materials, electrons are charged particles and interact with matter through Coulomb forces. This means that the incident electrons are affected by both the positively charged atomic nuclei and the surrounding electrons. In addition, the wavelength of an electron accelerated at typical voltages used in the TEM is much smaller than that used in X-ray and neutron diffraction experiments. An important consequence of this is that the radius of the Ewald sphere, $\boldsymbol{r} = 2\pi/\lambda$, is much larger in electron diffraction experiments. This allows the diffraction experiment to reveal more of the two-dimensional distribution of reciprocal reflections. Furthermore, electron lenses allow the geometry of the diffraction experiment to be varied. The conceptually simplest geometry is selected area electron diffraction (SAED) in which a broad parallel beam of electrons is incident on the specimen, with the specimen field of view selected using a post specimen aperture in an image plane in the TEM. Alternatively, by converging the electrons in a probe incident on the specimen, convergent beam electron diffraction (CBED) experiments can be performed using a range of incident angles simultaneously to reveal the full three-dimensional symmetry of the crystal. Importantly, electron diffraction in the TEM can be combined with direct imaging of the sample and a range of other spectroscopic techniques.

Furthermore, electron diffraction gives large scattering cross sections which permit rapid data collection. In addition, electrons can be easily focused into controlled geometry probes at specifically chosen areas. This enables the observation of the local atomic

structure of materials from very small volumes as compared to X-ray and neutron diffraction. Therefore, in this study electron diffraction is used.

2.3 The Historical Development of electron RDF Analysis

Early work by Grigson [25] attempted to obtain energy filtered diffraction patterns of solid metal films by developing a system to achieve high-speed direct recording of electron diffraction patterns. Moss et al. [26, 27] demonstrated a similar technique by using a scanning diffraction instrument with energy filtering of the diffracted electrons to obtain electron diffraction patterns of thin amorphous silicon films. It was only in 1988, that a detailed mathematical description of the conversion from the intensity distribution function $I(\boldsymbol{q})$ to the RDF $G(\boldsymbol{r})$ was given by Cockayne et al. [23]. The method claimed, to give a direct analysis of nearest neighbour distances accurate to 0.02Å together with coordination numbers from small regions of a specimen.

2.3.1 Energy Filtered Diffraction

To acquire the diffraction patterns for RDF analysis, Cockayne et al. [23] used a conventional TEM with an electron energy loss spectrometer (EELS) to give rapid collection of elastically scattered electrons. In this study, polycrystalline platinum was used to calibrate the TEM where the accuracy of the final results depended on the accuracy of this calibration, while the precision of the results depended on the step size of the scattering vector, the size of the diffraction pattern and the convergence angle of the incident beam. Further inaccuracies may also be present due to multiple scattering, unless the materials were thin enough to ensure this does not occur. During analysis, errors may be introduced when finding the centre of the diffraction pattern. As reported the centre of the diffraction pattern must be excluded by a beam stop during collection due to the "zero scattered" beam being of such high intensity that the variations in the rest of the diffraction

pattern are not recordable. A problem with the acquisition of diffraction patterns using EELS is that the energy loss window may drift over the collection time which limits the accuracy of results. To solve this problem, a further publication in 1991 by Cockayne et al. [28] demonstrated a more advanced form of electron energy filtering; Parallel Electron Energy Loss Spectrometry (PEELS). This study showed that PEELS has many advantages such as compensation for drift in the zero loss peak and the possibility of collecting energy loss spectra at each individual scattering angle and easy background removal. However, Heinemann et al. [29] criticized studies using EELS and PEELS as being "*a laborious and time consuming procedure, where the scattered electron intensity was recorded serially by shifting the diffraction pattern across the slit*". Their alternative used a TEM and a post column energy filter with multiple lenses located behind a magnetic prism which allowed the images to be recorded on a CCD with a specific electron energy loss. Vitreous silica and amorphous carbon films were tested after accurate calibration with polycrystalline gold and nickel. Diffraction patterns were taken and intensities were integrated using azimuthal average. Conversion of the intensities to RDFs was performed and the results were compared to previous work by Mozzi et al. [30] using X-ray and neutron diffraction.

2.3.2 Convergent Beam Diffraction

Previous RDF analysis demonstrated by Cockayne et al. [23] was restricted to diffraction patterns formed using parallel illumination to ensure that the intensity measured at a point p is from a specific scattering vector as shown in Figure 2.3.1 (a). However, due to the limited size of parallel probe around 400nm, further work by McBride et al. [31] used convergent beams in the TEM in order to study much smaller volumes of materials.

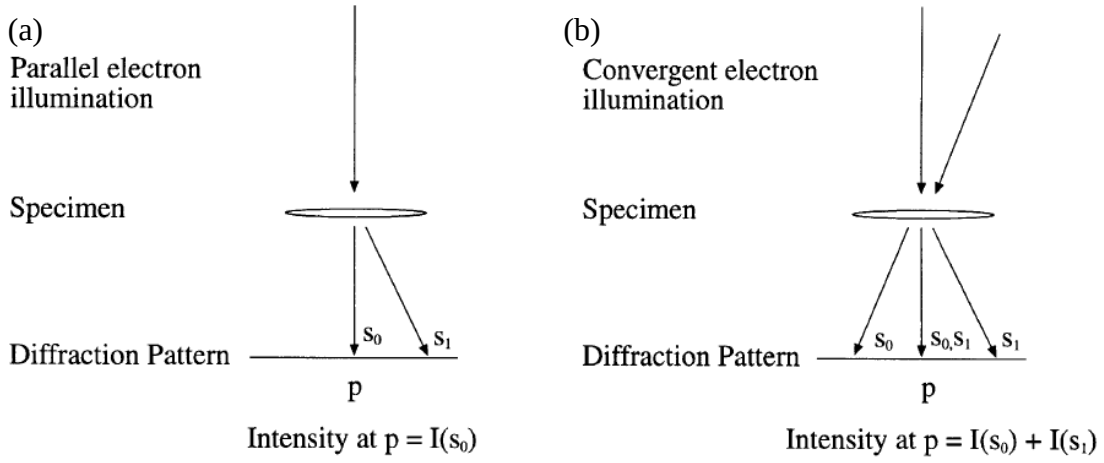


Figure 2.3.1 Schematic diagrams of parallel and convergent illumination [31].

When using convergent illumination, electrons have a range of incident directions which will lead to incoherent illumination. The intensities in the recorded diffraction pattern can thus be regarded as a superposition of intensities from each incident direction as shown in Figure 2.3.1 (b) and the diffraction pattern can alternatively be represented as a diffraction pattern from a single incident beam direction convolved with a point spread function (PSF). Therefore, deconvolution of the PSF will allow the retrieval of the real diffraction intensity and consequently the RDF analysis. Figure 2.3.2 shows the comparison of $G(\boldsymbol{r})$

from parallel, converged and deconvolved diffraction patterns, indicating how deconvolution helps to retrieve high frequencies lost to converged result.

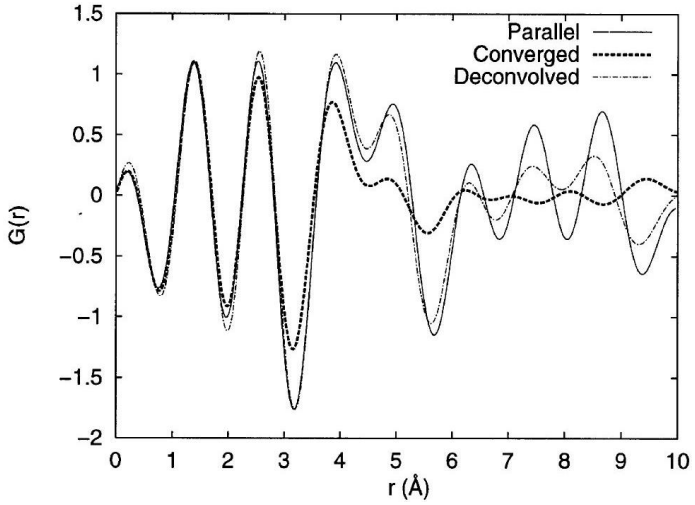


Figure 2.3.2 $G(\boldsymbol{r})$ of amorphous carbon formed from parallel, converged and deconvolved diffraction patterns [31].

Subsequently, McBride et al. [32] further improved the accuracy of results using a convergent beam in 2003. By using a new energy filtering technique with an omega filter in the TEM, they were able to perform energy filtered diffraction using image plates [33] for data recording. These provide a large dynamic range which allows the central undiffracted spot and diffraction rings to be collected in a single exposure, giving a strong signal over all scattering angles without need for overlapping diffraction patterns recorded with different exposures.

To reduce the volume of material being studied even further, McBride et al. [34] studied the use of a field emission gun (FEG) as opposed to a tungsten hairpin filament or a LaB_6 source in the TEM, which are beneficial as they can produce probes smaller than 1nm (FWHM). As discussed earlier, using a convergent beam no longer satisfies the assumption that illumination has a single direction of incidence, as required for RDF analysis. This was previously correct for non-field emission sources by assuming that different angles of incidence in the convergent beam are incoherent and can be corrected by deconvolution [35]. The convergent beam produced by a FEG, however, is (partially) coherent [36] which gives rise to a broadening of the diffraction pattern peaks which cannot necessarily be described by a simple deconvolution of the PSF. However, it was demonstrated that for probe sizes down to 1.2nm, deconvolution corrects the broadening and thus the data can be used for RDF analysis which allows studies of very small volumes, such as intergranular amorphous phases [34].

2.3.3 Multiple Scattering

An assumption in electron RDF analysis is that electrons undergo single scattering events. To fulfil this assumption experimentally generally requires that films of material are thin and consist of low atomic number elements. The required thickness depends on the energy of the electron beam, from which the scattering mean free path can be calculated for a particular element. If the film thickness is less than the mean free path, it can be assumed electrons are only scattered once. To study the effects of multiple scattering, Anstis et al. [37] used thick foils to examine this assumption. They found that multiple scattering introduces errors in the coordination numbers measured from nearest neighbour peaks but does not influence the positions of the peaks as shown in Figure 2.3.3. Following Anstis' method, Peterson et al. [38] described a method to use diffraction patterns taken with different electron wavelengths to extract the single scattering intensity from the multiple scattering intensity.

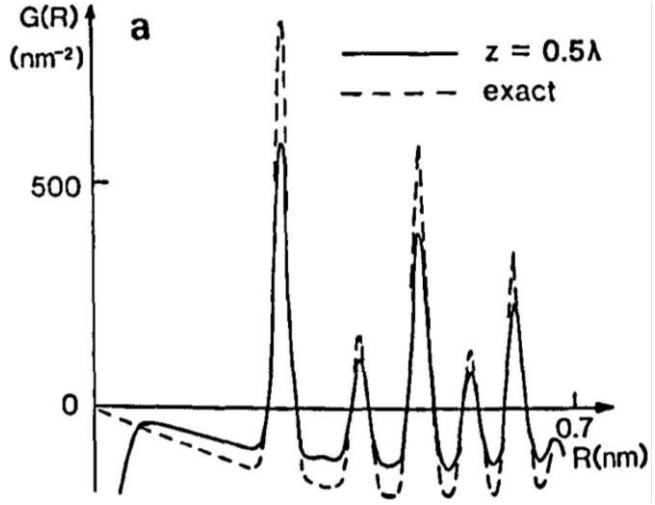


Figure 2.3.3 $G(\boldsymbol{r})$ of amorphous silicon derived from simulated data for thickness of 0.5λ [37].

2.3.4 RDF Analysis in Material Science

There are a number of published studies of amorphous materials using electron RDF analysis. In 1991, McKenzie et al. [39] used RDF to solve the structure of a thin film of amorphous carbon prepared by arc plasma deposition which has a tetrahedral coordinated structure (ta-C) instead of a graphitic structure. These results suggested that formation of the ta-C structure is due to stress caused during deposition. Subsequently, McCulloch et al. [40] combined simulations based on density functional theory (DFT) with RDF analysis to study ta-C and aluminium nitride films. They suggested the use of DFT simulated models as starting points with Reverse Monte Carlo (RMC) to refine the models obtained accordingly to RDF data. Shen and Mai [41] used RDF to study amorphous and crystallized tungsten nitride thin films in 2000, comparing them to theoretical calculations based on the determined crystalline phases and found good agreement demonstrating the ability of RDF to identify different structures. Hirotsu et al. [42] studied amorphous alloys of $Fe_{90}Zr_7B_3$ and SiC using electron RDF data and modelling using Monte Carlo simulations. They found that $Fe_{90}Zr_7B_3$ undergoes nanoscale phase separation and that SiC contains homonuclear Si-Si and C-C bonds as well as heteronuclear Si-C bonds, the ratio of which changed with relaxation of amorphous structure.

2.4 RDF Analysis of Amorphous Materials

2.4.1 Experimental RDF Analysis

2.4.1.1 Acquisitions of Diffraction Patterns

To investigate how various experimental parameters influence RDF analysis, an amorphous SiO_2 grid with thickness of 216Å (Agar Scientific Ltd, UK) was used as standard specimen. The standard microscope setup is shown in Table 2.4.1 for a JEM-2100 microscope. Diffraction patterns of the specimen were acquired as shown below in Figure 2.4.1 (a). A beam stop was used to block the intense central beam, in order to collect intensity at larger scattering angles while avoiding the risk of damaging the CCD during long exposures.

Table 2.4.1 Standard setup of the microscope.

TEM	JEM-2100 microscope (JEOL, Japan)
Emitter	LaB_6
Accelerating Voltage	200kV
Condenser Aperture	50μm
Illumination System	TEM mode for selected area diffraction (SA aperture of 10-120μm in diameter) NBD mode for nanobeam diffraction (Parallel probe of 280nm in diameter)
Camera Length	18cm
CCD	Orius SC200 (Gatan, USA)

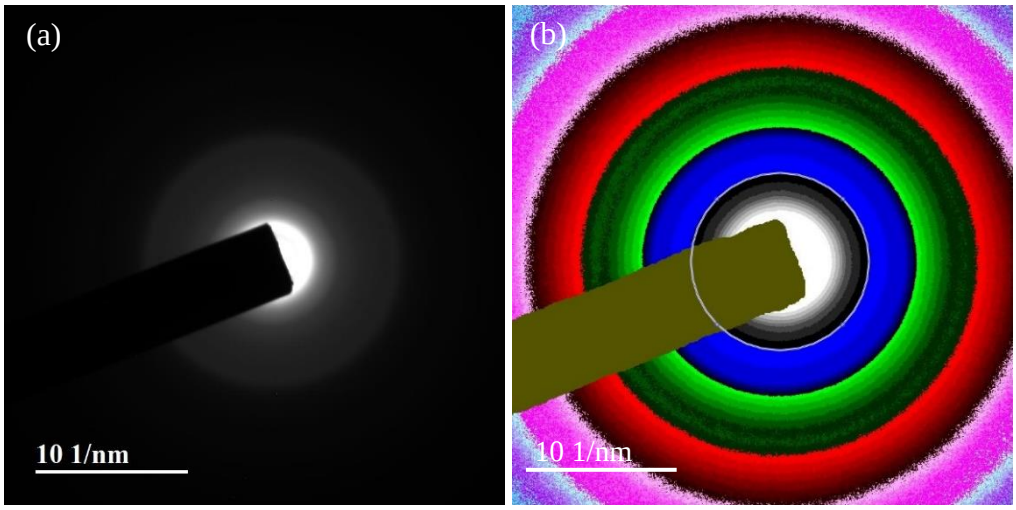


Figure 2.4.1 Electron diffraction pattern taken from a 216Å amorphous SiO_2 specimen. (a) Original image and (b) the same pattern displayed in coloured contour mode.

To calculate the correct intensity distribution function, $I(\boldsymbol{q})$, the centre location in the experimental diffraction pattern is needed to determine the origin of the scattering vector $\boldsymbol{q} = 0$. A group-designed software, "eRDF Analyser" [43] was used for this purpose. This allows users to mask beam stops or any distorted areas (to null the intensity within the area for precise calculation) and can define the centre by manual or optimised fitting of contours with equal intensity in a coloured contour mode, as shown in Figure 2.4.1 (b).

For the optimisation of the pattern centre the software generates a pair of concentric circles which include an initial guess and calculates a functional that minimises the sum of azimuthal variance within the limits defined by the concentric circles. The optimisation of the functional is performed by a grid scan, computing an array of values as a function of different positions of the centre. After thorough testing of many diffraction patterns, it is my experience that based on the coloured contour plotting of the diffraction pattern, the

initial guess of the centre position is sufficiently accurate for further analysis, usually within five pixels. Therefore, only a small area grid scan (< 5 pixels) is required for optimisation.

The software then generates $I(\boldsymbol{q})$ automatically by dividing the diffraction pattern in rings of equal radius increment following Equation 2.5 below, where i is the distance from the chosen centre and n is the number of pixels corresponding to that radial distance.

$$I(\boldsymbol{q})_{azav} = \frac{\sum_{i=1}^{n} I(\boldsymbol{q})_i}{n} \tag{2.5}$$

The measured $I(\boldsymbol{q})$ of a 216Å amorphous SiO_2 specimen is shown in Figure 2.4.2.

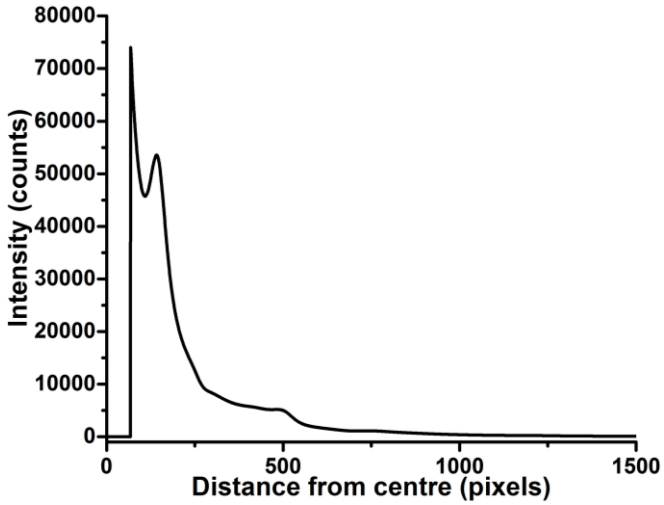


Figure 2.4.2 Intensity distribution function $I(\boldsymbol{q})$ of 216Å amorphous SiO_2 specimen extracted by azimuthal averaging.

2.4.1.2 Calculation of the Calibration Factor

Before fitting the scattering vector, $\boldsymbol{q}$, a calibration factor $\delta\boldsymbol{q}$ is needed in order to calibrate the pixel values (pixel to $Å^{-1}$) of the detector. A polycrystalline aluminium diffraction standard (SPI Supplies, USA) was used as a known crystalline specimen for the calibration. It is important to note that the crystalline diffraction patterns have to be taken under identical microscope settings to those used to record data from the amorphous specimens to ensure the accuracy of $\delta\boldsymbol{q}$.

Figure 2.4.3 shows a selected area diffraction pattern acquired from a polycrystalline aluminium specimen. Using the centre finding function within eRDF Analyser, $I(\boldsymbol{q})$ was calculated as shown in Figure 2.4.4, where the sharp peaks correspond to the pixel number n_i of each diffracted ring.

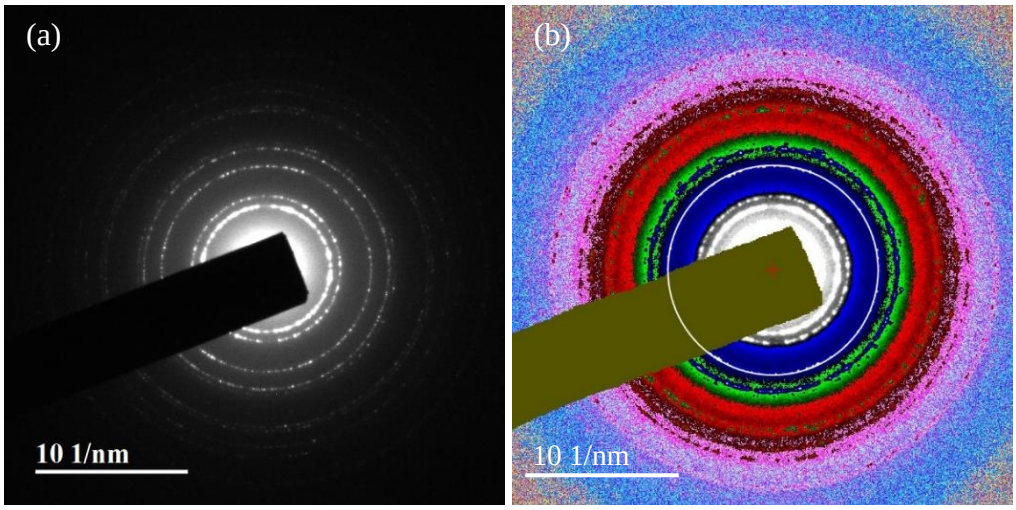


Figure 2.4.3 Electron diffraction pattern taken from a polycrystalline Aluminium specimen. (a) Original image and (b) the same pattern displayed in coloured contour mode.

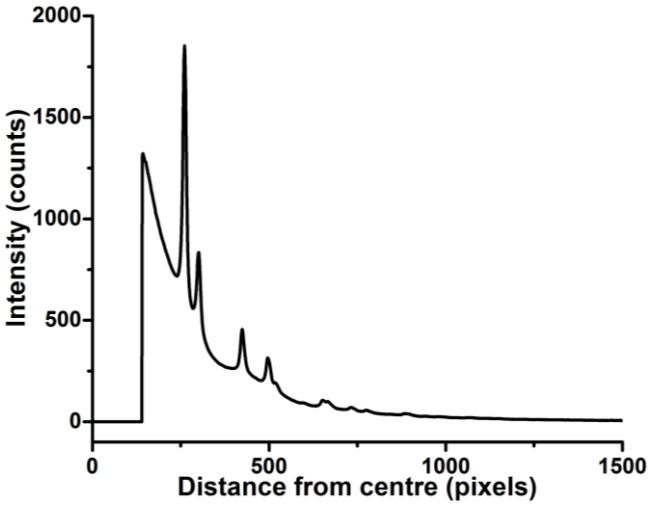


Figure 2.4.4 Intensity distribution function extracted from the diffraction pattern of the polycrystalline aluminium specimen shown in Figure 2.4.3.

Al has a face centred cubic structure with a lattice parameter, $a = 4.046\text{Å}$. For the symmetry allowed reflections, $= h^2 + k^2 + l^2$, the principle lattice spacings $d = a/\sqrt{N}$ are listed below in Table 2.4.2,

Table 2.4.2 Lattice spacings of polycrystalline Aluminium.

N	Lattice spacings (Å)
3 (111)	2.336
4 (200)	2.023
8 (220)	1.430
11 (311)	1.220
12 (222)	1.168

From the lattice spacings, d_i and pixel numbers, n_i, $\delta \boldsymbol{q}_i$ can be computed as

$$\delta \boldsymbol{q}_i = \frac{2\pi}{n_i \cdot d_i} \tag{2.6}$$

For accuracy, the values of $\delta \boldsymbol{q}_i$ measured from individual rings were averaged to give a final value of $\delta \boldsymbol{q}$ for RDF analysis. Using $I(\boldsymbol{q})$ from Figure 2.4.4, Table 2.4.3 gives $\delta \boldsymbol{q}$ calculated using Equation 2.6.

Table 2.4.3 Calculation of calibration factor though pixel numbers and lattice spacing from polycrystalline aluminium.

i (*hkl*)	Pixel numbers n_i (pixel)	lattice spacings d_i (Å)	$\delta \boldsymbol{q}_i = \frac{2\pi}{n_i \cdot d_i}$	
1 (111)	260	2.336	0.010345	Average $\delta \boldsymbol{q}$ = 0.0103557 ± 0.0000085 (±0.08%)
2 (200)	300	2.023	0.010353	
3 (220)	424	1.430	0.010363	
4 (311)	497	1.220	0.010362	

Table 2.4.3 shows that the averaged $\delta \boldsymbol{q}$ calculated using the first four reflections is 0.0103557Å^{-1} with a standard deviation of 0.0000085Å^{-1}. This gives an error of 0.08% suggesting that $\delta \boldsymbol{q}$ calculated from a single diffraction pattern is sufficiently accurate.

However, due to the hysteresis in the lens system, the excitation of the intermediate lens is frequently changed between different magnifications when switching between diffraction and image modes. The error in magnifications causes by hysteresis ranges up to 5 to 10% depending on the operation mode. To test the effect of hysteresis, a diffraction

pattern of polycrystalline aluminium was captured again after a month. The diffraction pattern is shown in Figure 2.4.5 while the $I(\boldsymbol{q})$ comparison with previous data is shown in Figure 2.4.6. At last, Table 2.4.4 gives the $\delta\boldsymbol{q}$ calculation.

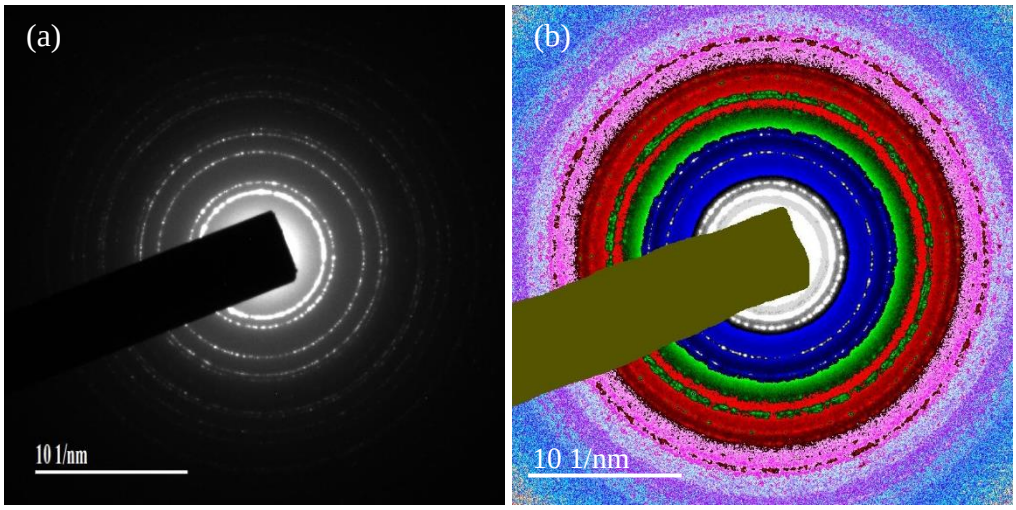


Figure 2.4.5 Electron diffraction pattern taken from a polycrystalline Aluminium specimen. (a) Original image and (b) the same pattern displayed in coloured contour mode.

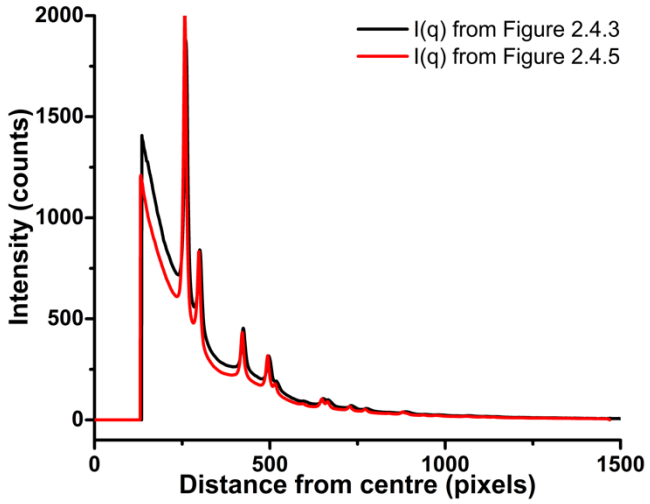


Figure 2.4.6 Intensity distribution extracted from the diffraction pattern of a polycrystalline Aluminium specimen shown in Figure 2.4.5.

Table 2.4.4 Calculation of the calibration factor of polycrystalline aluminium after a month.

i (*hkl*)	Pixel numbers n_i (pixel)	lattice spacings d_i (Å)	$\delta \boldsymbol{q}_i = \frac{2\pi}{n_i \cdot d_i}$	
1 (111)	258	2.336	0.010425	Average $\delta \boldsymbol{q}$ = 0.0104274 ± 0.0000063 (±0.06%)
2 (200)	298	2.023	0.010422	
3 (220)	421	1.430	0.010437	
4 (311)	494	1.220	0.010425	

From Figure 2.4.6, a small shift in the diffracted peaks around 2-3pixels can be observed which will result in small $\delta \boldsymbol{q}$ variation. Table 2.4.3 shows that the averaged $\delta \boldsymbol{q}$ is $0.0104274 Å^{-1} \pm 0.0000063 Å^{-1}$ with an error of 0.06%. Comparing results from Table 2.4.3 and Table 2.4.4, an error of 0.69% is obtained from both $\delta \boldsymbol{q}$ values. Therefore, it is important to note that $\delta \boldsymbol{q}$ needs to be calibrated for every experiment and the effect of errors in $\delta \boldsymbol{q}$ on the RDF will be discussed in Section 2.4.2.1.

2.4.1.3 Background Fitting

After acquiring both $I(\boldsymbol{q})$ and $\delta\boldsymbol{q}$, the reduced intensity function $\varphi(\boldsymbol{q})$ can be obtained by fitting $I(\boldsymbol{q})$ and $N\langle {f_{fit}}^2 \rangle$ following Equation 2.3.

A fitting parameter, f_{fit}, needs to be determined for the fitting procedure. Previous studies by Kaplow et al. [44] and Konnert et al. [45] obtained f_{fit} based on a priori knowledge of $G(\boldsymbol{r})$ for materials such as liquid mercury, lead and silica. Alternatively, Doyle et al. [46] proposed the use of a series of Gaussian functions $a_i e^{-b_i \boldsymbol{q}^2}$ to represent f_{fit} although they also reported that f_{fit} may be better approximated by a Lorenzian function. In 2015, Lobato et al. [47] demonstrated a detailed comparison between several parameterisations including works by Weickenmeier et al. [48], Peng et al. [49], Kirkland [17] and their own. They suggested that the parameterisations of Weickenmeier, Kirkland and Lobato produce similar results while Peng's parameterisation does not model the correct behaviour at high scattering angles.

Therefore, in this study the parameterisation of f_{fit} used is that given by Kirkland [17] which is widely used in simulations of electron diffraction and high-resolution imaging. This parameterisation is described as below as:

$$f_{fit-Kirkland} = \sum_{i=1}^{3} \frac{a_i}{\left(\frac{\boldsymbol{q}^2}{4\pi^2}\right) + b_i} + \sum_{i=1}^{3} c_i e^{-d_i\left(\frac{\boldsymbol{q}^2}{4\pi^2}\right)} \qquad (2.7)$$

Kirkland's representation of f_{fit} consists of two functions, (Gaussian and Lorenzian terms), $c_i e^{-d_i(\boldsymbol{q}^2/4\pi^2)}$ and $a_i/[(\boldsymbol{q}^2/4\pi^2)+b_i]$, respectively, where a_i, b_i, c_i and d_i are parameterisation values. An advantage of using Kirkland's representation of f_{fit} is that the Gaussian terms provide a better fitting of f_{fit} at lower scattering angles while the Lorenzian terms are more accurate at higher scattering angles.

Here SiO_2 is used as an example for the calculation of $\langle {f_{fit}}^2 \rangle$ and $\langle f_{fit} \rangle^2$:

$$\langle {f_{fit-Kirkland}}^2 \rangle = f_{Si}^2 + f_O^2$$

$$= \left\{ p_{Si} \left[\sum_{i=1}^{3} \frac{a_i^{Si}}{\left(\frac{\boldsymbol{q}^2}{4\pi^2}\right) + b_i^{Si}} + \sum_{i=1}^{3} c_i^{Si} e^{-d_i^{Si}(\frac{\boldsymbol{q}^2}{4\pi^2})} \right] \right\}^2 \tag{2.8}$$

$$+ \left\{ p_o \left[\sum_{i=1}^{3} \frac{a_i^{o}}{\left(\frac{\boldsymbol{q}^2}{4\pi^2}\right) + b_i^{o}} + \sum_{i=1}^{3} c_i^{o} e^{-d_i^{o}(\frac{\boldsymbol{q}^2}{4\pi^2})} \right] \right\}^2$$

$$\langle f_{fit-Kirkland} \rangle^2 = (f_{Si} + f_O)^2$$

$$= \left\{ p_{Si} \left[\sum_{i=1}^{3} \frac{a_i^{Si}}{\left(\frac{\boldsymbol{q}^2}{4\pi^2}\right) + b_i^{Si}} + \sum_{i=1}^{3} c_i^{Si} e^{-d_i^{Si}(\frac{\boldsymbol{q}^2}{4\pi^2})} \right] \right.$$

$$\left. + p_o \left[\sum_{i=1}^{3} \frac{a_i^{o}}{\left(\frac{\boldsymbol{q}^2}{4\pi^2}\right) + b_i^{o}} + \sum_{i=1}^{3} c_i^{o} e^{-d_i^{o}(\frac{\boldsymbol{q}^2}{4\pi^2})} \right] \right\}^2 \tag{2.9}$$

where $p_{Si} = N_{Si}/N$ and $p_O = N_O/N$ are the composition factors of Si and O. In the case of SiO_2, $p_{Si} = 1/3$ and $p_O = 2/3$. The Kirkland parameters for Si and O are listed in Table 2.4.4. The units for a_i, b_i, c_i and d_i are $Å^{-1}$, $Å^{-2}$, Å and $Å^2$, respectively.

Table 2.4.5 Kirkland parameters for Si and O [17].

Element	Kirkland fitting parameters		
Silicon (Z=14)	a_1 = 1.06543892	a_2 = 0.120143691	a_3 = 0.180915263
	b_1 = 1.04118455	b_2 = 68.7113368	b_3 = 0.0887533926
	c_1 = 1.12065620	c_2 = 0.0305452816	c_3 = 1.59963502
	d_1 = 3.70062619	d_2 = 0.214097897	d_3 = 9.99096638
Oxygen (Z=8)	a_1 = 0.339969204	a_2 = 0.307570172	a_3 = 0.130369072
	b_1 = 0.38157028	b_2 = 0.381571436	b_3 = 19.1919745
	c_1 = 0.0883326058	c_2 = 0.1965867	c_3 = 0.000996220028
	d_1 = 0.760635525	d_2 = 2.07401094	d_3 = 0.0303266869

After acquiring the fitting parameters, it is possible to fit $I(\boldsymbol{q})$ with $N\langle {f_{fit}}^2 \rangle$. The fitting procedure is an interactive process which may require different selections of the data range for $\boldsymbol{q}$ (which is discussed later) as well as adjusting parameters such as effective total atomic number N. The overall aim of the fitting is to focus on following the trend of $I(\boldsymbol{q})$ while minimising any unreasonable peaks, such as peaks below 1.1Å.

To make the fitting process easier an automated fitting routine is provided in "eRDF Analyser" based on a least squares approach as described in [43]. Note that in the software used the full range of the data and last third of the whole data range was selected.

Figure 2.4.7 shows the steps needed to compute $G(\boldsymbol{r})$ as described in this section. Figure 2.4.7 (a) shows $I(\boldsymbol{q})_{exp}$ and the fitting function $I(\boldsymbol{q})_{fit}$ for a data range $\boldsymbol{q}$ between 2 and 15Å^{-1}. Figures 2.4.7 (b) and (c) illustrate the computed $\varphi(\boldsymbol{q})$ and $G(\boldsymbol{r})$ after fitting.

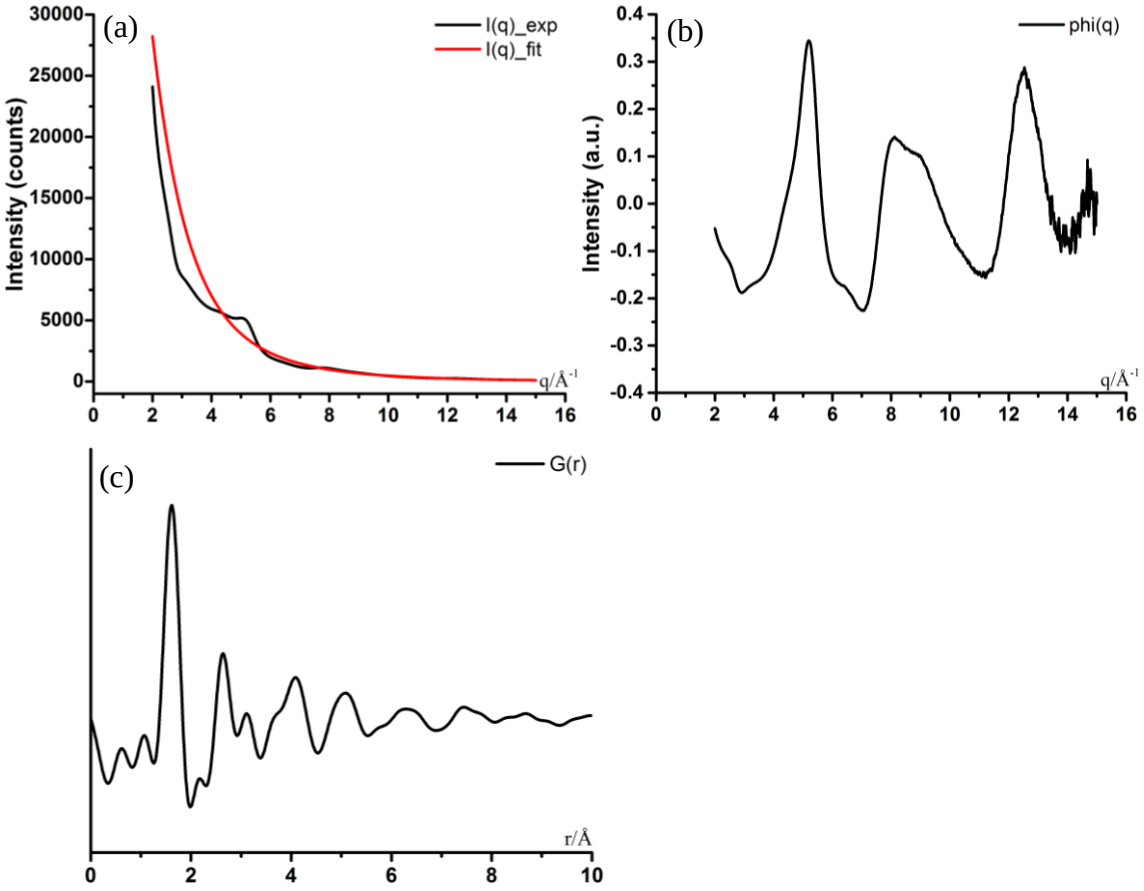


Figure 2.4.7 The intensity distribution function and fitting function with a selected $\boldsymbol{q}$ *range between 2 to 15Å*$^{-1}$*. (b) Resulting reduced intensity function* $\varphi(\boldsymbol{q})$ *calculated from equation 2.3. (c) Final reduced density function* $G(\boldsymbol{r})$ *calculated from equation 2.4.*

2.4.2 Factors Affecting the RDF Calculation

Since the RDF analysis is based on a series of equations as described in Section 2.1, errors in the input parameters will result in errors in the RDF outputs. Therefore, factors that affect the RDF calculation are discussed in this section.

2.4.2.1 Effect of the Calibration Factor on the RDF

As described in Section 2.4.1.2, $\delta \boldsymbol{q}$ is a value which represents the pixel size of the sensor. In practice, $\delta \boldsymbol{q}$ is influenced by the experimental settings of the microscope due to hysteresis in the lens system. Therefore, the following section examines the level of tolerance in the RDF to $\delta \boldsymbol{q}$.

To illustrate the effect of $\delta \boldsymbol{q}$, a value of 0.0103557 ± 0.0000085Å^{-1} as calculated in Section 2.4.1.2 was used together with $I(\boldsymbol{q})$ taken from a 216Å amorphous SiO_2 film. Additional $\delta \boldsymbol{q}$ values with ±0.5 and ±1% difference were used to check the level of tolerance in the calculated RDF. The resulting $\varphi(\boldsymbol{q})$ and $G(\boldsymbol{r})$ are shown in Figure 2.4.8 and statistical measurements of peak position and amplitude with relative errors are given in Table 2.4.6 for detailed comparison.

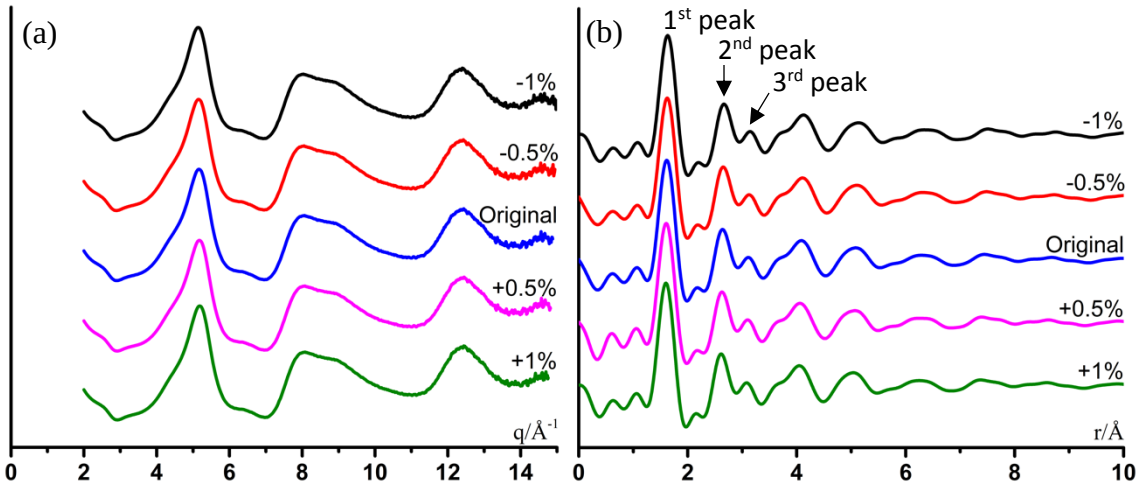


Figure 2.4.8 Effect of calibration factor $\delta \boldsymbol{q}$ on RDF. $\delta \boldsymbol{q}$ values with increments of 0.5% were used to compute the $G(\boldsymbol{r})$ curves.

Table 2.4.6 Effect of $\delta \boldsymbol{q}$ on $G(\boldsymbol{r})$. Deviations in (a) peak positions and (b) amplitude of the first three peaks.

(a) Peak position	1st	2nd	3rd
-1%	1.63 (+1.24%)	2.67 (+1.14%)	3.14 (+0.96%)
-0.5%	1.62 (+0.62%)	2.65 (+0.38%)	3.13 (+0.64%)
Original	1.61 (0%)	2.64 (0%)	3.11 (0%)
+0.5%	1.60 (-0.62%)	2.63 (-0.38%)	3.10 (-0.32%)
+1%	1.60 (-0.62%)	2.61 (-1.14%)	3.08 (-0.96%)

Unit: Å (Relative error wrt Original)

(b) Peak amplitude	1st	2nd	3rd
-1%	3.845 (+0.27%)	1.547 (-0.52%)	0.335 (+2.60%)
-0.5%	3.811 (-0.62%)	1.538 (-1.10%)	0.318 (-2.70%)
Original	3.835 (0%)	1.555 (0%)	0.327 (0%)
+0.5%	3.854 (+0.50%)	1.580 (+1.56%)	0.358 (+9.45%)
+1%	3.938 (+2.67%)	1.601 (+2.95%)	0.330 (+1.01%)

Unit: a.u. (Relative error wrt Original)

From Figure 2.4.8, when the value of $\delta \boldsymbol{q}$ varies, all $\varphi(\boldsymbol{q})$ still show similar results while the peak positions and heights shown in $G(\boldsymbol{r})$ are altered. Statistical results from Table 2.4.6 show that if $\delta \boldsymbol{q}$ varies within 0.5%, the maximum deviation of the peak position is 0.02Å (0.6%). Even if $\delta \boldsymbol{q}$ varies up to 1%, the peak position still deviates within 0.03Å (1.2%). In addition, the maximum peak amplitude deviates by about 9% and 3% respectively.

Note that the error of $\delta \boldsymbol{q}$ due hysteresis is 0.69% as discussed previously in Section 2.4.1.2.

2.4.2.2 Effect of Centre Location in a Diffraction Pattern on the RDF.

Although a systematic optimisation routine [43], as described in Section 2.4.1.1, was used for the location of the centre of the diffraction patterns to ensure stable $I(\boldsymbol{q})$ values a detailed study is required to determine the level of tolerance to errors in the centre location. The true centre after optimisation is shown as X: 1098 Y: 1049 in Figure 2.4.9 (a). To compare the effect of centre location on the RDF, five different centre locations were manually selected, where one is the true centre after optimisation and the others for the measurement values given in Table 2.4.7.

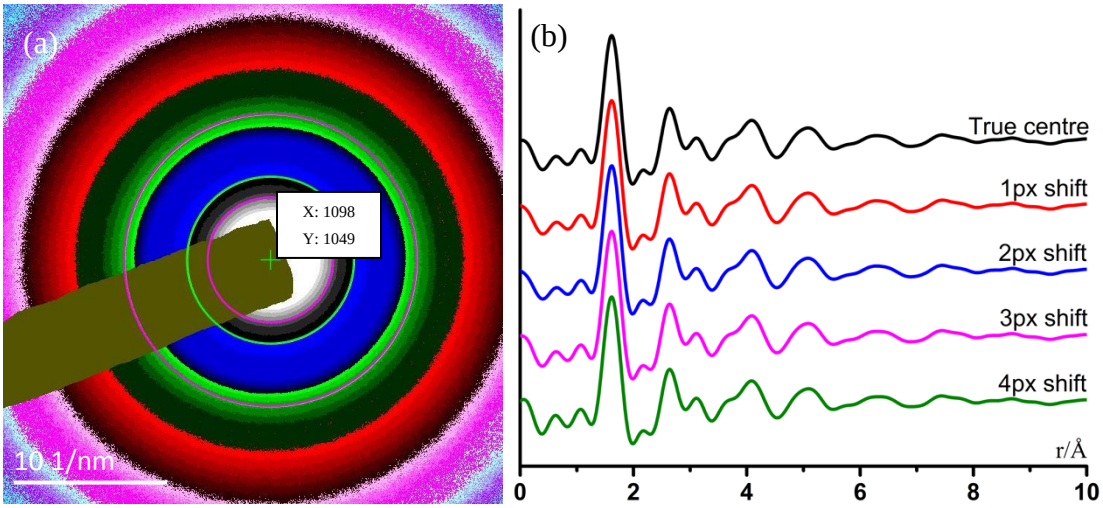


Figure 2.4.9 Effect of centre location of the diffraction pattern on the RDF. (a) Diffraction pattern of amorphous SiO_2 showing the true centre location. (b) RDF curves extracted from true centre and a centre shifted by 1-4pixel $I(\boldsymbol{q})$.

Table 2.4.7 Effects of centre location on $G(\boldsymbol{r})$. Deviations in (a) peak positions and (b) amplitude of the first three peaks.

(a) Peak position	1st	2nd	3rd
True centre	1.62 (0%)	2.64 (0%)	3.11 (0%)
1 pixel shift	1.62 (0%)	2.64 (0%)	3.11 (0%)
2 pixel shift	1.62 (0%)	2.64 (0%)	3.11 (0%)
3 pixel shift	1.62 (0%)	2.64 (0%)	3.11 (0%)
4 pixel shift	1.61 (-0.62%)	2.64 (0%)	3.11 (0%)

Unit: Å (Relative error wrt True centre)

(b) Peak amplitude	1st	2nd	3rd
True centre	3.895 (0%)	1.573 (0%)	0.322 (0%)
1 pixel shift	3.893 (-0.07%)	1.567 (-0.41%)	0.315 (-2.29%)
2 pixel shift	3.893 (-0.07%)	1.566 (-0.43%)	0.314 (-2.50%)
3 pixel shift	3.899 (+0.10%)	1.575 (+0.14%)	0.330 (+2.50%)
4 pixel shift	3.912 (+0.43%)	1.584 (+0.71%)	0.350 (+8.50%)

Unit: a.u. (Relative error wrt True centre)

It is clear from both Figure 2.4.9 and Table 2.4.7 that a shift of 4 pixels will only result in maximum deviation of the peak position is 0.01Å, which is less than a 1% error. Moreover, after repeated testing of the centre optimisation routine, the maximum shift of the centre finding routine is found to be less than 2 pixels. This gives no deviation in peak position and a maximum error in peak amplitude less than 3%.

2.4.2.3 Effect of Data Range on the RDF

After acquiring a reliable azimuthal averaged intensity $I(\boldsymbol{q})$ from a specimen, the selection of data range also plays an important role during the RDF extraction process. Following Equation 2.4, $G(\boldsymbol{r})$, $4\int_0^\infty \varphi(\boldsymbol{q})\sin(\boldsymbol{qr})\,d\boldsymbol{q}$, is a Fourier transform of $\varphi(\boldsymbol{q})$ with infinite $\boldsymbol{q}$ range. However, in an experimental measurement, $\varphi(\boldsymbol{q})$ only covers a limited range of data.

To study this effect, five different data ranges, 15 ± 10Å^{-1} with an increment of 5Å^{-1}, were selected for comparison. A damping factor $b = 0.2$ (which will be discussed later in Section 2.4.2.5) was applied to reduce the oscillations in $G(\boldsymbol{r})$. However, diffraction patterns with the electron beam located at the centre as shown in Figure 2.4.9 show data up to a values of $\boldsymbol{q}_{max}$ = 15Å^{-1}. Therefore, a new diffraction pattern was recorded, as shown in Figure 2.4.10, with the electron beam placed at the edge of the sensor. This allows the recording of diffraction patterns with a data range $\boldsymbol{q}_{max}$= 25Å^{-1}.

The RDFs extracted are shown in Figures 2.4.11 (a) and (b), which represent $\varphi(\boldsymbol{q})$ and $G(\boldsymbol{r})$ calculated using different data ranges.

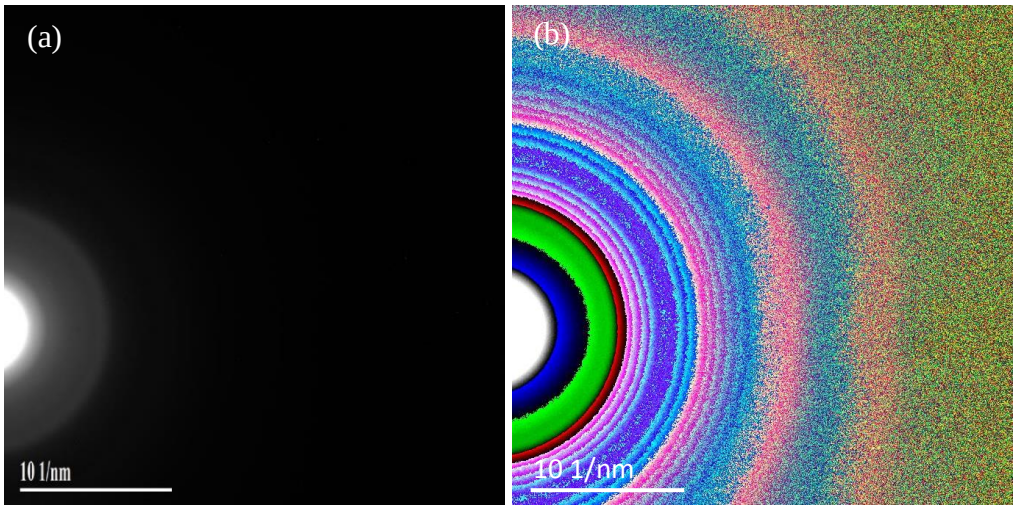


Figure 2.4.10 Electron diffraction pattern of an amorphous SiO_2 specimen without a beam stop. (a) Original image and (b) the same pattern displayed in coloured contour mode.

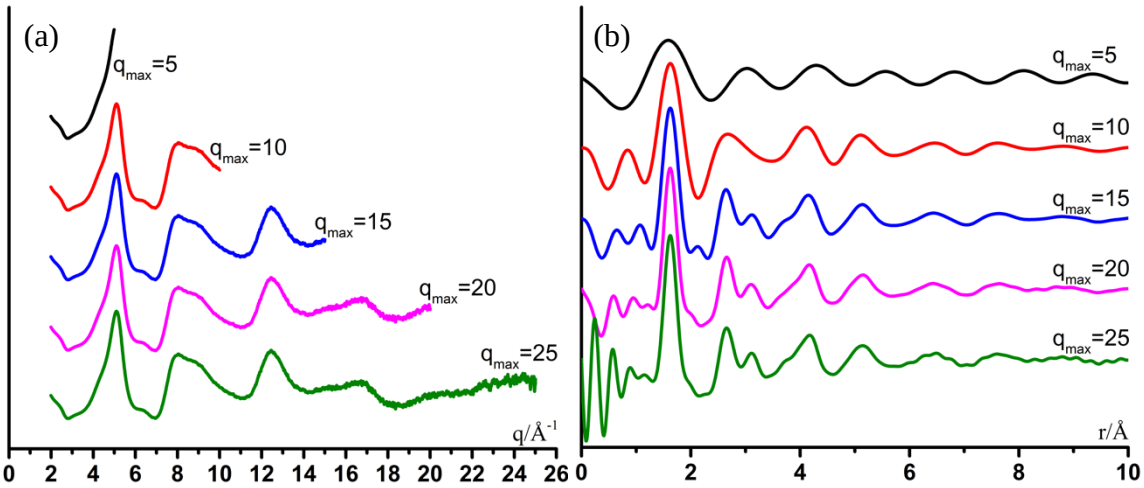


Figure 2.4.11 Effect of data range selection on RDF. (a) $\varphi(\boldsymbol{q})$ and (b) RDF curves extracted from different data range selections.

Figure 2.4.11 (a) shows that the general shape of $\varphi(\boldsymbol{q})$ with $\boldsymbol{q}_{max}$ = 15, 20, 25Å^{-1} is similar although each has different $\boldsymbol{q}_{max}$ value. After Fourier transformation, the same result is observed for $G(\boldsymbol{r})$ as shown in Figure 2.4.11 (b). Three curves with $\boldsymbol{q}_{max}$ = 15, 20, 25Å^{-1} are almost identical while $G(\boldsymbol{r})$ with $\boldsymbol{q}_{max}$ = 5Å^{-1} is different due to its

insufficient data range. For $G(\boldsymbol{r})$ with $\boldsymbol{q}_{max}$ = 10Å^{-1}, the curve shows some structural information, however, the second and third peaks are not separated due to a lack of data range. In addition, various oscillations are observed in all $G(\boldsymbol{r})$, which will be discussed later in Section 2.4.2.5. Detailed measurements are listed below in Table 2.4.8.

Table 2.4.8 Effect of data range selection on $G(\boldsymbol{r})$. Deviations of (a) peak positions and (b) amplitude of the first three peaks.

(a) Peak position	1st	2nd	3rd
$\boldsymbol{q}_{max}$ = 5Å^{-1}	1.59 (-1.85%)	N/A	N/A
$\boldsymbol{q}_{max}$ = 10Å^{-1}	1.62 (0%)	2.68 (+1.52%)	N/A
$\boldsymbol{q}_{max}$ = 15Å^{-1}	1.62 (0%)	2.64 (0%)	3.12 (0%)
$\boldsymbol{q}_{max}$ = 20Å^{-1}	1.62 (0%)	2.66 (+0.76%)	3.10 (-0.64%)
$\boldsymbol{q}_{max}$ = 25Å^{-1}	1.62 (0%)	2.65 (+0.38%)	3.11 (-0.32%)

Unit: Å (Relative error wrt $\boldsymbol{q}_{max}$ = 15Å^{-1})

(b) Peak amplitude	1st	2nd	3rd
$\boldsymbol{q}_{max}$ = 5Å^{-1}	1.569 (-60.78%)	N/A	N/A
$\boldsymbol{q}_{max}$ = 10Å^{-1}	3.389 (-15.28%)	0.769 (-43.77)	N/A
$\boldsymbol{q}_{max}$ = 15Å^{-1}	4.001 (0%)	1.367 (0%)	0.263 (0%)
$\boldsymbol{q}_{max}$ = 20Å^{-1}	4.002 (+0.03%)	1.435 (+4.99%)	0.341 (+29.57%)
$\boldsymbol{q}_{max}$ = 25Å^{-1}	4.139 (+3.48%)	1.393 (+1.86%)	0.390 (+48.13%)

Unit: a.u. (Relative error wrt $\boldsymbol{q}_{max}$ = 15Å^{-1})

Table 2.4.8 shows that the maximum deviation in all peak position is 0.04Å, corresponding to less than a 2% error. Comparing $\boldsymbol{q}_{max}$ < 15Å^{-1}, the deviation of the peak amplitude has an error about 60 and 15% for $\boldsymbol{q}_{max}$ = 5 and 10Å^{-1}, respectively. In contrast,

the peak amplitudes of $\boldsymbol{q}_{max}$ = 15, 20 and 25Å^{-1} have less than 5% variation in their first two peaks.

In summary, an insufficient data range ($\boldsymbol{q}_{max}$ < 15Å^{-1}) will causes an inaccuracy in $G(\boldsymbol{r})$ due to the lack of wave components in $\varphi(\boldsymbol{q})$. However, when $\boldsymbol{q}_{max}$ > 15Å^{-1}, the overall shape of $G(\boldsymbol{r})$ is less affected even with a selection of a longer data range because $G(\boldsymbol{r})$ is already accurately described by those wave components observed before 15Å^{-1}.

2.4.2.4 Effect of Chemical Composition on the RDF

Following Section 2.4.1.3, the fitting parameter f is related to the chemical composition of the materials. In the previous section, the specimen was amorphous SiO_2 which simply used a ratio of Si: O = 1: 2. However, in practice the composition of the material may be unknown. Therefore, it is useful to assess the influence on the RDF.

To study the effect of chemical composition, three compositions, Si_1O_0, Si_1O_1 and Si_1O_2 were applied in the fitting function. Figure 2.4.12 shows the three fitting curves with identical $I(\boldsymbol{q})$ data. Goodness-of-fit indices (R) are shown inset which can be defined as,

$$R = \left\{ \sum \left[I(\boldsymbol{q})_{exp} - I(\boldsymbol{q})_{fit} \right]^2 / \sum I^2(\boldsymbol{q})_{exp} \right\}^{\frac{1}{2}} \tag{2.10}$$

The index describes the deviation between $I(\boldsymbol{q})_{exp}$ and $I(\boldsymbol{q})_{fit}$, where smaller R means less deviation which result in better fitting. The resulting $\varphi(\boldsymbol{q})$ and $G(\boldsymbol{r})$ for different compositions computed from RDF analysis were compared and are shown in Figure 2.4.13 along with a comparison of peak positions and amplitudes in Table 2.4.9.

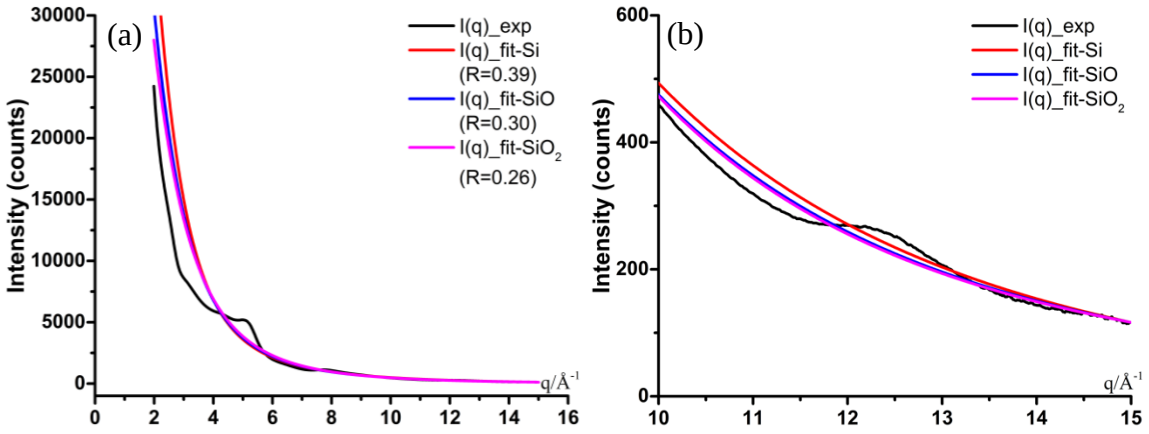


Figure 2.4.12 Effect of chemical composition on the RDF, $I(\boldsymbol{q})$ with fitted curves. (a) Full data range and (b) enlarged tail region.

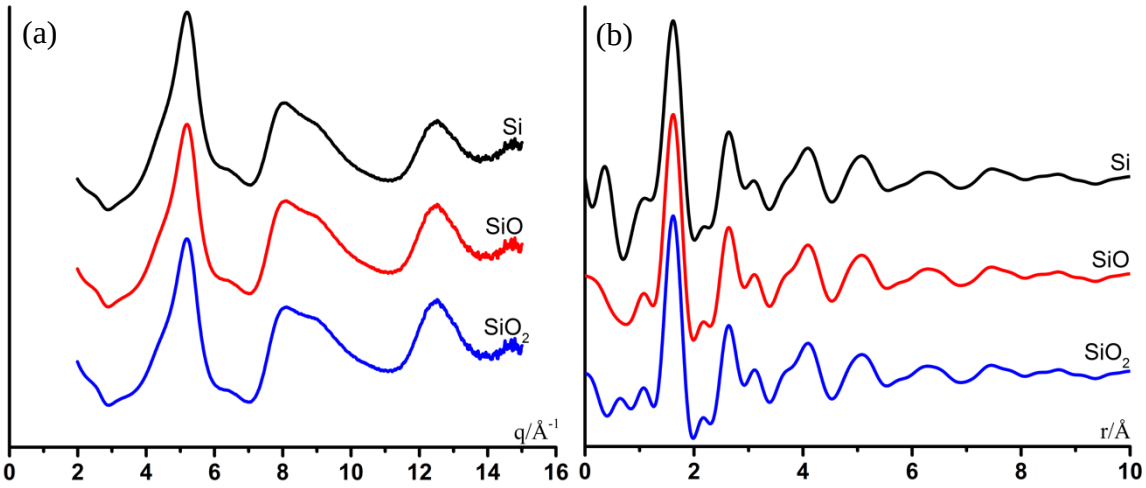


Figure 2.4.13 Effect of chemical composition on the RDF. (a) $\varphi(\boldsymbol{q})$ and (b) RDF curves extracted using three different compositions.

Table 2.4.9 Effect of chemical composition on $G(\boldsymbol{r})$. Deviations of (a) peak positions and (b) amplitude of the first three peaks.

(a) Peak position	1st	2nd	3rd
Si: O = 1: 0	1.62 (0%)	2.64 (0%)	3.09 (-0.64%)
Si: O = 1: 1	1.62 (0%)	2.64 (0%)	3.11 (0%)
Si: O = 1: 2	1.62 (0%)	2.64 (0%)	3.11 (0%)

Unit: Å (Relative error wrt Si: O = 1: 2)

(b) Peak amplitude	1st	2nd	3rd
Si: O = 1: 0	3.748 (-3.90%)	1.588 (+1.03%)	0.151 (-52.13%)
Si: O = 1: 1	3.915 (+0.37%)	1.614 (+2.70%)	0.264 (-16.12%)
Si: O = 1: 2	3.900 (0%)	1.572 (0%)	0.315 (0%)

Unit: a.u. (Relative error wrt Si: O = 1: 2)

Figure 2.4.12 shows that a composition Si: O = 1: 2 gives the best fit (R = 0.26) to $I(\boldsymbol{q})$. With decreasing O concentration, R increases by about 50% (R = 0.39). This misfit of $I(\boldsymbol{q})$ can be hardly be observed in the resulting $\varphi(\boldsymbol{q})$ shown in Figure 2.4.13 (a), however, it results in changes in $G(\boldsymbol{r})$ below 1Å where no contributions from interatomic distances are expected as shown in Figure 2.4.13 (b). Finally, Table 2.4.9 (a) shows that the peak position is identical for the first two peaks while the third peaks only varies by 0.02Å (0.6%) when using a pure silicon fitting. The peak amplitude as shown in Table 2.4.9 (b) shows similar results with less than 5% deviation in the first two peaks but with an error in the third peak of 16% and 52% for the Si_1O_1 and Si_1O_0 fitting, respectively.

2.4.2.5 Effect of a Damping Factor on the RDF

As mentioned earlier, the data range $\boldsymbol{q}$ is limited by the sensor in practical RDF analysis. This will result in oscillations after Fourier transformation. To explain this effect analytically, $G(\boldsymbol{r})$ is expressed as a Fourier Transform of $\varphi(\boldsymbol{q})$ as follows:

$$G(\boldsymbol{r}) = \mathcal{F}\big(\varphi(\boldsymbol{q})\big) = 4\int_0^{\infty} \varphi(\boldsymbol{q}) \sin(\boldsymbol{qr})\, d\boldsymbol{q} \tag{2.11}$$

In an experimental measurement, $\varphi(\boldsymbol{q})$ covers a limited range of data, denoted as $\boldsymbol{q}_{max}$. This can be expressed using a truncation function defined as;

$$\mathrm{A}(\boldsymbol{q}) = \begin{cases} 1, & \boldsymbol{q} \le \boldsymbol{q}_{max} \\ 0, & \boldsymbol{q} > \boldsymbol{q}_{max} \end{cases} \tag{2.12}$$

The Fourier Transform of A($\boldsymbol{q}$) is given by

$$\begin{aligned} \mathcal{F}[A(\boldsymbol{q})] &= 4\int_0^{\boldsymbol{q}_{max}} \sin(\boldsymbol{qr})\, d\boldsymbol{q} \\ &= 4\left(\frac{1-\cos(\boldsymbol{q}_{max}\boldsymbol{r})}{\boldsymbol{r}}\right) \end{aligned} \tag{2.13}$$

$G(\boldsymbol{r})_{exp}$ computed with $\boldsymbol{q}_{max}$ will thus be (where $\otimes$ is the convolution operator)

$$\begin{aligned} G(\boldsymbol{r})_{exp} &= \mathcal{F}[A(\boldsymbol{q})\varphi(\boldsymbol{q})] = \mathcal{F}[A(\boldsymbol{q})] \otimes \mathcal{F}[\varphi(\boldsymbol{q})] \\ &= 4\left(\frac{1-\cos(\boldsymbol{q}_{max}\boldsymbol{r})}{\boldsymbol{r}}\right) \otimes G(\boldsymbol{r}) \end{aligned} \tag{2.14}$$

Following the above equations, $G(\boldsymbol{r})$ can be regarded as a sum of wave functions $\sin(\boldsymbol{qr})$ with an amplitude of $\varphi(\boldsymbol{q})$. However, with a limited data range, $\boldsymbol{q}_{max}$, a frequency of $\boldsymbol{q}_{max}/2\pi$ and period of $2\pi/\boldsymbol{q}_{max}$ will be present due to the truncation function. For instance, if $\boldsymbol{q}_{max}$ = 15Å^{-1} is chosen, a period of $2\pi/\boldsymbol{q}_{max}$ = 0.42Å will be present as a period of oscillation in $G(\boldsymbol{r})$ which might be misleading. For a better representation, a damping term $D(\boldsymbol{q}) = \exp(-b\boldsymbol{q}^2)$ is generally applied to $\varphi(\boldsymbol{q})$ to suppress these oscillations in $G(\boldsymbol{r})$, where b is the damping factor.

The effect of damping factors on both $\varphi(\boldsymbol{q})$ and $G(\boldsymbol{r})$ is shown in Figure 2.4.14 with $\boldsymbol{q}_{max}$ = 15Å^{-1}. All curves were calculated from the diffraction pattern with the correct chemical composition (Si: O = 1: 2). Six different damping factors from 0 (un-damped) to 0.5 (heavily damped) were applied with an increment of 0.1.

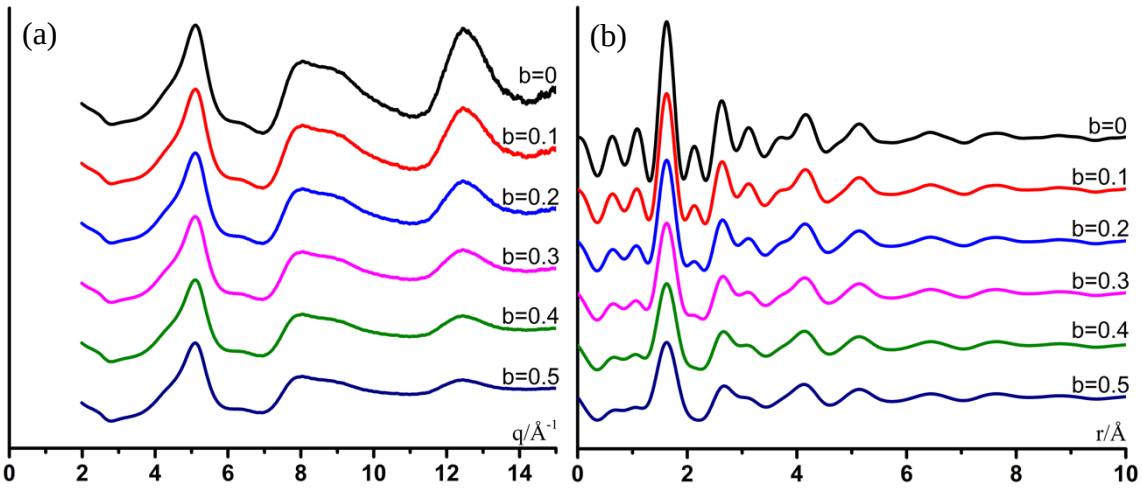


Figure 2.4.14 Effect of a damping factor on the RDF with $\boldsymbol{q}$ *=15Å^{-1}. (a)* $\varphi(\boldsymbol{q})$ *and (b) RDF curves extracted with different damping factors from 0 to 0.5.*

It can be seen from Figure 2.4.14 (a) that the un-damped $\varphi(\boldsymbol{q})$ (b = 0) shows strong interference up to 13Å^{-1}. Once a damping factor is applied, the intensity of the peaks starts to decrease and the intensity at high angle lies close to zero when b = 0.5. Figure 2.4.14 (b) illustrates the effects of different damping factors on $G(\boldsymbol{r})$. It can be seen that oscillations at 0.63, 1.09 and 2.13Å appear with an increment around 0.42Å when damping factors of 0 to 0.3 were applied, which is due to the limited data range of 15Å^{-1}. When applying a damping factor of 0.4 or greater, the intensity of the oscillations drops significantly due to heavily damped $\varphi(\boldsymbol{q})$ values. An analysis of $G(\boldsymbol{r})$ is shown in Table 2.4.10, indicating that the peak positions are relatively stable when the damping factor varies from 0 to 0.5. It can also be seen that the peak position shows little shift (maximum 0.04Å) corresponding to a 1% deviation. However, the peak amplitude shows a substantial change with the damping factor with a maximum deviation of up to two due to a significant reduction of wave components as a result of damping.

Table 2.4.10 Effects of the damping factor on $G(\boldsymbol{r})$. Deviations of (a) peak positions and (b) amplitude of the first three peaks.

(a) Peak position	1st	2nd	3rd
b = 0	1.62 (0%)	2.63 (-0.38%)	3.12 (0%)
b = 0.1	1.62 (0%)	2.64 (0%)	3.12 (0%)
b = 0.2	1.62 (0%)	2.64 (0%)	3.12 (0%)
b = 0.3	1.62 (0%)	2.65 (+0.38%)	3.11 (-0.32%)
b = 0.4	1.62 (0%)	2.66 (+0.76%)	N/A
b = 0.5	1.62 (0%)	2.67 (+1.14%)	N/A

Unit: Å (Relative error wrt b = 0.2)

(b) Peak amplitude	1st	2nd	3rd
b = 0	6.116 (+54.24%)	2.154 (+58.68%)	0.879 (+236.14%)
b = 0.1	4.866 (+22.25%)	1.687 (+19.45%)	0.506 (+93.32%)
b = 0.2	3.965 (0%)	1.357 (0%)	0.262 (0%)
b = 0.3	3.323 (-16.20%)	1.196 (-17.51%)	0.108 (-58.58%)
b = 0.4	2.864 (-27.76%)	0.945 (-30.35%)	N/A
b = 0.5	2.536 (-36.04%)	0.815 (-39.97%)	N/A

Unit: a.u. (Relative error wrt b = 0.2)

Besides the limited data range, noise acquired in experiments will also contribute to the oscillation in $G(\boldsymbol{r})$. To test this, a diffraction pattern from Figure 2.4.10 was used with a longer data range up to 25Å^{-1} where noise is present at higher angles.

Figure 2.4.15 shows the effect of damping factors on both $\varphi(\boldsymbol{q})$ and $G(\boldsymbol{r})$ with $\boldsymbol{q}_{max}$ = 25Å^{-1}. RDF analysis were performed using identical setups as before with damping factors from 0 to 0.5.

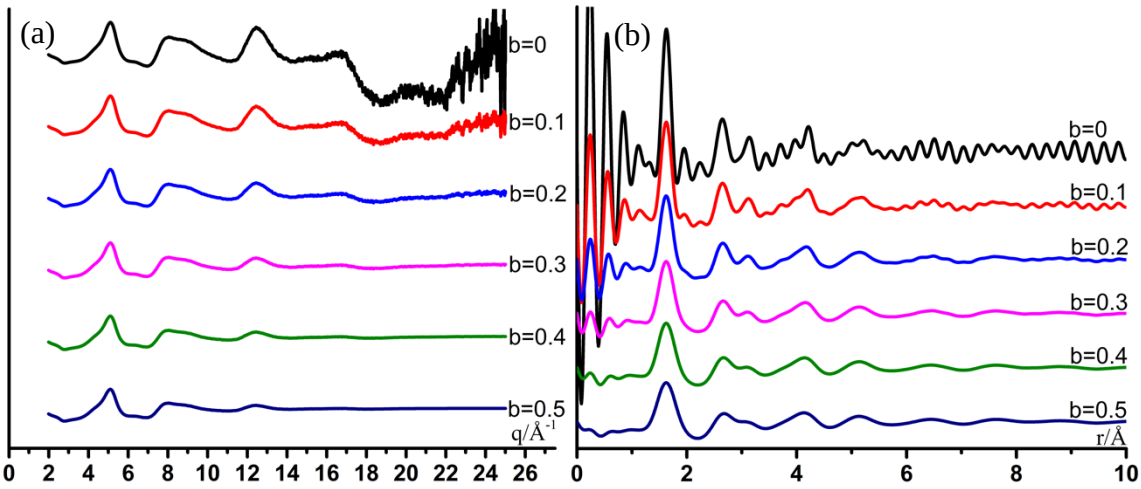


Figure 2.4.15 Effect of a damping factor on the RDF with $\boldsymbol{q}$=25Å^{-1}. (a) $\varphi(\boldsymbol{q})$ and (b) RDF curves extracted with different damping factors from 0 to 0.5.

Figure 2.4.15 (a) shows that the large contributions from noise at high $\boldsymbol{q}$ (b = 0) are damped to different levels when damping factors varying from 0.1 to 0.5 were applied, whereas Figure 2.4.15 (b) illustrates the effects of different damping factors on $G(\boldsymbol{r})$. Significant oscillations with a period around 0.25Å ($2\pi/\boldsymbol{q}_{max}$) can be observed in $G(\boldsymbol{r})$ with b = 0 and 0.1 along the whole curve. Comparison with to Figure 2.4.14, shows that the presence of noise leads to much stronger oscillations in $G(\boldsymbol{r})$, and to minimize the oscillation, damping factors of more than 0.2 are needed. Detailed analysis of peak positions and amplitudes have been measured and are given in Table 2.4.11.

Table 2.4.11 Effects of the damping factor on $G(\boldsymbol{r})$. Deviations of (a) peak positions and (b) amplitude of the first three peaks.

(a) Peak position	1st	2nd	3rd
b = 0	1.63 (+062%)	2.65 (0%)	3.14 (+0.96%)
b = 0.1	1.62 (0%)	2.65 (0%)	3.12 (+0.32%)
b = 0.2	1.62 (0%)	2.65 (0%)	3.11 (0%)
b = 0.3	1.62 (0%)	2.66 (+0.38%)	3.10 (-0.32%)
b = 0.4	1.62 (0%)	2.67 (+0.75%)	N/A
b = 0.5	1.62 (0%)	2.68 (+1.13%)	N/A

Unit: Å (Relative error wrt b = 0.2)

(b) Peak amplitude	1st	2nd	3rd
b = 0	8.148 (+96.53%)	2.811 (+101.68%)	1.347 (+248.0%)
b = 0.1	5.416 (+30.62%)	1.832 (+31.42%)	0.743 (+91.86%)
b = 0.2	4.146 (0%)	1.394 (0%)	0.387 (0%)
b = 0.3	3.401 (-17.97%)	1.145 (-17.84%)	0.170 (-58.18%)
b = 0.4	2.954 (-28.96%)	0.967 (-30.66%)	N/A
b = 0.5	2.625 (-36.69%)	0.8324 (-40.29%)	N/A

Unit: a.u. (Relative error wrt b = 0.2)

Table 2.4.11 shows that the peak positions are stable while the peak amplitudes changes significantly, similar to measurements of $\boldsymbol{q}$ = 15Å^{-1}. It can be seen that the peak position has a shift of less than 0.03Å with an error of 1%. Comparing the peak amplitude to previous measurements (Table 2.4.10), the deviations when b = 0 and 0.1 became larger on the first and second peaks which is due to the presence of noise. Once b is greater than 0.2, the noise was damped and the relative errors are similar to previous results. In addition, a small deviation of about 5% (for the 1st and 2nd peak) is observed comparing both $b =$

0.2 to 0.5 data with $\boldsymbol{q}$ = 15 and 25Å^{-1} which is due to the selection of the data range as described in Section 2.4.2.3.

2.4.2.6 Summary

In this section, five factors that affect the accuracy of RDF analysis have been explored; the calibration factor $\delta\boldsymbol{q}$, the centre location of the diffraction pattern, the choice of data range $\boldsymbol{q}$, the chemical composition and the damping factor b.

These results indicate that a 1% error in calibration factor has a small impact on peak position (0.03Å, 1.2%) and the peak amplitude (less than 3%). However, it is worth noting that a typical maximum experimental error in a diffraction pattern only deviates by 0.17% while the error introduced by hysteresis after a month is 0.69% (see Section 2.4.1.2).

Using eRDF Analyser [43], a centre optimisation routine was applied with a maximum pixel shift of less than 2 pixels. This gives no deviation in peak position and an insignificant effect on peak amplitude with less than 3% error.

In the selection of the data range, a data range $\boldsymbol{q}$ of up to 15Å^{-1} is recommended to give enough interference in $\varphi(\boldsymbol{q})$ for accurate RDF extraction, whilst $\boldsymbol{q}_{max}$ up to 25Å^{-1} gives consistent results with less than 5% variation.

The results from the selection of chemical composition suggest that any inaccuracy in composition gives rise to a negligible effect on the peak positions with an error of 4% for the first and second peak.

Finally, the use of a damping term $D(\boldsymbol{q}) = \exp(-b\boldsymbol{q}^2)$ was applied to suppress the oscillations cause by a limited data range and noise. A damping factor b = 0.2 is needed to reduce the oscillation while maintaining useful data.

Overall, using a 216Å amorphous SiO_2 thin film, the above analyses have demonstrated that the RDF analysis is accurate and reliable for practical studies of amorphous materials.

Chapter 3 Factors Affecting Experimental RDF Analysis

In the previous chapter, a brief history of RDF analysis was presented and the computational factors that affect the analysis, from calibration to data damping, were discussed. These results indicate that RDF analysis is robust with respect to data processing. There can be, however, various experimental conditions that can influence the RDF analysis. Therefore, the effects of experimental factors, such as sample thickness, noise, beam coherence and electron dose on the RDF are described in this chapter.

3.1 Experimental and Simulation Setup

3.1.1 RDF Acquisition

To test the influence of sample thickness on the RDF, electron diffraction patterns were recorded using a JEOL-2100 microscope equipped with a 2048 x 2048 pixel camera (Gatan, Orius SC200). The setup of the microscope was identical to the one described previously in Section 2.4.1. To test the influence of noise, coherence and dose on the RDF, a double-corrected Grand-ARM300F microscope fitted with two detectors, a 4096 x 4096 pixel camera (Gatan, OneView) and a 256 x 256 pixel direct electron counting detector (Quantum Detectors, Medipix3), was used.

Measurements of the calibration factor, $\delta\boldsymbol{q}$, were performed during each microscope session and the RDF curves, $G(\boldsymbol{r})$, were computed using the procedures described earlier. For each specimen, the method of analysis was identical.

3.1.2 DFT Simulations

DFT simulations were carried out to help with the interpretation of the structural data. First, a charge-balanced initial model was built by distributing atoms randomly within a supercell as shown in Figure 3.1.1 (a). A basic geometry optimisation was then applied to adjust unphysical atomic distances as shown in Figure 3.1.1 (b). This used a repulsive soft spherical potential based on each atoms covalent radius and the atomic position was adjusted if the atomic distance between two atoms was smaller than the sum of their radii.

Next, the optimised model was input into CASTEP (Cambridge Serial Total Energy Package) software [50] for DFT molecular dynamics simulation. The input parameters use a Perdew-Burke-Ernzerhof (PBE) exchange correlation functional [51] and a cut-off energy, which will be discussed later, was set to 300eV. The temperature control was implemented by Nose-Hoover chain method [52] within a canonical ensemble (NVT). The model was first melted at 3000K for 2ps and then gradually cooled to 2000K over 10ps. The melt was then further quenched to 300K in steps with a cooling rate of $1.5 \cdot 10^{14}$K/s. Figure 3.1.1 (d) shows the energy of the model throughout the quench procedure. Finally, the quenched models were energy optimised to find their most stable structure as shown in Figure 3.1.1 (c).

In this study, DFT simulations with around 100 atoms were used to balance computational time and the reliability of the result. The averaged bond lengths obtained from the DFT models were then used as constraints in the RMC refinement process.

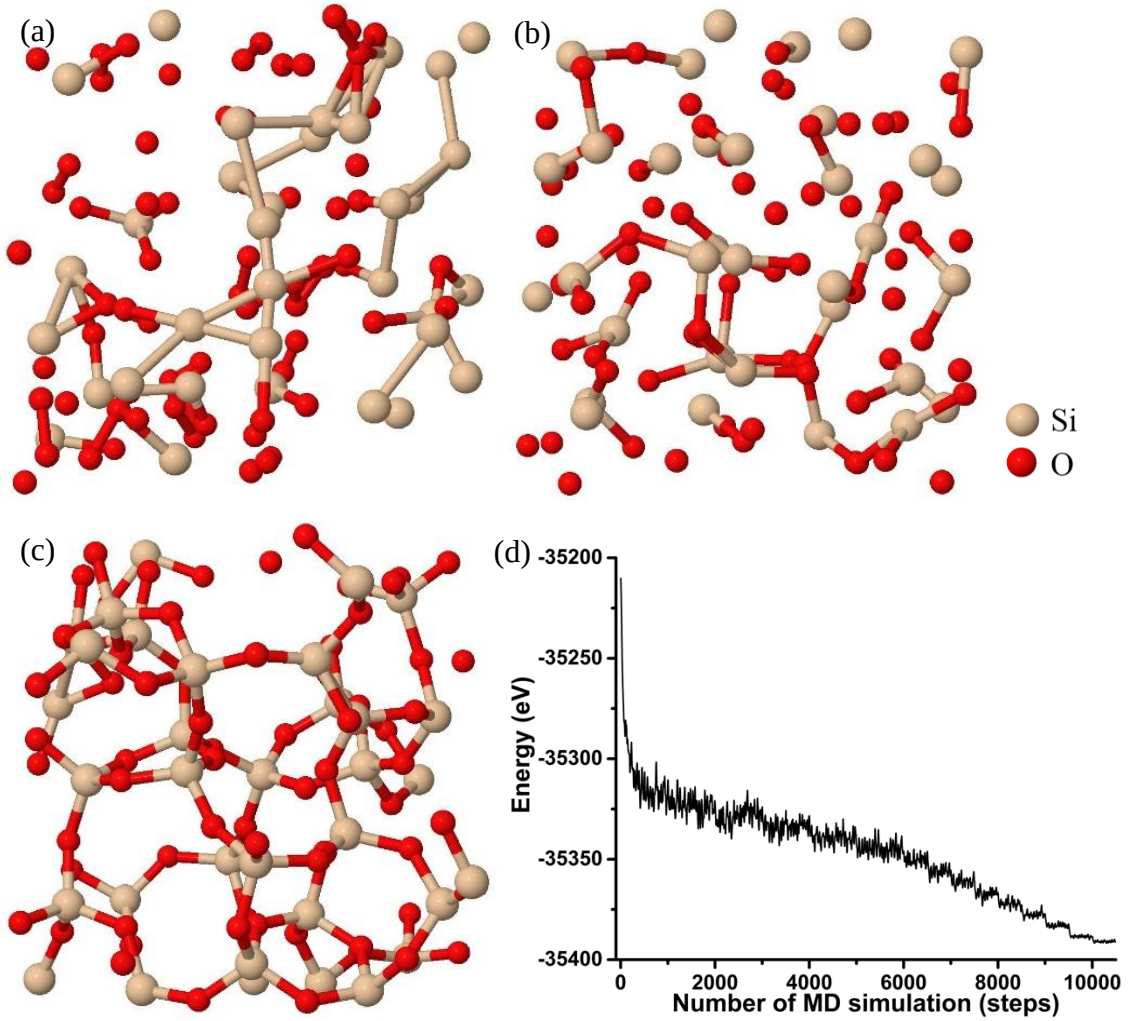


Figure 3.1.1 Example simulation for amorphous SiO_2. (a) An initial charge-balanced model with 102 atoms, (b) the same model after geometry optimisation using a soft spherical potential and (c) the model after DFT MD simulation. (d) Potential energy states throughout the DFT simulation process.

For accurate simulation, the correct basis set is an important parameter that needs to be determined. This is controlled by the cut-off energy that fixes the number of plane waves in the basis set which in principle is otherwise infinite.

However, the truncation of the basis set at a finite cut-off energy will lead to an error in the computed total energy and its derivatives. To reduce this error it is necessary to increase the value of the cut-off energy until the calculated total energy converges within the required tolerance. Since a higher cut-off energy will result in longer computational time, the aim is to find the lowest cut-off energy which can produce consistent results to balance it. Figure 3.1.2 shows the resulting $G(\boldsymbol{r})$ curves derived with different cut-off energies from 100-600eV.

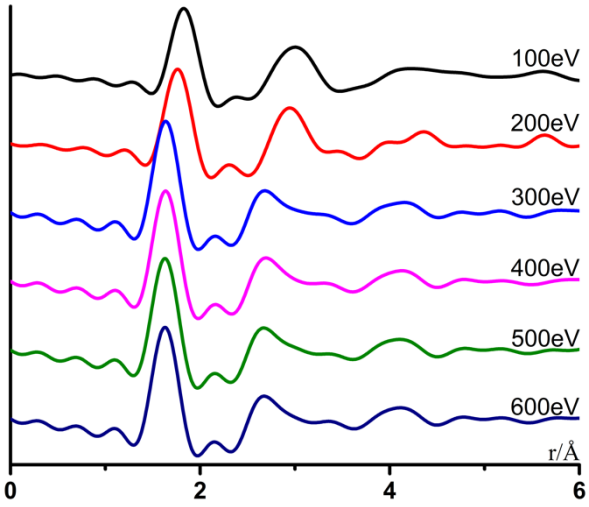


Figure 3.1.2 $G(\boldsymbol{r})$ curves extracted with various cut-off energies from 100-600eV.

It can be seen from Figure 3.1.2 that $G(\boldsymbol{r})$ extracted with cut-off energies of 300-600eV give identical results with a first peak at around 1.63Å. In contrast, curves extracted with 100 and 200eV cut-off energies show distinct differences with longer first neighbour distances of 1.83Å and 1.76Å due to the limited cut-off energy. Therefore, in the following simulations a cut-off energy of 300eV was used to ensure an accurate output whilst saving computational time.

3.1.3 RMC Refinements

Due to various limiting parameters in the DFT simulations such as small model size, short simulation time, low cut-off energy and the use of rigid periodic boundary conditions, computational errors may be introduced to the resulting configurations. Therefore, the DFT-optimised models were refined using a Reverse Monte Carlo (RMC) refinement procedure by comparing $\varphi(\boldsymbol{q})$ calculated from the structures to the experimental $\varphi(\boldsymbol{q})$ data. This refinement is a way to solve the inverse problem of finding an unknown structural model from the experimental scattering data. Figure 3.1.3 illustrates the RMC refinement process for which detailed information can be found in the paper by McGreevy [53].

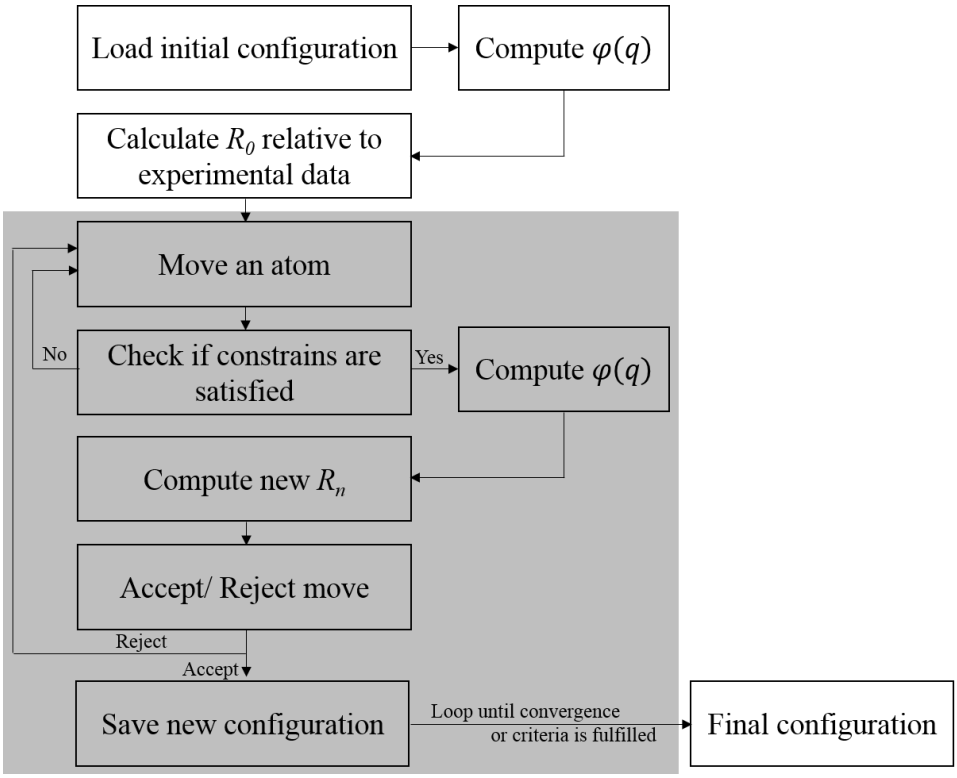


Figure 3.1.3 Algorithm for RMC refinement taken from [53].

The refinement process starts by loading an initial configuration which in our case is a DFT simulated model. The software calculates $\varphi(\boldsymbol{q})$ from the model and automatically compares it to $\varphi(\boldsymbol{q})_{exp}$. A goodness-of-fit index, R_0, (see Equation 2.10), is then calculated and thus an atom will be moved. The refinement is an iterative progress moving one atom each time and accepting/rejecting each move based a set of constraints and a goodness-of-fit index. If the movement violates any constraint, the step will be rejected. Once all constrains are satisfied, the system computes a new R_n and decides whether the move will be accepted or rejected. After a designated number of iterations, R will decrease to a minimum in the final configuration.

It is important to note that contribution of the scattering intensity components to peaks below 1.1Å in the experimental RDF, where no contributions from the interatomic distance are expected, were removed using a Fourier filter before refinement. The software filters out the low-frequency contributions in Fourier space and outputs the filtered $G(\boldsymbol{r})$ and Figure 3.1.4 shows the $\varphi(\boldsymbol{q})$ and $G(\boldsymbol{r})$ before and after filtering.

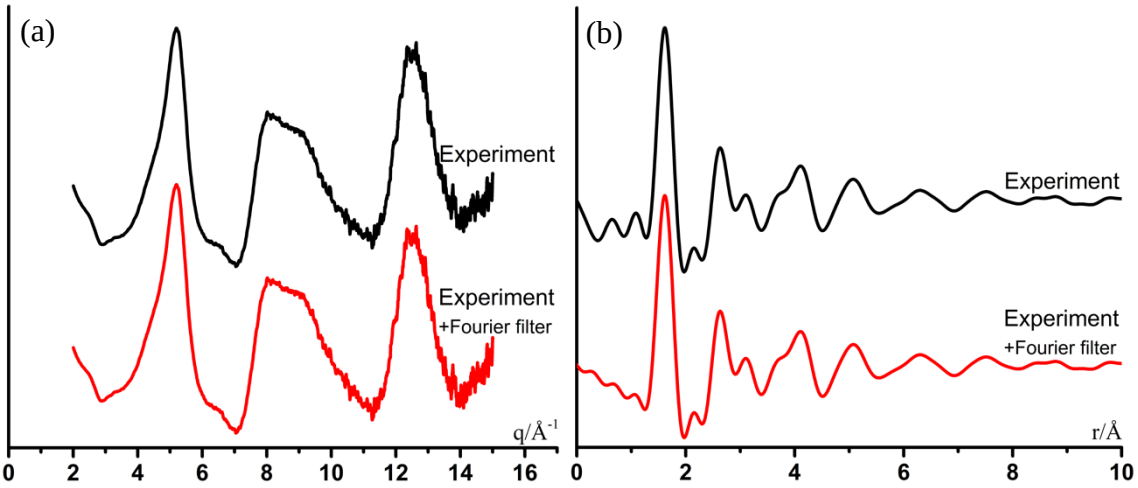


Figure 3.1.4 (a) $\varphi(\boldsymbol{q})$ and (b) $G(\boldsymbol{r})$ before and after the Fourier filtering.

It can be seen from Figure 3.1.4 (a) that the overall shape of $\varphi(\boldsymbol{q})$ before and after filtering is identical while peaks below 1.1Å in the corresponding $G(\boldsymbol{r})$ curve are removed.

After Fourier filtering, the RMC refinement was performed assuming periodic boundary conditions in all three dimensions. The maximum movement range for each step was set to be 0.2Å and constraints (e.g. Si-O, Si…Si and O…O distances), obtained from DFT simulation, were added to avoid unphysical atomic distances. Figure 3.1.5 shows the models and the RDF analysis before and after RMC refinement.

Both the Fourier filters and the RMC programme used in this thesis were developed by Dr Konstantin Borisenko at the University of Oxford.

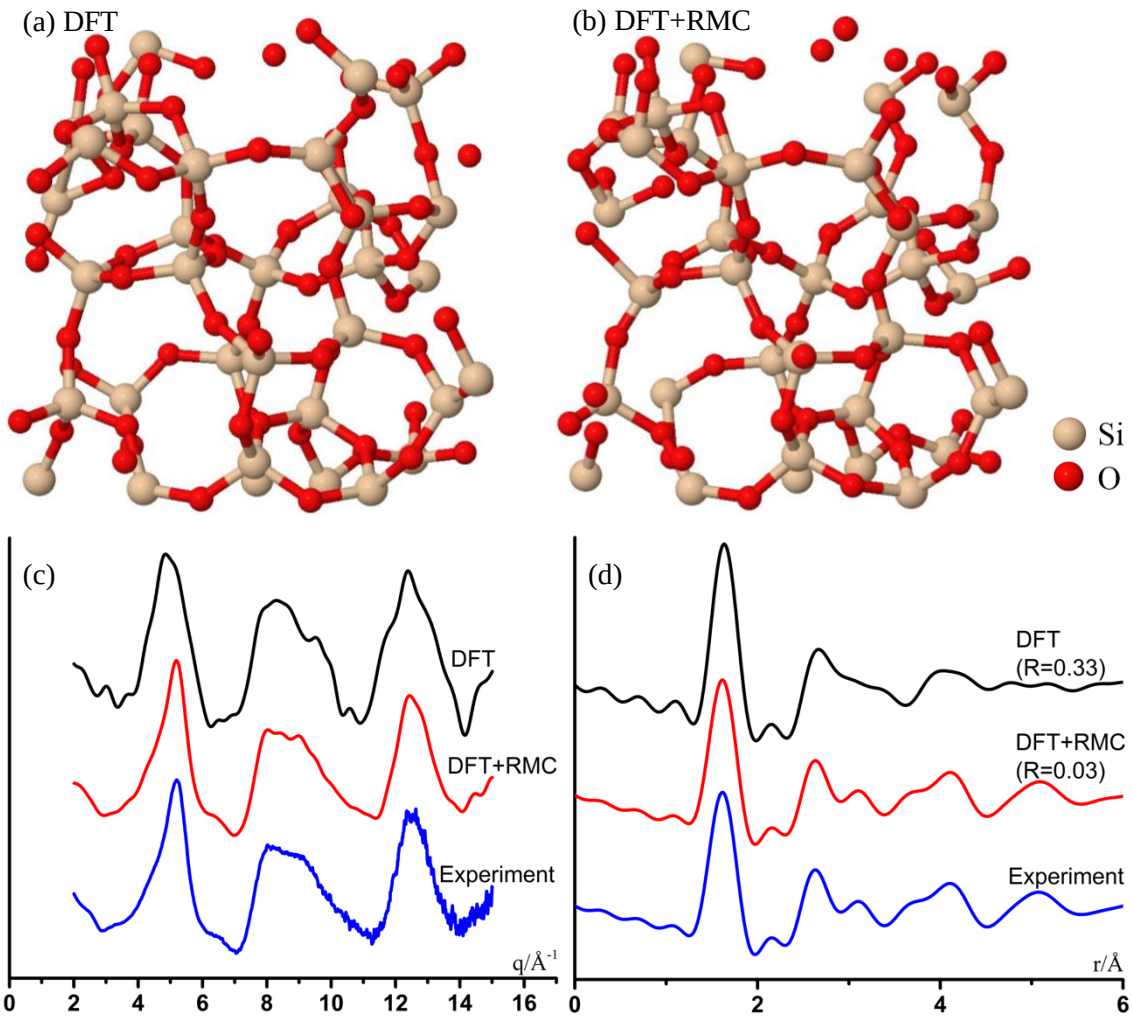


Figure 3.1.5 (a, b) DFT Models before and after RMC refinements along with their corresponding (c) $\varphi(\boldsymbol{q})$ and (d) $G(\boldsymbol{r})$.

Figures 3.1.5 (a) and (b) show the atomic models before and after RMC refinement. It can be seen that the overall tetrahedral structure remains unchanged after the RMC refinement owing to the constraints applied. Figures 3.1.5 (c) and (d) show the corresponding $\varphi(\boldsymbol{q})$ and $G(\boldsymbol{r})$ curves after the RDF analysis and the results suggest that $\varphi(\boldsymbol{q})$ before RMC (Figure 3.1.5 (c) black curve) already has a similar trend with four major peaks around 5,

8, 9 and 12.5Å^{-1} compared to the experimental data. After refinement, the overall shape of the refined $\varphi(\boldsymbol{q})$ (Figure 3.1.5 (c) red curve) fits better to the experimental data. The same results also applied to $G(\boldsymbol{r})$ with R decreasing from 0.33 to 0.03, indicating an improved agreement with the experiment. A detailed comparison between bond angles and bond types for these two models are shown in Figure 3.1.6.

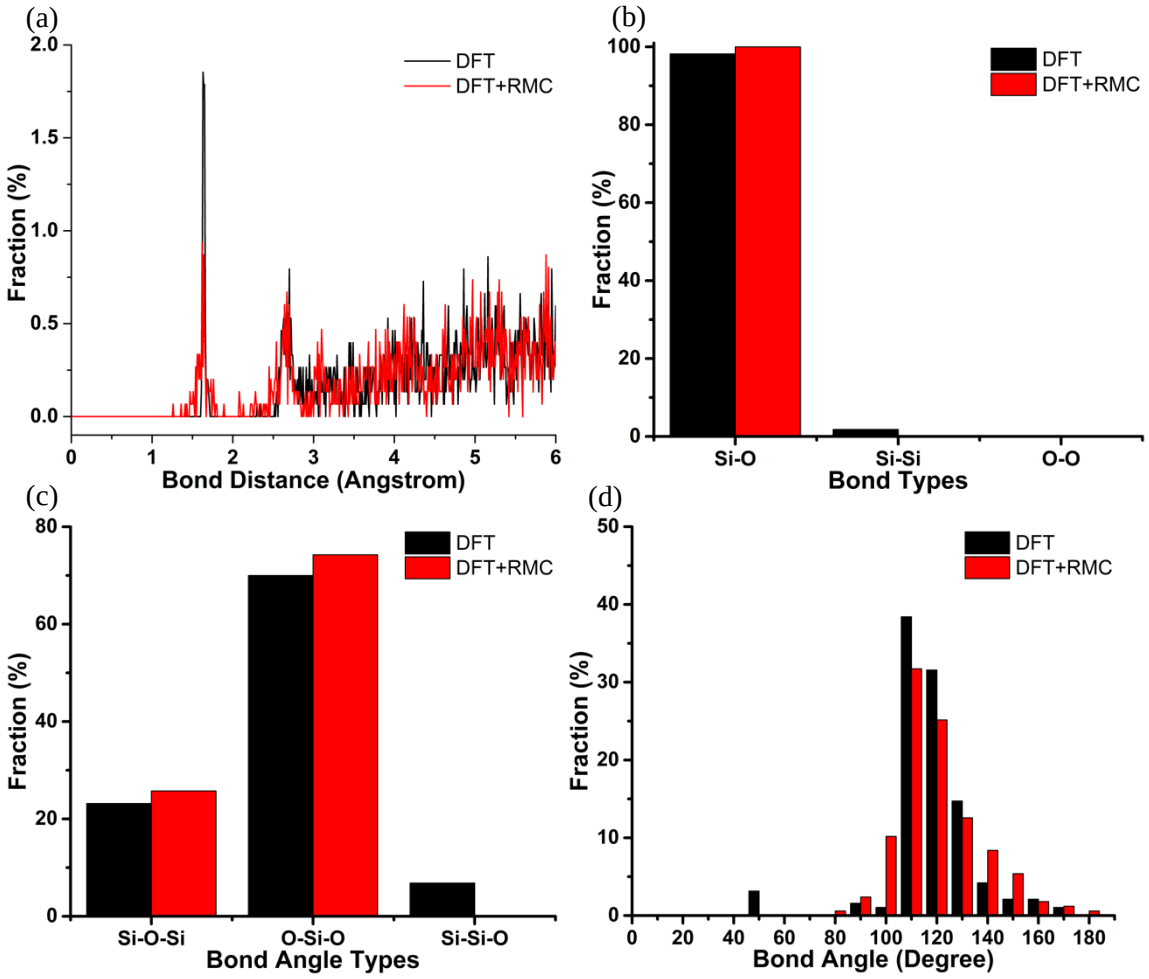


Figure 3.1.6 Comparison of the models before and after RMC refinement. (a) Bond distance distributions, (b) Bond types, (c) Bond angle types and (d) Bond angle distributions.

The bond distance distributions shown in Figure 3.1.6 (a) indicate that there are fewer Si-O bonds around 1.6Å after RMC refinement, and more Si…Si distances around 3.1Å matching the experimental data. Figure 3.1.6 (b) shows the bond type distribution before and after RMC refinements, suggesting that there were 2% of Si-Si bonds in the model before the refinement. However, in the refined model only Si-O bonds are present. Since no more Si-Si bonds were present in the refined model, the 7% contribution to the Si-Si-O bond angle, before refinement is distributed between Si-O-Si and O-Si-O. Figure 3.1.6 (c) shows that both models have the same ratio of 1:3 between Si-O-Si to O-Si-O angles, as expected in a SiO_2 tetrahedral structure as shown in Figure 3.1.7 below. Finally, Figure 3.1.6 (d) shows the bond angle distributions in both models. The first peak at 50^o comes from Si-Si-O bond angles which no longer exist in the model after RMC refinement. The bond angles around 110-130^o mainly corresponds to the inner-tetrahedral O-Si-O angle which decreased after the refinement and angles over 130^o which are the outer-tetrahedral Si-O-Si angles increased (see Figure 3.1.7).

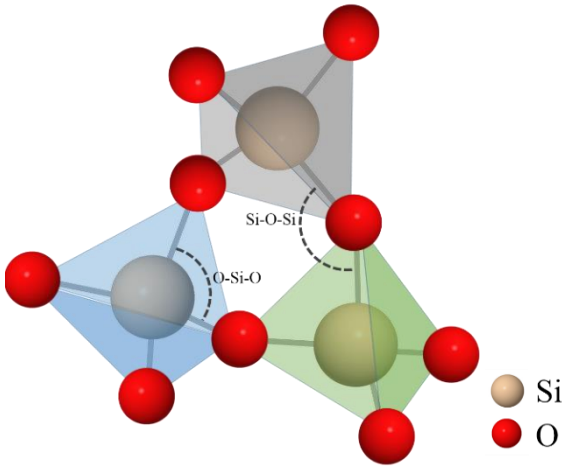


Figure 3.1.7 Schematic SiO2 tetrahedral structure.

In addition, the average coordination numbers of Si (Z_{Si}) and O (Z_O) were computed from both models. The results show that $Z_{Si} = 3.86$ and $Z_O = 1.85$ for the DFT model which are very close to the theoretical value of $Z_{Si} = 4$ and $Z_O = 2$. After the RMC refinement, $Z_{Si} = 3.57$ and $Z_O = 1.78$ were obtained.

To conclude, DFT model does not fit well ($R = 0.33$) to the experimental data owing to possible limiting parameters such as short simulation time and the use of rigid periodic boundary conditions. Hence, the RMC refinement was performed and the results indicate an improved agreement with the experiment with R decreasing from 0.33 to 0.03. Although RMC refinement suffers from some potential arguments such as more than one output will give similar agreement with experimental data, the results suggest that with appropriate use of constraints the output model can provide a good interpretation of the averaging structural information.

3.2 Effect of Sample Thickness on the RDF

The kinematic scattering approximation is often used for interpretation of electron diffraction data, which assumes that only one scattering event occurs for each electron passing through the specimen. However, in practice, the electrons are multiply scattered. The contribution of multiple scattering will increase as the sample thickness increases, and since the RDF analysis is usually based on single scattering approximation, this may be inadequate for accurate interpretation of thicker samples. It is therefore important to know the specimen thickness limitation for which the single scattering approximation is still valid.

To study the effect of sample thickness on the RDF experimentally, three commercial amorphous SiO_2 films (Agar Scientific Ltd, UK) were examined. Although the thickness of each film was given by the company as 80, 180 and 400Å, EELS data were used for confirmation. By averaging over three windows in each film, the results show that the t/λ (t is the thickness and λ is the mean free path) ratio for thin, medium and thick films are 0.34, 0.37 and 0.73 with standard deviation of 0.02, 0.04 and 0.01, respectively. Following Malis et al. [54], the mean free path of SiO_2 at 80kV within an angular collection angle up to 50mrad was estimated as $\lambda = 640.5 \pm 64$Å (error of ±10%). Therefore, the thickness of each film was calculated and that the nominal 80, 180 and 400Å films have true thicknesses of 216±26, 234±36 and 471±47Å, respectively.

After the thicknesses were confirmed, diffraction patterns from each film were captured under the same conditions, and their corresponding azimuthally averaged intensity distribution functions $I(\boldsymbol{q})$ are shown in Figure 3.2.1.

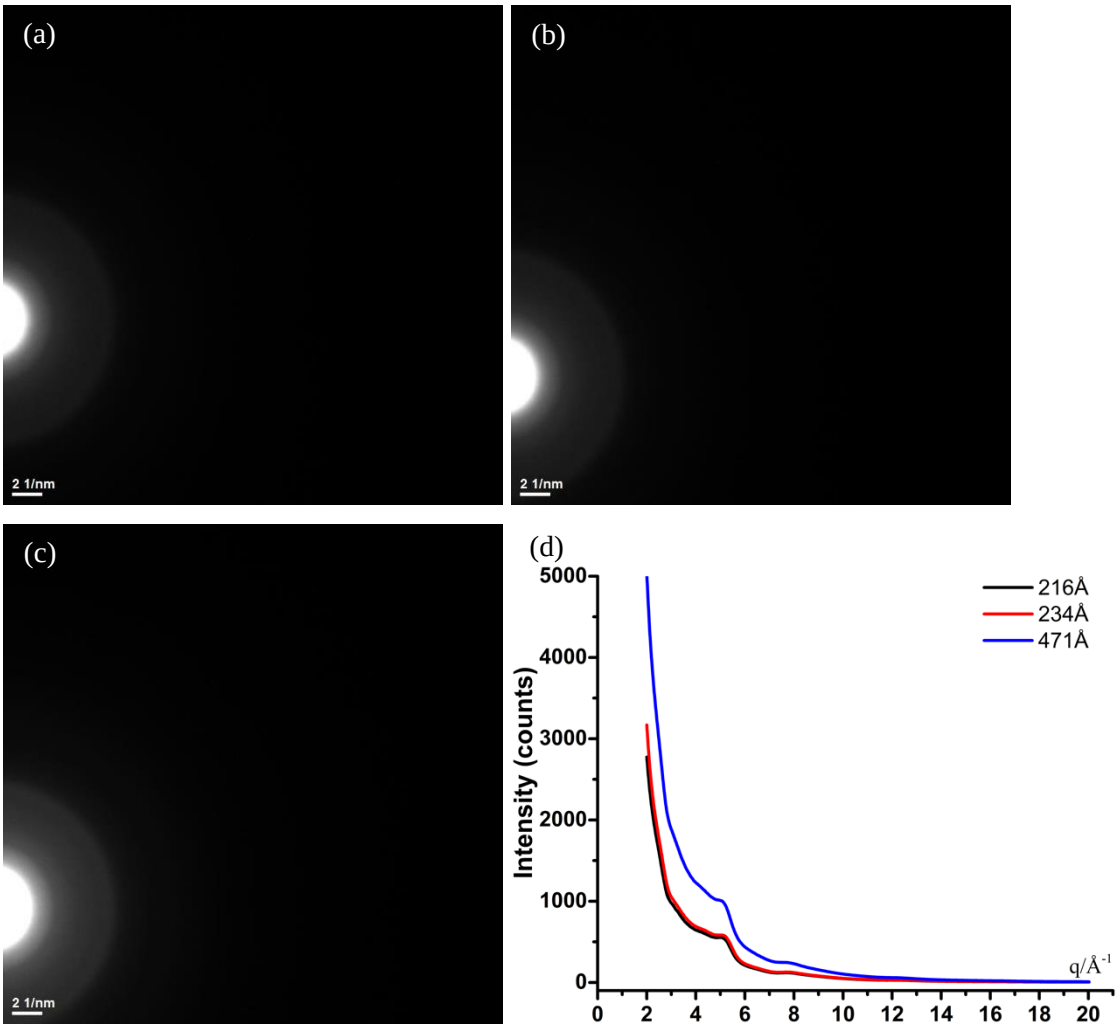


Figure 3.2.1 Diffraction patterns of amorphous SiO_2 specimen of various thicknesses (a) 216Å, (b) 234Å (c) 471Å and (d) their corresponding intensity distribution functions.

From Figure 3.2.1 (d), it can be seen that $I(\boldsymbol{q})$ from the 216Å film is just slightly stronger than the 234Å film owing to their small variation in thicknesses, while $I(\boldsymbol{q})$ of the 471Å film shows distinct higher counts compared to the others. RDF analysis was then performed and the resulting $I(\boldsymbol{q})$ background fittings, $\varphi(\boldsymbol{q})$ and $G(\boldsymbol{r})$ are shown in Figure 3.2.2. Meanwhile, measurements of peak position and amplitude are given in Table 3.2.1.

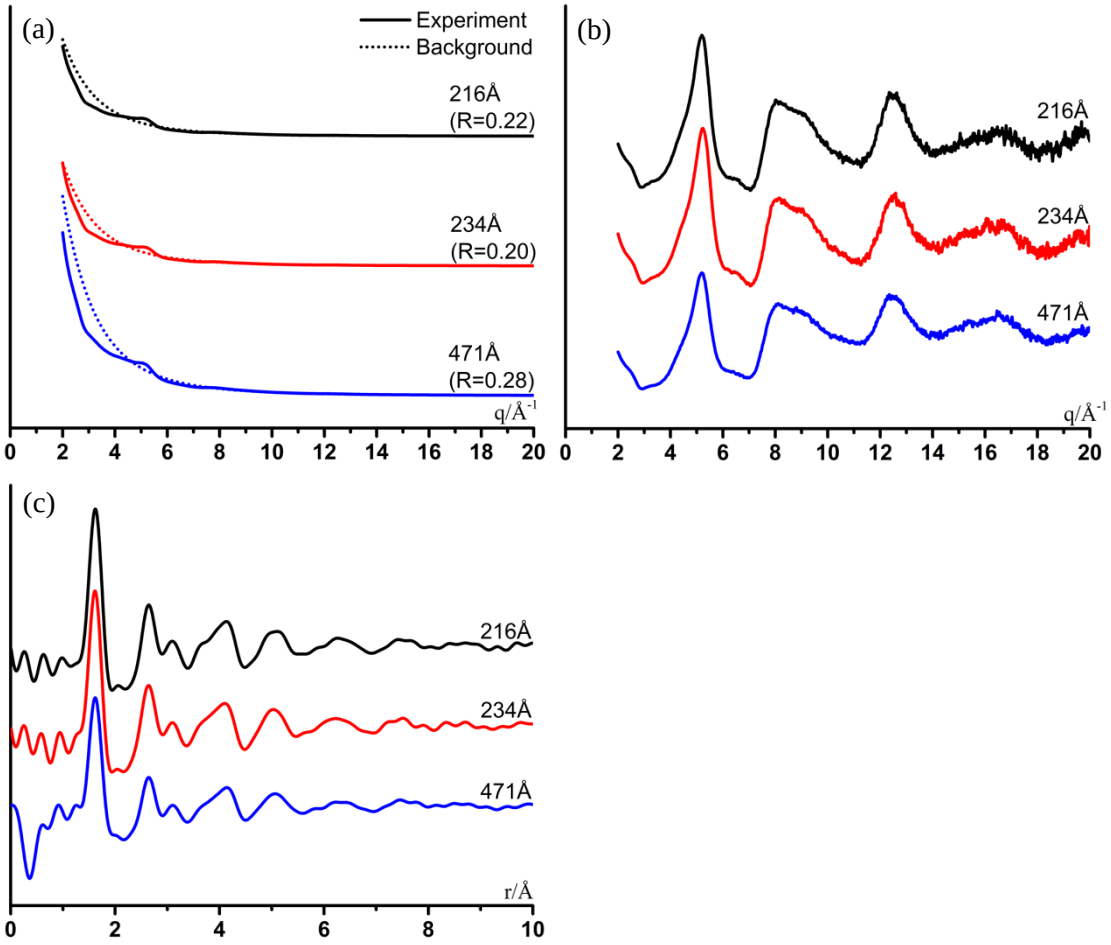


Figure 3.2.2 Effect of sample thickness on the RDF. (a) $I(\boldsymbol{q})$ background fittings, (b) $\varphi(\boldsymbol{q})$ and (c) $G(\boldsymbol{r})$ extracted from patterns from 216, 234 and 471Å amorphous SiO_2 films.

Table 3.2.1 Effect of sample thickness on $G(\boldsymbol{r})$. Deviations of (a) peak positions and (b) amplitude of the first three peaks.

(a) Peak position	1st	2nd	3rd
216Å	1.62 (0%)	2.64 (0%)	3.09 (0%)
234Å	1.61 (+0.62%)	2.64 (0%)	3.10 (+0.32%)
471Å	1.62 (0%)	2.64 (0%)	3.10 (+0.32%)

Unit: Å (Relative error wrt 216Å)

(b) Peak amplitude	1st	2nd	3rd
216Å	3.931 (0%)	1.581 (0%)	0.321 (0%)
234Å	4.045 (+2.91%)	1.509 (-4.53%)	0.304 (-5.32%)
471Å	3.041 (-22.64%)	1.116 (-29.39%)	0.260 (-19.08%)

Unit: a.u. (Relative error wrt 216Å)

From the resulting $I(\boldsymbol{q})$ background fits as shown in Figure 3.2.2 (a), noticeable differences at low scattering angle ($\boldsymbol{q}$ from 2 to 4Å^{-1}) can be observed when comparing the 471Å film to the others. Using the goodness-of-fit index *R*, it can be seen that the fitting of the atomic scattering background for thinner specimens gives a better agreement (R = 0.2) as compared to the thicker film (R = 0.3). This will impact the output $\varphi(\boldsymbol{q})$ and $G(\boldsymbol{r})$ as shown in Figures 3.2.2 (b) and (c). The measurements of $G(\boldsymbol{r})$ curves are given in Table 3.2.1 showing that the peak position and amplitude of the 216Å and 234Å films are within 0.01Å and around 5% difference, respectively. Although the peak position of the 471Å film has only a 0.01Å error, the peak amplitude shows a large deviation of up to 23% and 29% for the 1st and 2nd peaks.

Beside the experimental observation as described above, simulations using the multislice method proposed by Cowley and Moodie [55, 56] were used to estimate the effect of multiple scattering. An illustration of multislice simulation is shown in Figure 3.2.3. Using this approach, a model is input (Figure 3.2.3 (a)) and divided into a series of slices and the potential of each slice is projected onto a plane at which the electron scattering occurs (Figure 3.2.3 (b)). The electron wavefront is propagated between the slices to give a resulting exit wave which can be computed into diffraction pattern (Figure 3.2.3 (c)).

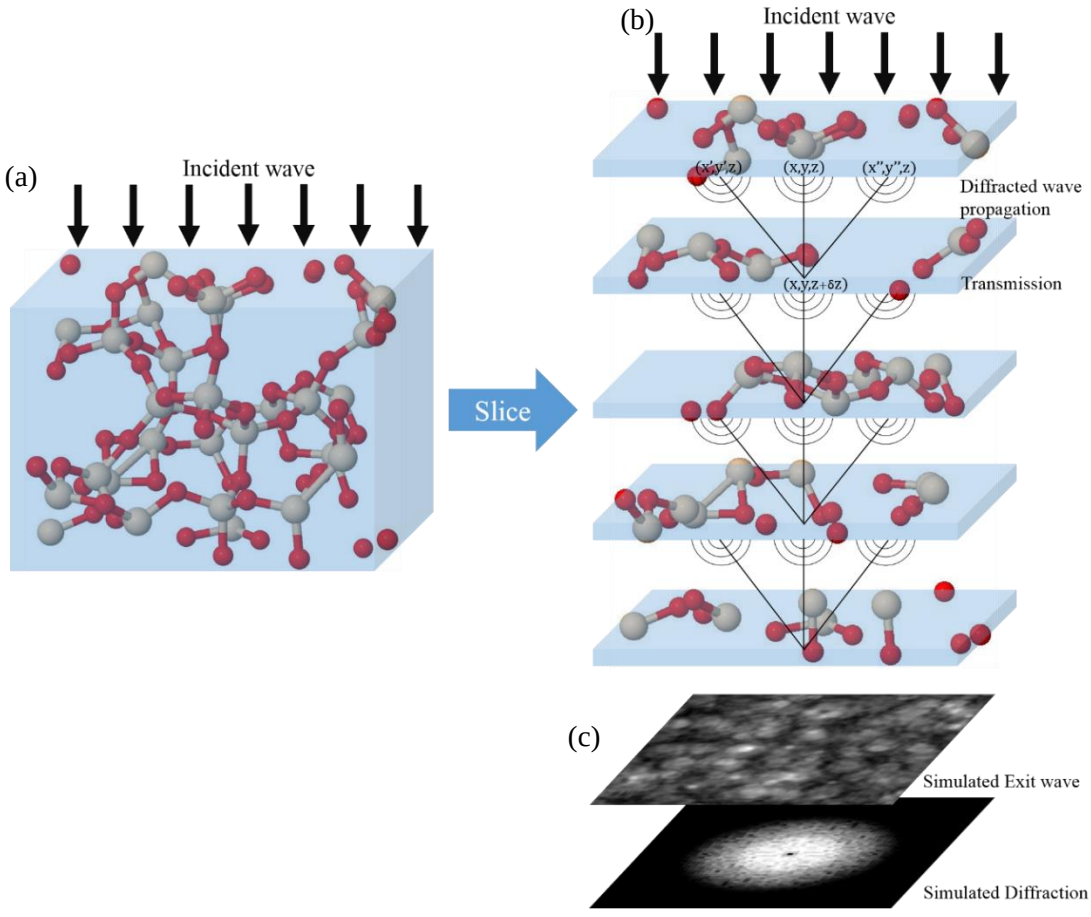


Figure 3.2.3 Illustration of multislice simulation. (a) Input model. (b) Model slices, wave propagation and transmission. (c) Resulting exit wave and diffraction pattern.

To perform the multislice simulations, Kirkland's multislice code [17] was used. For better approximation of the experimental data, a large input model is recommended to prevent the formation of periodicity during model extension. Therefore, a large model of an amorphous SiO_2 block with 3000 atoms by Le Roux and Petkov [57] was used. The model was generated by RMC with guided by synchrotron X-ray radiation data and Figure 3.2.4 (a) shows the atomic structure of the model.

Once the selected model is input, the software can extend it vertically to achieve thicknesses of 216, 234 and 471Å to match those determined experimentally. This extension has to be done randomly to avoid periodicity and the resulting models of various thicknesses are shown in Figure 3.2.4 (b). The multislice calculations were carried out with a slice thickness of 2Å (thin enough to be regard as a weak phase object [58]), and the resulting exit wave was output and its diffraction pattern computed from square modulus of the Fourier transform of the exit wave which was then used in turn for further RDF analysis.

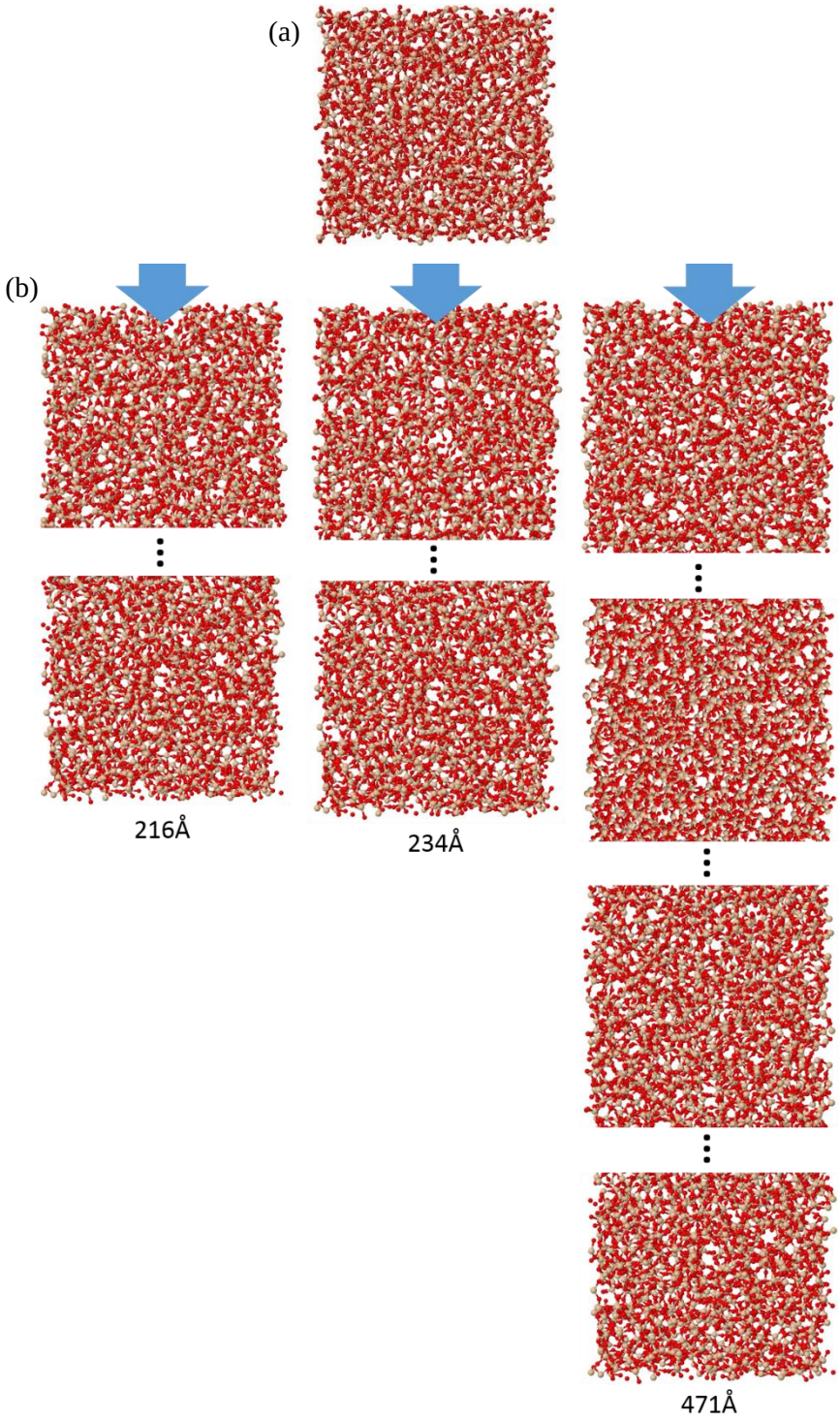


Figure 3.2.4 (a) Amorphous SiO_2 model obtained from Le Roux and Petkov [57]. (b) Output models of various thicknesses.

The resulting diffraction patterns and corresponding azimuthally averaged intensity distribution functions $I(\boldsymbol{q})$ are shown in Figure 3.2.5 while Figure 3.2.6 shows the resulting $I(\boldsymbol{q})$ background fits, $\varphi(\boldsymbol{q})$ and $G(\boldsymbol{r})$ after atomic background subtraction. Measurements of the first three peaks of $G(\boldsymbol{r})$ curves are given in Table 3.2.2.

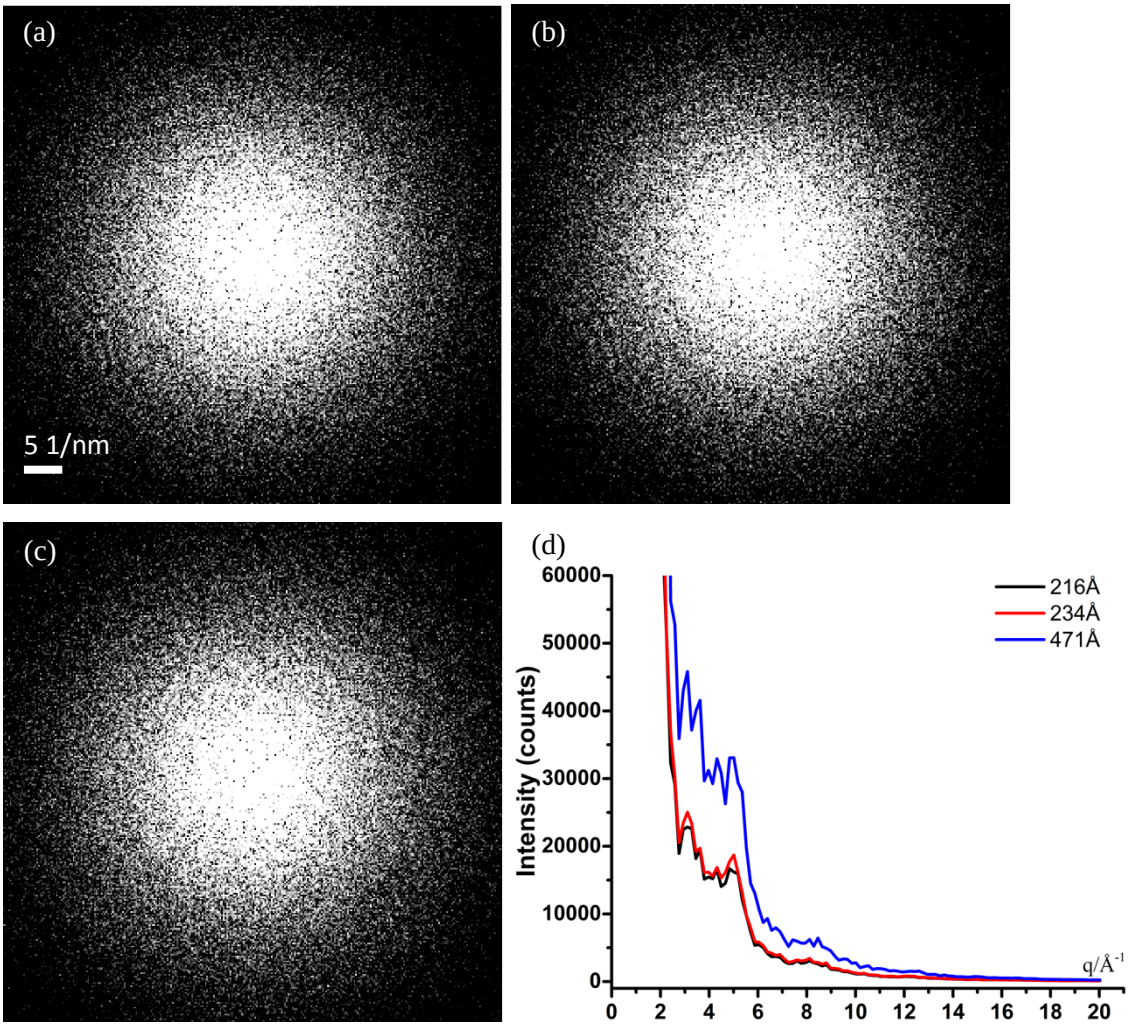


Figure 3.2.5 Simulated diffraction patterns of amorphous SiO_2 films with various thicknesses calculated using multislice simulations. Thicknesses of (a) 216Å, (b) 234Å (c) 471Å and (d) their corresponding azimuthally averaged intensity profiles.

It can be seen from Figures 3.2.5 (a), (b) and (c) that all three diffraction patterns are amorphous without any diffracted spots or rings. Comparing Figures 3.2.5 (d) with 3.2.1 (d), shows that $I(\boldsymbol{q})$ of the 234Å film is marginally more intense than shows significantly higher intensity compared to the others. Moreover, shoulders around $\boldsymbol{q}$ = 3 and 5Å^{-1} are observed which also appear in the experimental data.

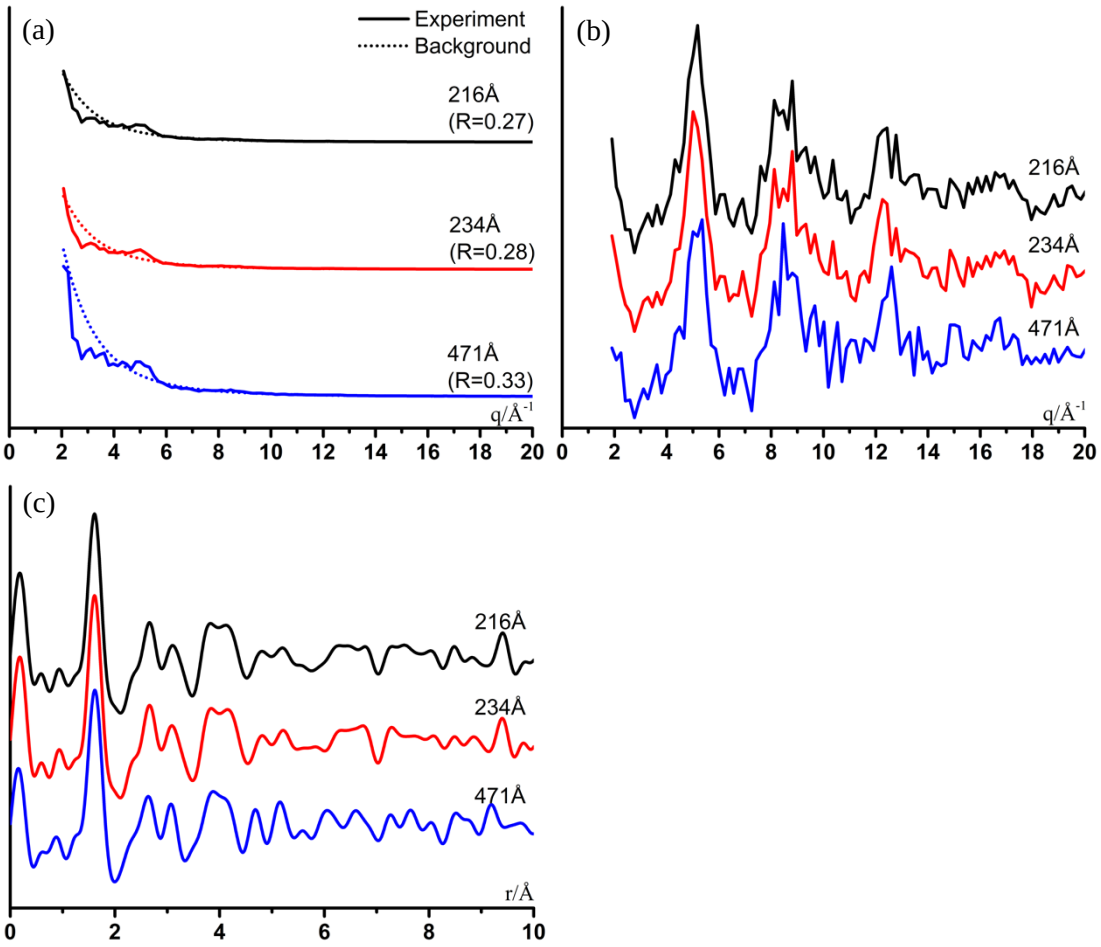


Figure 3.2.6 Effect of sample thickness on the RDF. (a) $I(\boldsymbol{q})$ background fits, (b) $\varphi(\boldsymbol{q})$ and (c) $G(\boldsymbol{r})$ extracted from 216, 234 and 471Å thick models.

Table 3.2.2 Effect of sample thickness on $G(\boldsymbol{r})$ after multislice simulations. Deviations of (a) peak positions and (b) amplitude of the first three peaks.

(a) Peak position	1st	2nd	3rd
216Å	1.61 (0%)	2.66 (0%)	3.10 (0%)
234Å	1.61 (0%)	2.66 (0%)	3.09 (-0.32%)
471Å	1.62 (+0.62%)	2.64 (-0.75%)	3.07 (+0.97%)

Unit: Å (Relative error wrt 216Å)

(b) Peak amplitude	1st	2nd	3rd
216Å	6.112 (0%)	2.612 (0%)	0.831 (0%)
234Å	6.161 (+0.79%)	2.681 (+2.64%)	0.865 (+4.12%)
471Å	5.936 (-10.89%)	2.294 (-12.18%)	1.221 (+46.92%)

Unit: a.u. (Relative error wrt 216Å)

It can be seen from Figure 3.2.6 (a) that the $I(\boldsymbol{q})$ background fits show the same result as the experimental data (Figure 3.2.2 (a)) in that thinner specimens show a better agreement (R = 0.28) compared to the thicker film (R = 0.33). In addition, measurements given in Table 3.2.2 for the 1st and 2nd peaks shows the same trend as the experimental data, with less than a 1% peak position shift and a drop in peak amplitude of more than 10%. However, possibly due to limited sampling (a simulated area of 1200Å^2 as compared to 7,000,000Å^2 in practice) and residual periodicity formed during model extension, the 3rd peaks, which represent distances up to third neighbours, do not show the same trend as expected as the experimental data.

Finally, RMC refinements were performed using the RDF results from each specimen and the resulting models with extracted $G(\boldsymbol{r})$ are shown in Figure 3.2.7.

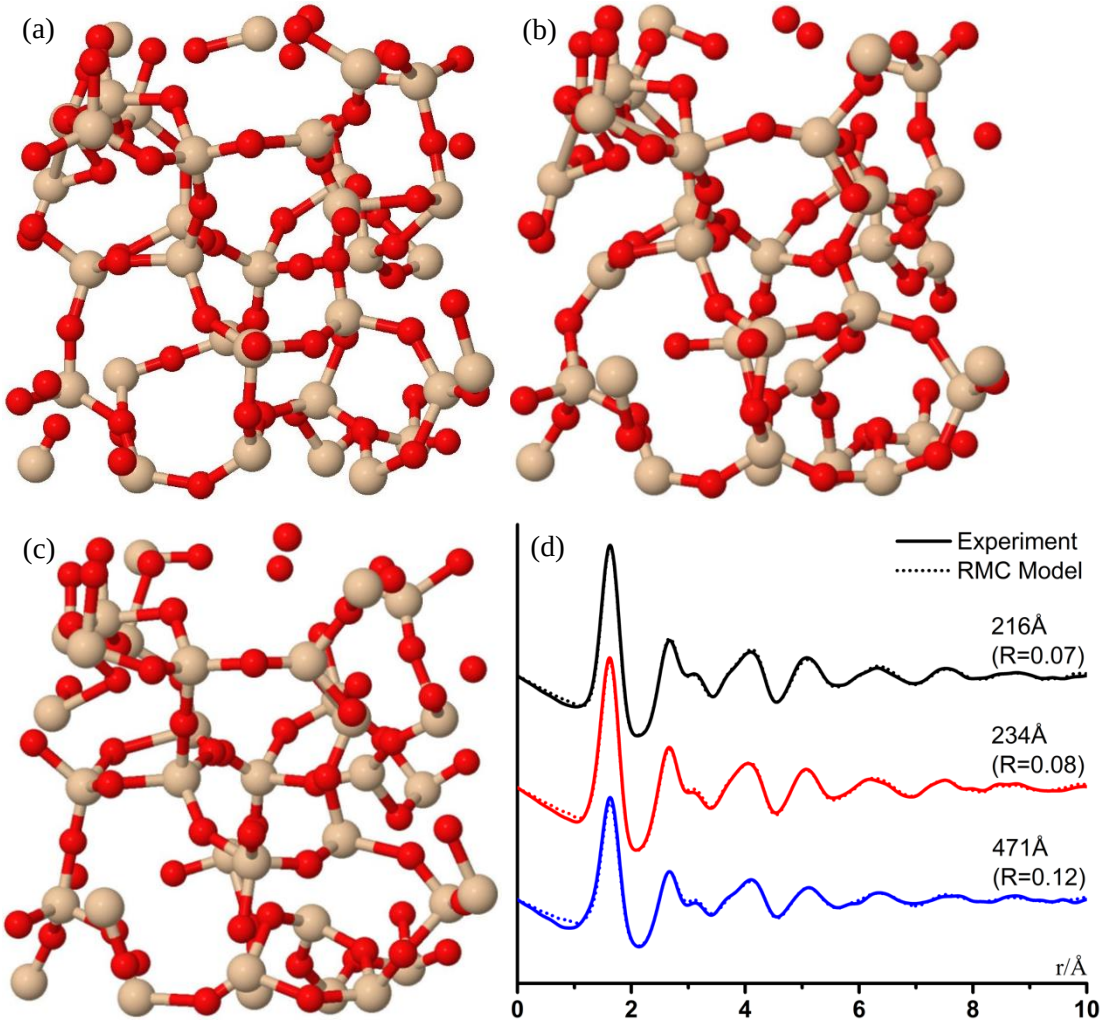


Figure 3.2.7 RMC refined models of varied thicknesses of (a) 216, (b) 234 and (c) 471Å together with their corresponding (d) $G(\boldsymbol{r})$.

Owing to the applied constraints as described in Section 3.1.3, the silica tetrahedral structure is preserved after the refinements as shown in Figures 3.2.7 (a), (b) and (c). The corresponding $G(\boldsymbol{r})$ curves (Figure 3.2.7 (d)) show a goodness-of-fit index *R* of 0.07, 0.08 and 0.12 for 216, 234 and 471Å films, respectively, indicating a good agreement between the models and the experimental data. Detailed information about the bond angles and bond types for those two models are given in Figure 3.2.8.

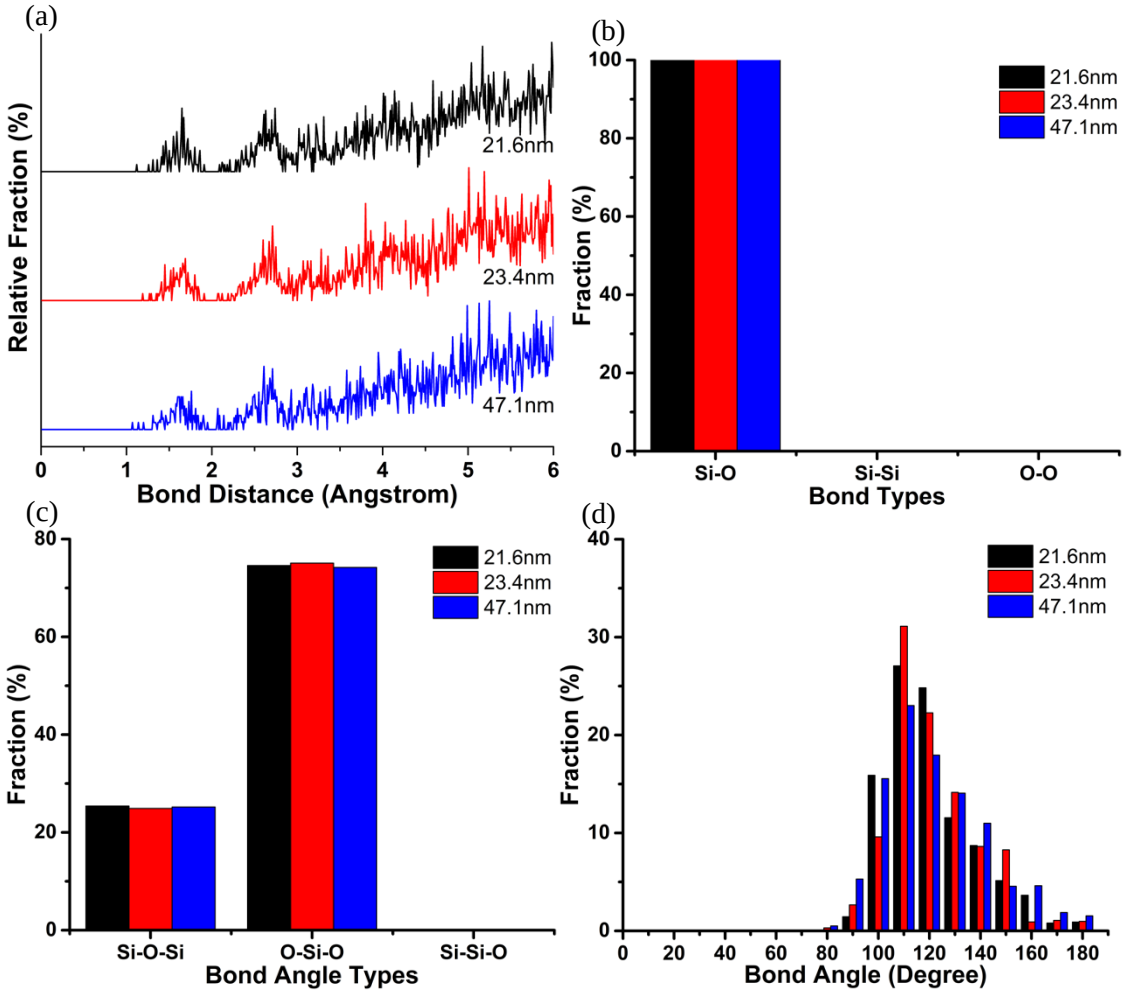


Figure 3.2.8 Comparison of models with varied thicknesses. (a) Bond distance distributions, (b) Bond types, (c) Bond angle types and (d) Bond angle distributions.

The bond distance distributions as shown in Figure 3.2.8 (a) show a similar trend for all three models with Si-O bonds around 1.6Å, O…O distances around 2.6Å and Si…Si distances around 3.1Å. Figure 3.2.8 (b) shows the bond type distributions for all three models and the results show that only Si-O bonds are present whereas the distances of Si…Si and O…O were close enough to be considered as bonded distances based on their covalent radii. Since there are no Si-Si bonds present, the contribution of the Si-Si-O bond

angle is 0% for all three models with a similar ratio of 1:3 for Si-O-Si to O-Si-O angles as shown in Figure 3.2.8 (c). Figure 3.2.8 (d) shows the bond angle distributions. All three models have around 75% of the bond angles between 80-130^{o} which mainly correspond to the inner-tetrahedral O-Si-O angle, comparable to Figure 3.2.8 (c). The remaining 25% of bond angles over 130^{o} correspond to the outer-tetrahedral Si-O-Si angles (See Figure 3.1.7).

Finally, the average coordination numbers were computed for all three models. The results show that Z_{Si} for models of 216, 234 and 471Å are 3.57, 3.54 and 3.36 while Z_O are 1.78, 1.77 and 1.68, respectively. As described in the previous section, Z_{Si} and Z_O for the DFT model are 3.86 and 1.85. This suggest that errors of 8% and 4% in Z_{Si} and Z_O are introduced when the film thickness is around 200Å. Moreover, for thickness of up to 500Å, errors of 13% and 9% for Z_{Si} and Z_O are expected.

3.3 Effect of Noise on the RDF

Before moving onto the effect of coherence and dose, I first look at the influence of noise on the RDF. As mentioned in Section 2.4.2.5, a damping factor is needed to suppress oscillations in $\varphi(\boldsymbol{q})$ at high $\boldsymbol{q}$ caused by noise. Therefore, a direct electron counting detector (Medipix3) was used for comparison with a conventional integrating CMOS detector (OneView) to assess the influence of noise. Note that a hardware binning was applied to the OneView detector in order match the pixel size of the Medipix3 for comparison. General details of both detectors are listed in Table 3.3.1.

Table 3.3.1 General specifications of Medipix3 and OneView detectors.

	Medipix3	OneView
Type	Counting	Integrating
Pixel numbers	256 x 256	1024 x 1024 (bin by 4)
Pixel size	55μm	60μm (binned by 4)
Active size	14.1mm	61.4mm
Dynamic range	24 bit	16bit
Features	Readout Noise-free	High Signal-to-Noise ratio
	1200 Frames-per-second	200 Frames-per-second

First, the calibration factor $\delta\boldsymbol{q}$ described in Section 2.4.2.1 was obtained using both detectors and Figures 3.3.1 (a) and (c) show the diffraction patterns of polycrystalline gold captured by both Medipix3 and OneView detectors, together with the azimuthally averaged intensity distribution functions $I(\boldsymbol{q})$ in Figure 3.3.1 (b) and (d).

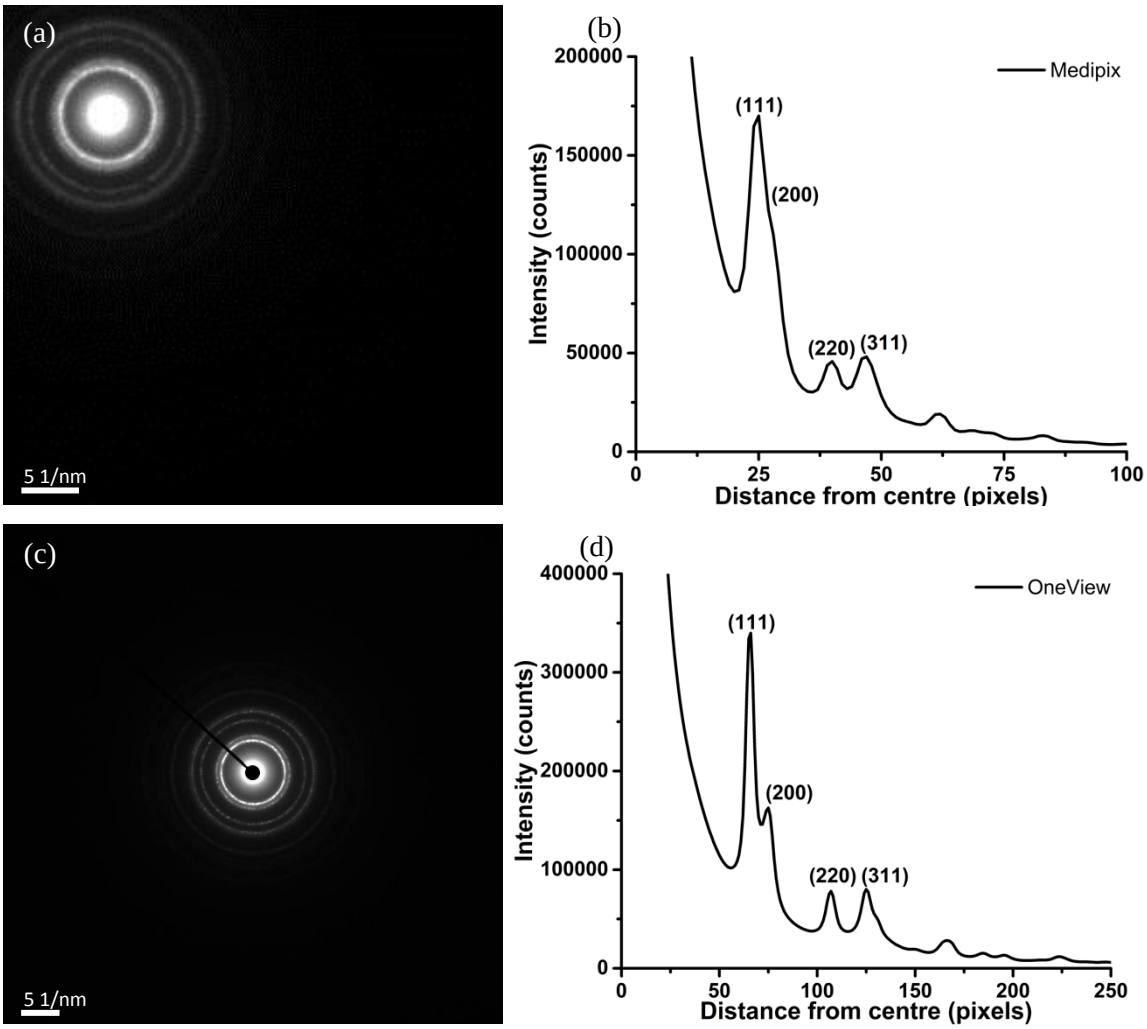


Figure 3.3.1 Diffraction patterns of polycrystalline gold specimen recorded by (a) Medipix3 and (c) OneView detectors. (b) and (d) shows their corresponding azimuthally averaged intensity distribution functions.

Figures 3.3.1 (a) and (c) show clearly defined diffracted rings captured on both detectors. Their $I(\boldsymbol{q})$ in Figures 3.3.1 (b) and (d) show clearly resolved (111), (220) and (311) reflections. However, the (200) reflection is not resolved on the Medipix3 sensor due to a limited pixel number (256 x 256).

With the $I(\boldsymbol{q})$ measured, the calibration factors $\delta\boldsymbol{q}$ calculated from these patterns are shown in Table 3.3.2. The results show that $\delta\boldsymbol{q}$ of the Medipix3 and OneView detectors are 0.108613 ± 0.001376 (1.27%) and 0.04078 ± 0.000275 (0.67%), respectively.

Table 3.3.2 Calibration factors calculated from polycrystalline gold with (a) Medipix3 and (b) OneView detectors.

(a) i	Pixel numbers n_i (pixel)	lattice spacings d_i (Å)	$\delta\boldsymbol{q}_i = \frac{2\pi}{n_i \cdot d_i}$	
1	25	2.354	0.106741	
2	28	2.039	0.110048	Average $\delta\boldsymbol{q}$ = 0.108613 ± 0.001376 (±1.27%)
3	40	1.442	0.108942	
4	47	1.230	0.108720	

(b) i	Pixel numbers n_i (pixel)	lattice spacings d_i (Å)	$\delta\boldsymbol{q}_i = \frac{2\pi}{n_i \cdot d_i}$	
1	66	2.354	0.040432	
2	75	2.039	0.041085	Average $\delta\boldsymbol{q}$ = 0.040780 ± 0.000275 (±0.67%)
3	107	1.442	0.040726	
4	125	1.230	0.040879	

After $\delta\boldsymbol{q}$ were acquired from both detectors, diffraction patterns from amorphous SiO_2 were captured on both detectors as shown in Figure 3.3.2 while Figure 3.3.3 shows the resulting $\varphi(\boldsymbol{q})$ and $G(\boldsymbol{r})$.

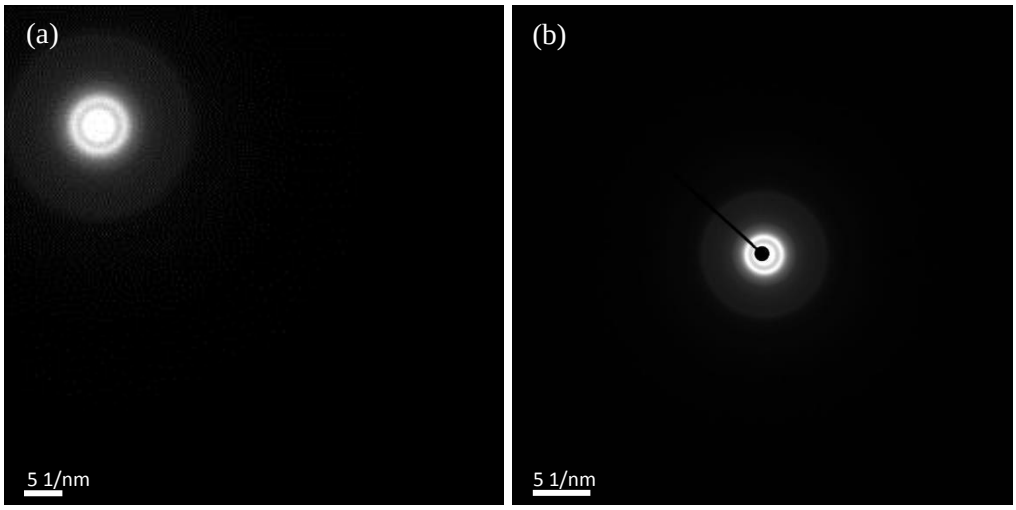


Figure 3.3.2 Diffraction patterns recorded from 216Å amorphous SiO_2 captured by (a) Medipix3 and (c) OneView detectors.

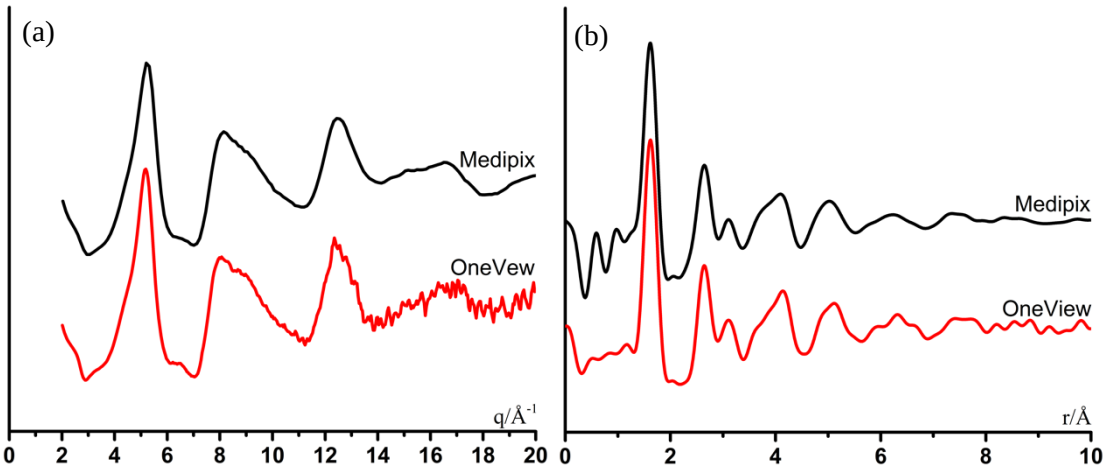


Figure 3.3.3 Effect of noise on the RDF. (a) $\varphi(\boldsymbol{q})$ and (b) $G(\boldsymbol{r})$ extracted from diffraction patterns captured by Medipix3 and OneView detectors.

Due to the limited active size of 14.1mm, the diffraction pattern was placed at the top left corner of the Medipix3 sensor to enable the recording of high $\boldsymbol{q}$ range data up to 20Å^{-1} as shown in Figure 3.3.2 (a). In contrast, the OneView detector show in Figure 3.3.2 (b) has

larger active size of 61.4mm which allows diffraction pattern to be captured at a central position. It can be seen from Figure 3.3.3 (a) that the overall shape of $\varphi(\boldsymbol{q})$ is the same for both detectors. However, a considerable oscillation is observed at $\boldsymbol{q}$ range over 13Å^{-1} in the data recorded by OneView camera. The oscillations in the $\varphi(\boldsymbol{q})$ lead to ripples in the $G(\boldsymbol{r})$ as shown in Figure 3.3.3 (b). Measurements of the corresponding RDFs are shown in Table 3.3.3.

Table 3.3.3 Effect of noise on $G(\boldsymbol{r})$. Deviations of (a) peak positions and (b) amplitude of the first three peaks.

(a) Peak position	1st	2nd	3rd
Medipix3	1.62 (0%)	2.65 (0%)	3.10 (0%)
OneView	1.62 (0%)	2.64 (-0.38%)	3.10 (0%)

Unit: Å (Relative error wrt Medipix3)

(b) Peak amplitude	1st	2nd	3rd
Medipix3	3.747 (0%)	1.567 (0%)	0.366 (0%)
OneView	4.025 (+7.42%)	1.773 (+13.17%)	0.396 (+8.06%)

Unit: a.u. (Relative error wrt Medipix3)

It can be seen from Table 3.3.3 that the peak positions in both $G(\boldsymbol{r})$ curves are identical except for a 0.01Å difference at the 2nd peak. However, the peak amplitudes indicate that peaks recorded on the OneView camera are more than 7% larger compared to the Medipix3 data. Thus, Medipix3 was used in the rest of the experiments to test the effect of coherence and dose on the RDF analysis.

3.4 Effect of Coherence on the RDF

Since the formation of a diffraction pattern relies on the interference of waves, changes in illumination coherence will lead to changes in the recorded intensities in diffraction patterns. Therefore, the effect of coherence has been explored in this section by analysing diffraction patterns recorded using various degrees of coherence.

In general, the coherence of an electron beam defines how well the electron waves are "in step" with one another and is used to indicate the degree of interference of electrons [19]. Temporal coherence measures how similar the wave packets at any pair of times. A definition of the temporal coherence, also known as longitudinal coherence length, is given as $L_T = v\mathrm{h}/\Delta E$ where v is the electron velocity, h is Planck's constant and ΔE is the energy spread of the beam. To ensure high temporal coherence, a source size low intrinsic energy width, a stable high voltage supply and stable lens supplies is required to give a small energy width $\triangle E$. Spatial coherence describes the degree of correlation between different points on the same wave front at the same time. Perfect spatial coherence would imply that the electrons all arise from the same point at the source. Hence source size governs spatial coherence and smaller sources give a better degree of coherence. The spatial coherence length, or transverse coherence length, is defined as $L_s = \lambda/2\theta$ [19] where λ is the electron wavelength and θ is the semi-angle of the incident beam. To achieve good spatial coherence, small values of θ can be achieved using smaller condenser apertures while decreasing, λ by increasing the accelerating voltage. Figure

3.4.1 shows a schematic diagram illustrating the difference in temporal and spatial coherence.

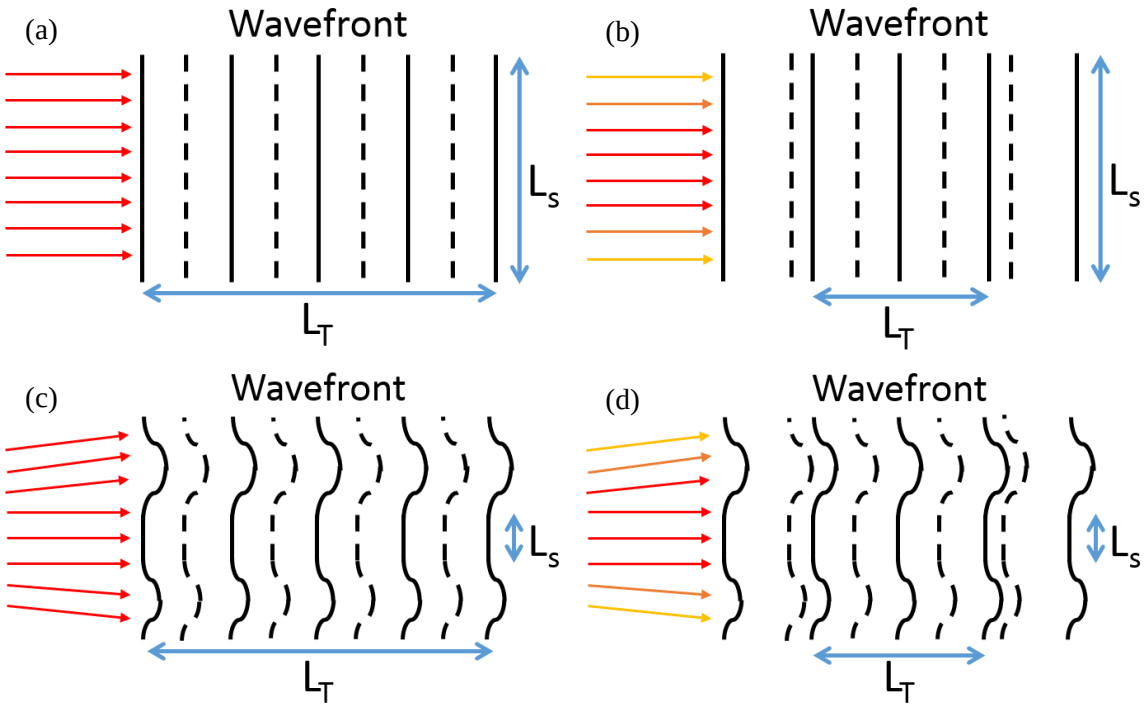


Figure 3.4.1 Schematic diagram of coherence. (a)Full spatial and temporal coherence, (b) Spatial coherence but temporal incoherence, (c) Spatial incoherence but temporal coherence, and (d) Spatial and temporal incoherence.

With no energy spread ($\Delta E = 0$), all wavefronts are flat, and a perfectly coherent beam is shown as Figure 3.4.1 (a). If energy spread is non-zero as indicated in different colours, limited temporal coherence is present as Figure 3.4.1 (b). In contrast, if the wavefronts are not flat, this leads to partial spatial coherence (Figure 3.4.1 (c)). Finally, when an energy spread is present and wavefronts are not flat, spatial and temporal incoherence are present as shown in Figure 3.4.1 (d).

In this study, a cold field emission W emitter with an energy spread of ~0.3eV was used operating at 200keV. Following $L_T = v\mathrm{h}/\Delta E$, where $v = 2.085 \cdot 10^8 \mathrm{m/s}$ and $\mathrm{h} = 6.626 \cdot 10^{-34} \mathrm{m^2 kg/s}$, it provides a high temporal coherence of ~3μm which exceeds the typical sizes of objects studied in this thesis. The spatial coherence can adjusted by altering the strength of the electrostatic gun lens (A2) as shown in the schematic ray diagram in Figure 3.4.2 below.

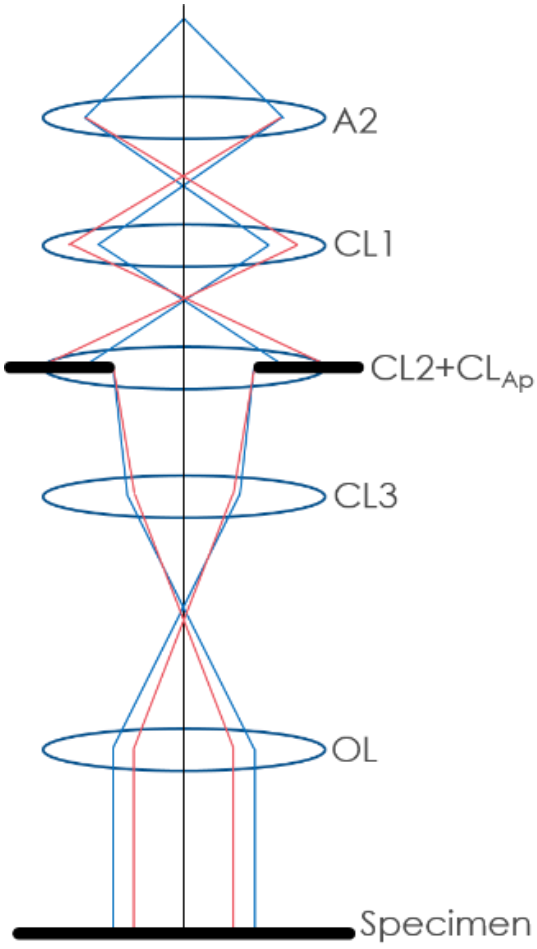


Figure 3.4.2 Schematic ray diagram of the Grand-ARM upper optical column. (Blue) Default setting. (Red) High Coherence setting.

It can be seen from Figure 3.4.2 that by moving the cross-over point closer to the A2 lens, as indicated by the red line, the virtual source size is demagnified and the wave passing through the second condenser lens and aperture ($CL2+CL_{Ap}$) is hence more coherent. However, adjusting the A2 lens current, will also affect the flux passing through the aperture, which will affect the current in the probe. Therefore, the current for each experimental condition was measured using a faraday cage and for each degree of coherence the total number of electrons was kept constant.

In this experiment, four different A2 lens currents of 3.30, 3.39, 3.45 and 3.50eV were set to achieve four degrees of coherence. The resulting probe images and their corresponding intensities of Fresnel fringes averaging over 10 pixels are shown in Figure 3.4.3.

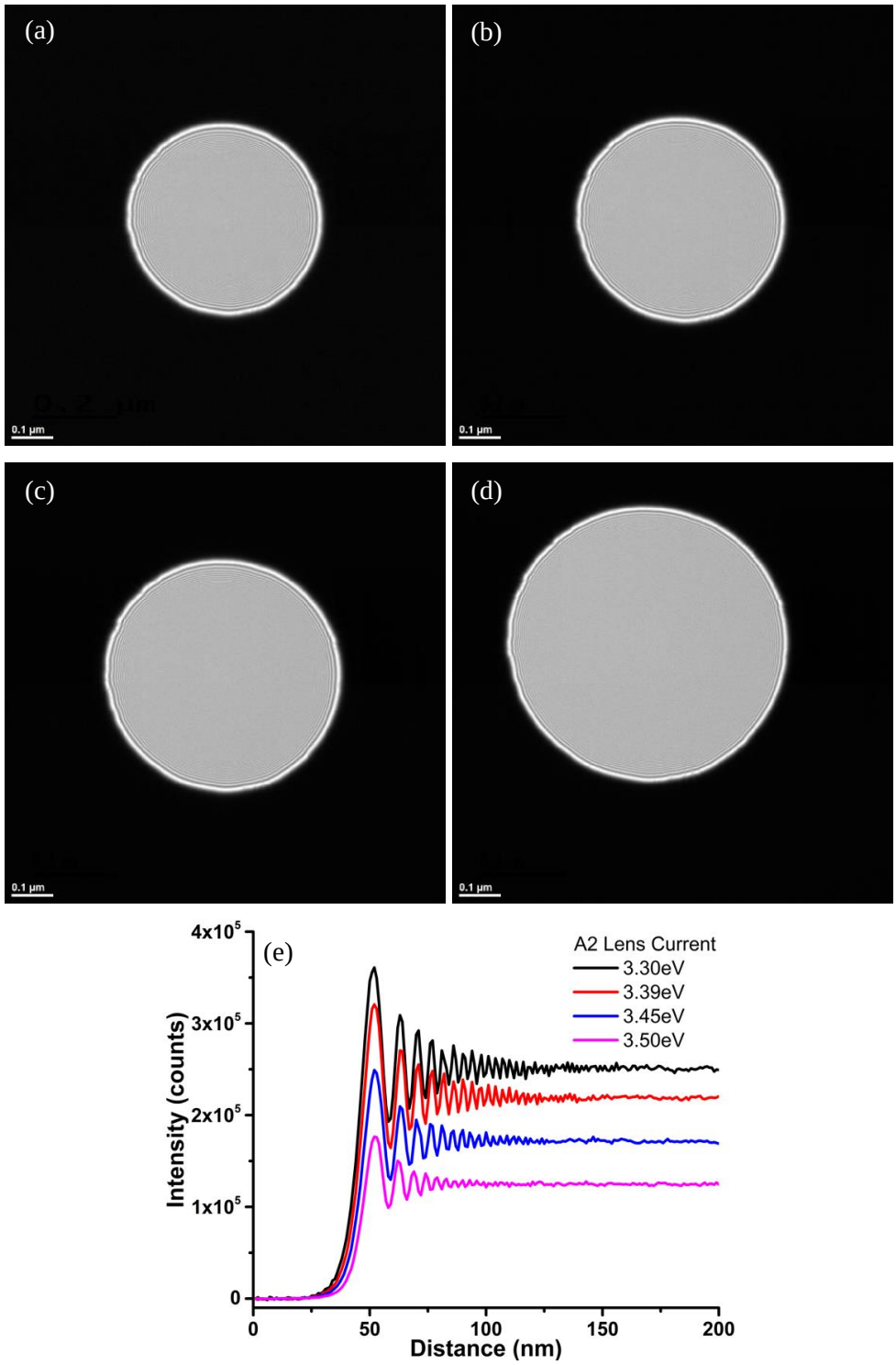


Figure 3.4.3 Probe images for various degrees of coherence. A2 lens currents of (a) 3.30eV, (b) 3.39eV, (c) 3.45eV, (d) 3.50eV and (e) their corresponding intensity profiles of Fresnel fringes averaging over 10 pixels.

Comparing Figures 3.4.3 (a-d), it can be seen that the probe sizes change when altering the A2 lens (Figure 3.4.2). In addition, direct evidence of changes in the degree of coherence can be seen from the intensities of Fresnel fringes as shown in Figure 3.4.3 (e). It is clear that the contrast of the Fresnel fringes is higher at an A2 value of 3.30eV as compared to 3.50eV, suggesting better spatial coherence.

However, to determine the spatial coherence length using $L_s = \lambda/2\theta$, diffraction patterns of polycrystalline gold were acquired to define the semi-angle θ and Figure 3.4.4 shows the recorded diffraction patterns and their corresponding intensity profiles.

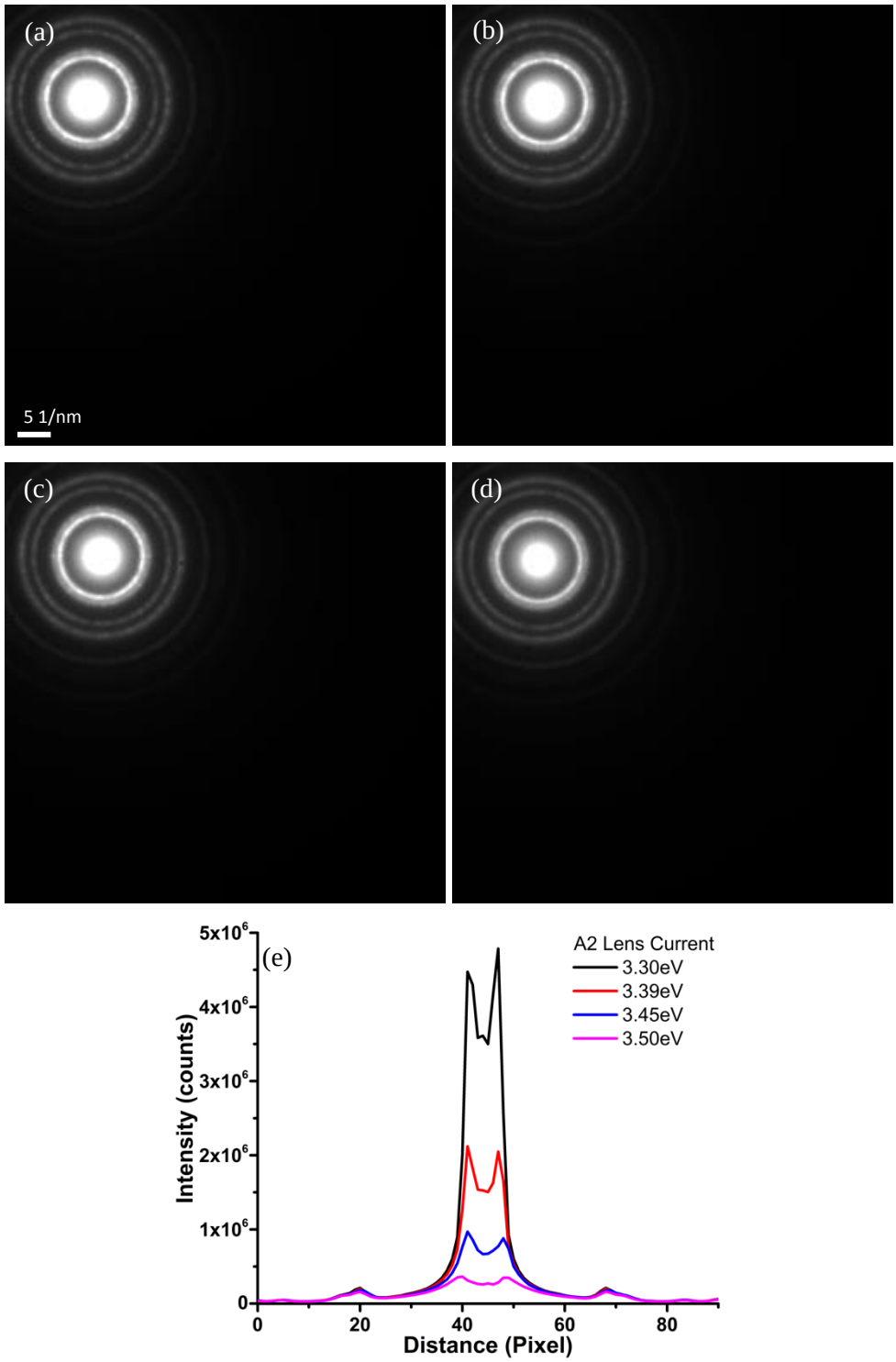


Figure 3.4.4 Polycrystalline gold diffraction patterns for various degrees of coherence. A2 lens currents of (a) 3.30eV, (b) 3.39eV, (c) 3.45eV, (d) 3.50eV and (e) their corresponding azimuthal averaged intensities.

It can be seen from Figure 3.4.4 (e) that all central beams were saturated and to measure the semi-angle θ the FWHM of the central beam is required. Therefore, the saturated intensities were cropped and a Gaussian function was applied to fit the central beam. Once the FWHM is known, θ can be computed as $\theta = \beta(a/b)$, where β is the angle corresponding to a diffraction ring while a and b are the size of the central beam and the diffracted ring. In this case of polycrystalline gold, β is 10.66mrad and b is 48pixel corresponding to the first diffraction maxima for gold while a is the FWHM computed from each central beam. All resulting data, for a, θ and L_s at each condition are given in Table 3.4.1.

Table 3.4.1 Spatial coherence length calculation under various A2 lens currents

A2 Lens Current	a (pixel)	θ (mrad)	L_s (Å)
3.30eV	4.96	0.55	22.8
3.39eV	6.28	0.70	18.0
3.45eV	8.35	0.93	13.5
3.50eV	12.0	1.33	9.4

(λ = 2.51pm at 200kV)

Table 3.4.1 shows the spatial coherence lengths for all degrees of coherence. The results indicate that the coherence length decreases with an increase in the A2 lens current, which is the same trend as measured previously using Fresnel fringes in Figure 3.4.3 (e).

Once the spatial coherence lengths were determined, diffraction patterns of amorphous SiO_2 for each degree of coherence were captured along with their azimuthally averaged $I(\boldsymbol{q})$ as shown in Figure 3.4.5. Figure 3.4.6 shows the resulting $I(\boldsymbol{q})$ background fits, $\varphi(\boldsymbol{q})$ and $G(\boldsymbol{r})$. Measurements of the peak parameters of $G(\boldsymbol{r})$ are given in Table 3.4.2.

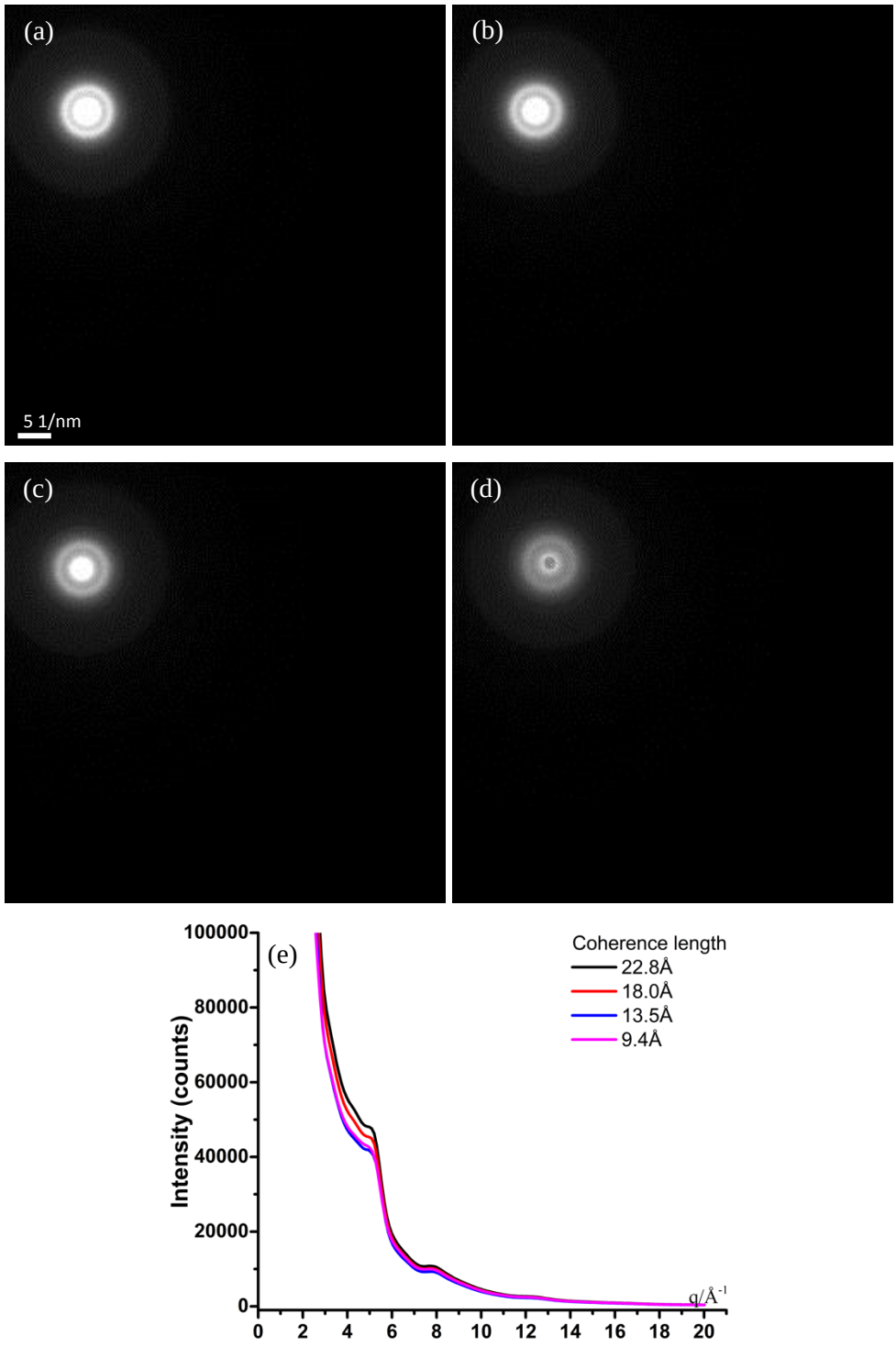


Figure 3.4.5 Diffraction patterns of 216Å amorphous SiO_2 with various coherence lengths (a) 22.8Å (b) 18.0Å, (c) 13.5Å, (d) 9.4Å and (e) their azimuthally averaged intensity distribution functions.

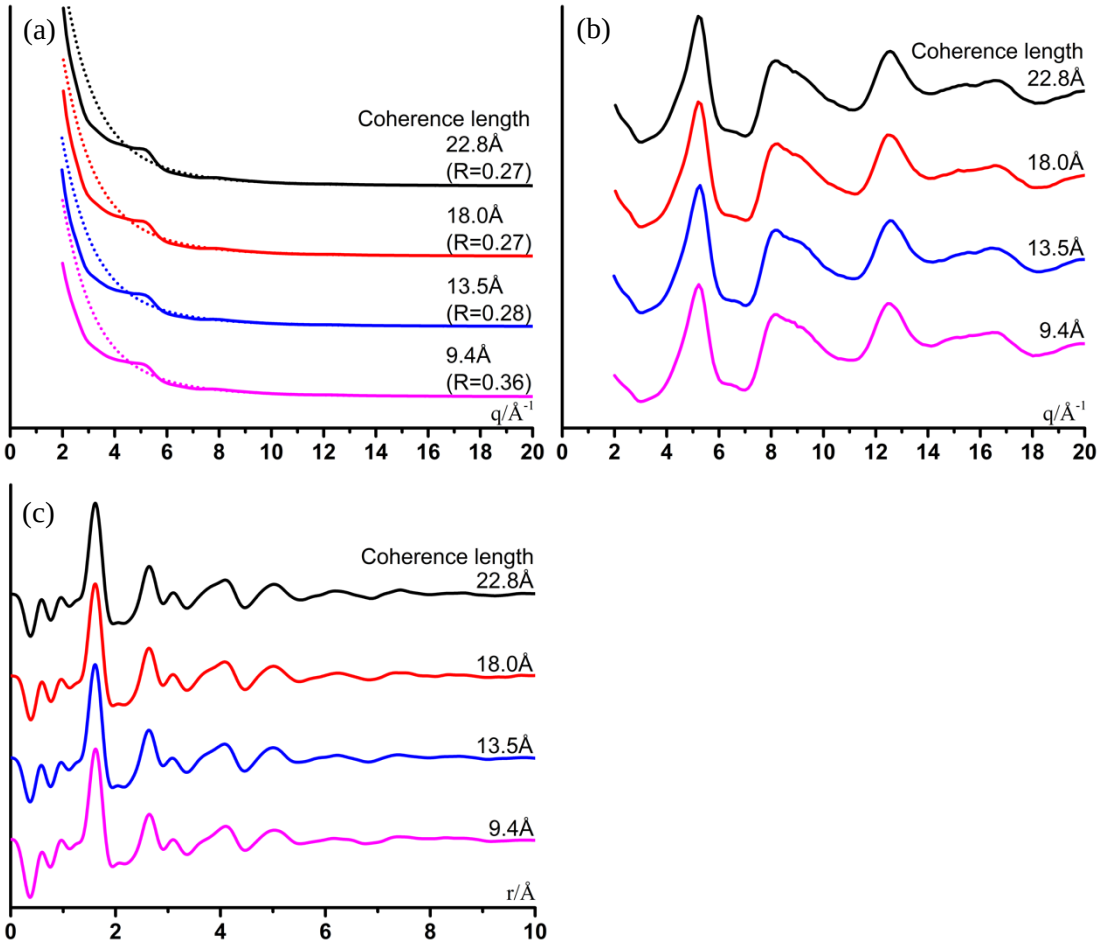


Figure 3.4.6 Effect of coherence on the RDF. (a) $I(\boldsymbol{q})$ background fittings, (b) $\varphi(\boldsymbol{q})$ and (c) $G(\boldsymbol{r})$ extracted from diffraction patterns recorded with various coherence lengths.

It can be seen from Figure 3.4.6 (a) that the $I(\boldsymbol{q})$ background fits to coherence lengths of 22.8, 18.0 and 13.5Å are nearly identical with R around 0.27, while a coherence length of 9.4Å gives a poorer fit, with R = 0.36.

Table 3.4.2 Effect of coherence on $G(\boldsymbol{r})$. Deviations of (a) peak positions and (b) amplitude of the first three peaks.

(a) Peak position	1st	2nd	3rd
22.8Å	1.61 (0%)	2.64 (0%)	3.10 (0%)
18.0Å	1.61 (0%)	2.64 (0%)	3.09 (-0.32%)
13.5Å	1.61 (0%)	2.64 (0%)	3.08 (-0.64%)
9.4Å	1.62 (+0.62%)	2.64 (0%)	3.10 (0%)

Unit: Å (Relative error wrt 22.8Å)

(b) Peak amplitude	1st	2nd	3rd
22.8Å	3.780 (0%)	1.532 (0%)	0.399 (0%)
18.0Å	3.812 (+0.86%)	1.542 (+0.67%)	0.395 (-1.08%)
13.5Å	3.860 (+2.14%)	1.544 (+0.83%)	0.277 (-30.63%)
9.4Å	3.661 (-3.14%)	1.473 (-3.82%)	0.353 (-11.64%)

Unit: a.u. (Relative error wrt 22.8Å)

It can be seen from Table 3.4.1 that the peaks deviate by only 0.02Å in position while the peak amplitudes fluctuate by less than 4% for the 1st and 2nd peaks. Based on the experimental results above, I have demonstrated that the RDF analysis is insensitive to spatial coherence.

3.5 Effect of Dose on the RDF

Radiation damage is a significant problem in electron microscopy and multiple mechanisms have be proposed in previous studies [59, 60]. In general, two main damage mechanisms, namely knock-on damage and radiolysis, are observed. This may result in changes of atomic structure or even destroy the entire specimen. Therefore, in this section the influence of dose on the RDF will be studied.

To define the radiation damage in electron microscopy, a commonly accepted unit, the electron dose, is defined as the number of electrons per square angstrom ($e^-/Å^2$). In practice, the electron beam current is measured using a faraday cage and the dose rate is calculated taking into account the size of the electron probe which is measured from a probe image (see Figure 3.4.3 (b)). Table 3.5.1 shows the details of the current to dose rate conversion.

Table 3.5.1 Current-to-dose rate conversion

Probe radius (Measured from probe image)	$2.50 \cdot 10^3$ Å
Probe area ($\pi \cdot r^2$)	$1.9635 \cdot 10^7$ $Å^2$
Current (Measured from Faraday cage)	62 pA
(1pA = $6.25 \cdot 10^6$ e^-/s)	$3.88 \cdot 10^8$ e^-/s
Dose rate	19.74 $e^-/Å^2 \cdot s$

From Table 3.5.1, a constant dose rate of 19.74$e^-/Å^2 \cdot s$ is obtained. This can be converted into a dose as 10.76, 21.51, 32.27, 43.02 and 53.78$e^-/Å^2$ for corresponding exposure times of 0.55, 1.10, 1.65, 2.20 and 2.75s. Figure 3.5.1 shows the diffraction patterns and azimuthally averaged intensity distribution functions $I(\boldsymbol{q})$, while Figure 3.5.2 shows the resulting $\varphi(\boldsymbol{q})$ and $G(\boldsymbol{r})$. Measurements of the peaks in the RDFs are shown in Table 3.5.2.

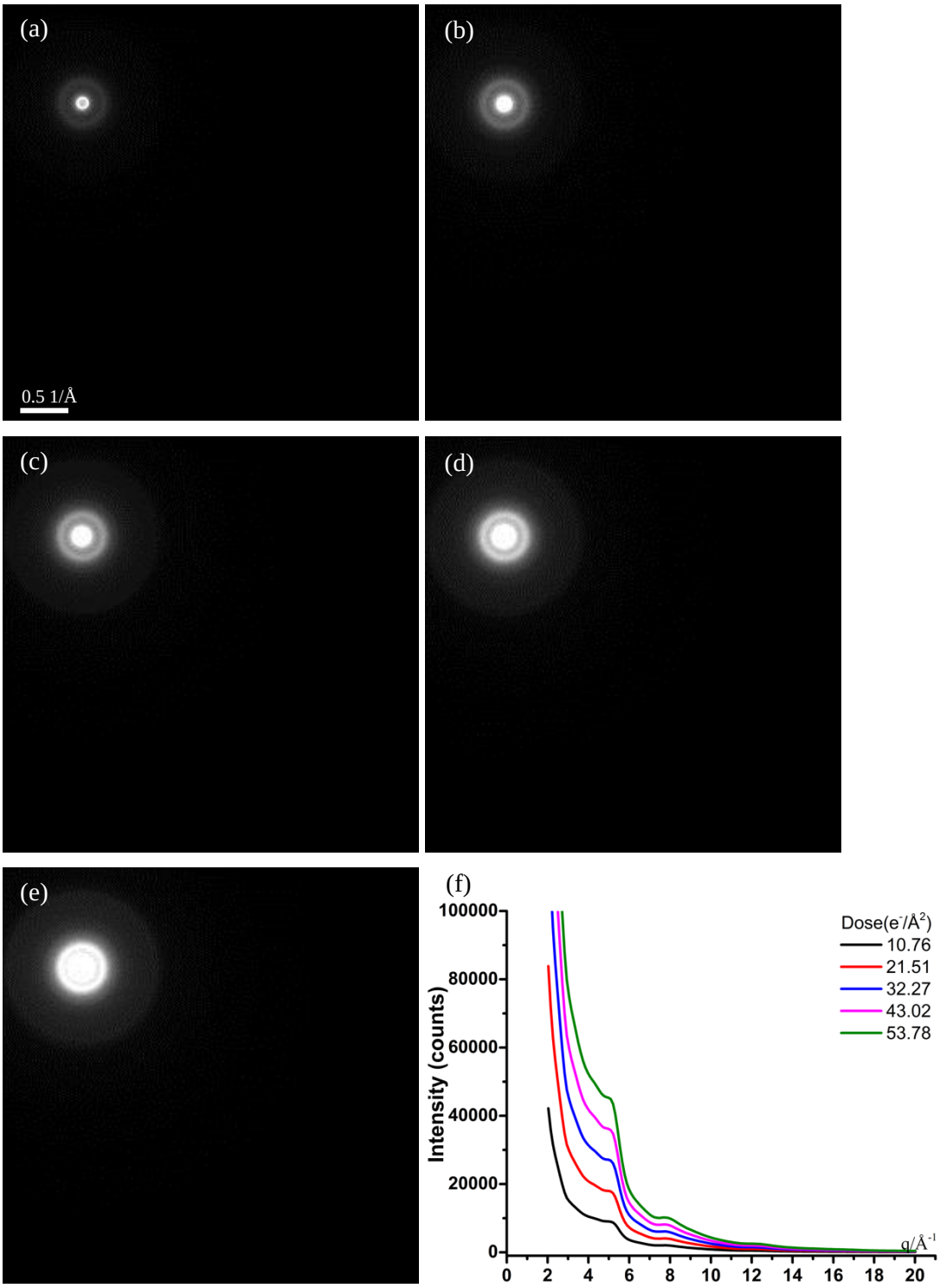


Figure 3.5.1 Diffraction patterns recorded from a 216Å amorphous SiO_2 with various doses ($e^-/Å^2$) (a) 10.76, (b) 21.51, (c) 32.27 (d) 43.02, (e) 53.78 and (f) their azimuthally averaged intensity distribution functions.

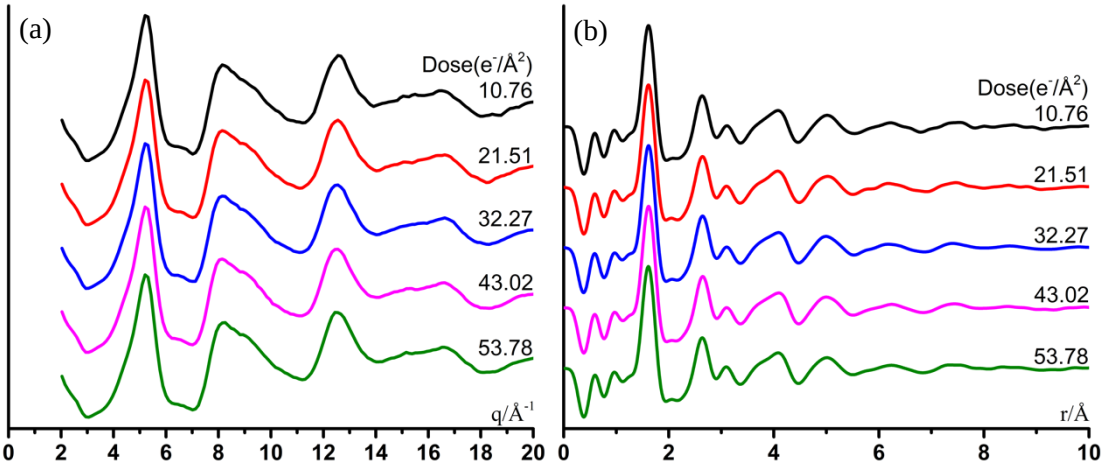


Figure 3.5.2 Effect of dose on the RDF. (a) $\varphi(\boldsymbol{q})$ and (b) $G(\boldsymbol{r})$ extracted from experiments with different dose.

It can be seen from Table 3.5.2 that the peak position alters by only 0.01Å with changing dose, while the peak amplitude has less than 2% deviation for the first two peaks. Even with only 10.76 $e^-/Å^2$ dose, the RDF curve does not differ from ones obtained with higher doses. Although amorphous SiO_2 appears not to be radiation sensitive, a dose of 10.76 $e^-/Å^2$ can be considered as a low-dose condition for most radiation sensitive materials. For example, Chen et al. [61] used a dose of 26 $e^-/Å^2$ for a single image for ZSM-5 zeolites. This suggests that the RDF analysis is suitable for studies of radiation sensitive materials.

Table 3.5.2 Effect of dose on $G(\boldsymbol{r})$. Deviations of (a) peak positions and (b) amplitude of the first three peaks.

(a) Peak position	1st	2nd	3rd
10.76 $e^-/Å^2$	1.61 (0%)	2.64 (0%)	3.11 (0%)
21.51 $e^-/Å^2$	1.61 (0%)	2.64 (0%)	3.10 (-0.32%)
32.27 $e^-/Å^2$	1.62 (+0.62%)	2.64 (0%)	3.10 (-0.32%)
43.02 $e^-/Å^2$	1.62 (+0.62%)	2.65 (+0.38%)	3.10 (-0.32%)
53.78 $e^-/Å^2$	1.61 (0%)	2.64 (0%)	3.09 (-0.64%)

Unit: Å (Relative error wrt 10.76$e^-/Å^2$)

(b) Peak amplitude	1st	2nd	3rd
10.76 $e^-/Å^2$	3.815 (0%)	1.566 (0%)	0.393 (0%)
21.51 $e^-/Å^2$	3.827 (+0.32%)	1.545 (-1.31%)	0.389 (-0.97%)
32.27 $e^-/Å^2$	3.780 (-0.92%)	1.566 (0%)	0.374 (-4.64%)
43.02 $e^-/Å^2$	3.782 (-0.86%)	1.568 (+0.13%)	0.359 (-8.67%)
53.78 $e^-/Å^2$	3.812 (-0.07%)	1.542 (-1.51%)	0.395 (+0.56%)

Unit: a.u. (Relative error wrt 10.76$e^-/Å^2$)

3.6 Robustness of RDF Analysis

In this chapter, detailed experimental and simulations were described in Section 3.1 and four experimental factors which have the potential to affect the RDF curves have been examined. These included the sample thickness, noise, coherence and dose.

In Section 3.2, experiments carried out for samples of various thicknesses indicate that multiple scattering has nearly no impact on the position of the peak but influences the amplitude strongly. Combining DFT simulations and RMC refinements, the structural information related to bond types and angles are similar for all refined models but the coordination numbers are decreased by 8% and 13% for films of ~200Å and ~500Å, respectively.

Section 3.3 demonstrated the effects of noise on the RDF. Comparing a conventional integrating detector (OneView) to a direct electron counting detector (Medipix3), noise contributions at high $\boldsymbol{q}$ range can be removed which eliminates errors of up to 13% from $G(\boldsymbol{r})$ curves.

Experiments to study the influence of spatial coherence were carried out by altering the current of the electrostatic gun lens in Section 3.4. The results show that the RDF analysis is also insensitive to spatial coherence. With variations in coherence length of up to 13Å, the $G(\boldsymbol{r})$ curves show errors of less than 0.02Å and 4% for 1st and 2nd peak position and amplitudes, respectively.

Finally, Section 3.5 demonstrated the effect of electron dose on the RDF. The results from different doses indicate that RDF analysis is still robust even at a dose of $11e^{-}/Å^{2}$ and gives accurate $G(\boldsymbol{r})$ with less than 2% deviation. This makes the RDF technique suitable for studies of radiation sensitive materials.

Overall, the robustness of RDF analysis against noise, partial coherence and low dose condition has been demonstrated. The application of this method to studies in materials science will be presented in the next chapter.

Chapter 4 Structural Analysis of Amorphous Materials

In previous chapters, the theory underlying RDF analysis has been discussed. The effects of various factors on both calculations and experiments have been tested. The results demonstrate the robustness of RDF analysis under various conditions. In this chapter, the application of RDF analysis to two different amorphous materials, bioactive glass and metallic glass is discussed.

4.1 Bioactive Glasses

4.1.1 Introduction

The development of biomaterials started in the 1960s. The first generation of biomaterials were bio-inert materials such as ceramics (alumina and zirconia), metals (titanium) or alloys (stainless steel) [62, 63]. Due to their weak interactions with living tissues, an implanted bio-inert material was found to be encapsulated within a non-adherent, fibrous layer of bio-tissue. This results in increased relative movement at the implant-tissue interface leading to loosening and deterioration of the mechanical fit which causes pain. Tissue breakdown is a common mode of clinical failure of implants made from bio-inert materials [64].

To solve the above problem, resorbable materials, such as calcium phosphates, were developed. This type of biomaterial was designed to be dissolved and replaced by the surrounding tissues and to be replaced by the natural host tissues [65, 66]. This concept appears to be ideal, however, in reality, it is complicated by the need to match the rates of implant dissolution and tissue growth. In addition, while the implant is dissolving, its

strength gradually decreases which results in an unstable tissue-implant interface. During this period, patients are required to be immobilized.

Incorporating the advantages of both bio-inert and resorbable materials, bioactive materials can elicit a specific biological response which offers an ideal solution by being able to rapidly form a stable bond with living tissue after implantation [67, 68]. Among the family of bioactive materials, bioactive glasses (BGs) which are based on SiO_2, CaO and P_2O_5 system have been extensively studied [69, 70]. The responses of these three types of materials are shown in Table 4.1.1.

Table 4.1.1 Types of tissue-implant interfacial responses.

	Bio-inert materials	**Resorbable materials**	**Bioactive materials**
Interfacial response	None (Mechanical fixation)	Dissolve and replace by surrounding tissue	Formation of interfacial bond
Materials	Alumina Al_2O_3 Zirconia ZrO_2	Tricalcium Phosphate $Ca_3(PO_4)_2$ Calcium sulfate $CaSO_4$	Hydroxyapatite $Ca_{10}(PO_4)_6(OH)_2$ Bioactive glasses SiO_2-CaO-P_2O_5

4.1.1.1 Bioactivity

Through the development of biomaterials, BGs have successfully competed against bio-inert and resorbable biomaterials. They have attracted enormous attention in the past few decades in the fields of bioengineering due to their superior bioactivity and numerous possible applications. BGs as bone implants, drug carriers and tooth repairing materials are now widely used in commercial products.

The term "bioactive" was first proposed by Hench et al. [8] in 1969. It was defined as follows. "*A bioactive material is one that elicits a specific biological response at the interface of the materials which results in the formation of an intermediate between the tissue and the material*". Various studies have demonstrated that when BGs are implanted into the human body, layers of hydroxyapatite, constituting the main mineral component of human bones, are formed on the surface of BGs [71-73]. These hydroxyapatite layers can chemically bond to human bones which reduces rejection and inflammation [74, 75]. Figure 4.1.1 shows a mechanism of bonding of bioactive glasses to living tissue which involves a sequence of several steps. During the past ten years, research into BGs has focused on how to enhance their bioactivity and this has led to the development and testing of various synthetic methods.

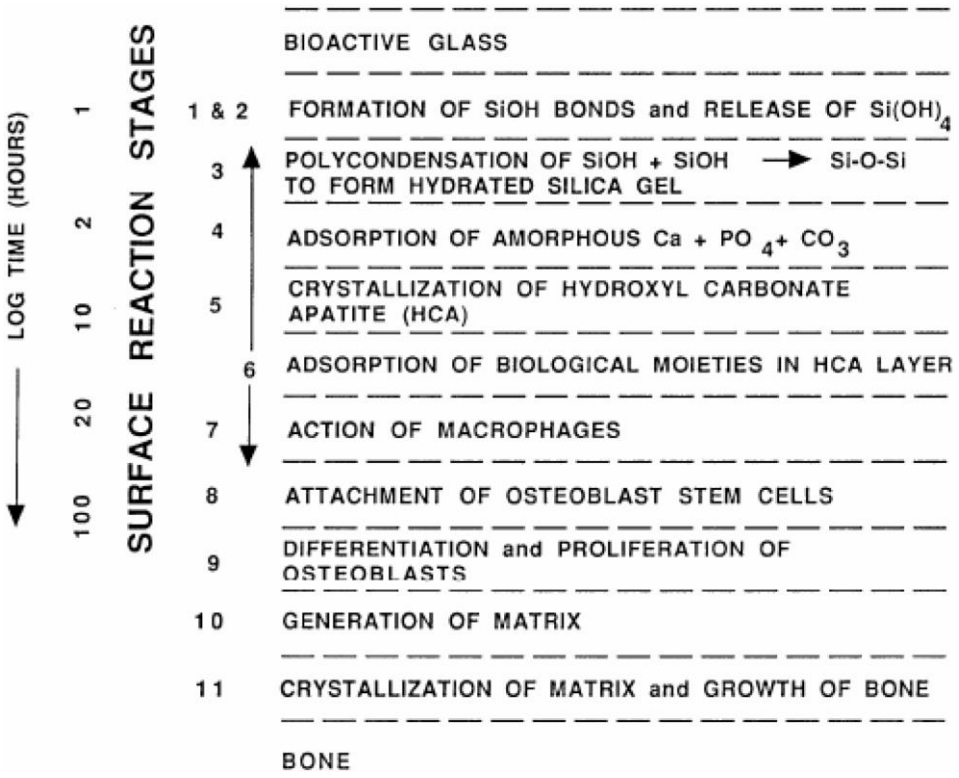


Figure 4.1.1 Sequence of interfacial reactions between bone and bioactive glasses, reproduced from [71].

4.1.1.2 Synthetic methods

The first BG reported by Hench et al. [8] was fabricated by a conventional glass smelting procedure. This process involved melting the raw materials at high temperatures of 1200-1400^{o}C and casting the melts into small rectangular implants. There are some advantages using this smelting procedure such as being able to produce the material in large quantities. However, the required high temperatures lead to disadvantages, such as high energy consumption, partial crystallization and also potential contamination. As BGs are fabricated for medical use, contamination must be avoided and purity must be assured [71].

In order to avoid some of the disadvantages caused by conventional glass smelting procedure, Li et al. [76] successfully synthesized BGs using a sol-gel method in 1991. This method has subsequently become one of the most popular BG fabrication methods. Three main reasons for its popularity are as follows:

The sol-gel method firstly offers a lower heat treatment temperature of around 600^{o}C compared to conventional glass smelting procedure (1200-1400^{o}C). Secondly, it provides a broader range and better control of the product's properties due to its chemical flexibility. Thirdly, by adding templates or surfactants into the precursor solution, different morphologies can be prepared, including solid, hollow or mesoporous structures. For example, Xia et al. [77] used a tri-block surfactant to successfully synthesize a well-ordered mesoporous bioactive glass in 2006. Although the sol-gel method has been widely used for BG fabrication, the overall process has the disadvantage of batch processing, *i.e.* it is difficult to adapt to mass production, which usually requires several steps with some of which need long periods of time. Typically, the whole process takes up to 4-7 days from start to collection of the final product.

Spray pyrolysis combines the advantages of both of the processes described above, *i.e.* it is suitable for mass production, operates lower temperature of around 500-600^{o}C and produces high purity BGs within a period of 1-2 days [78]. Spray pyrolysis involves dissolving the precursor ingredients in a solvent to form a precursor solution, which is then atomized into fine droplets using ultrasound and then introduced into a tube furnace to undergo three stages of solvent evaporation, solute precipitation and precursor

decomposition [79]. The synthesized BG particles are then collected in a high voltage electrostatic deposition system which is located immediately after the furnace. Figure 4.1.2 shows a schematic diagram of a typical spray pyrolysis setup and Table 4.1.2 gives a comparison of different procedures.

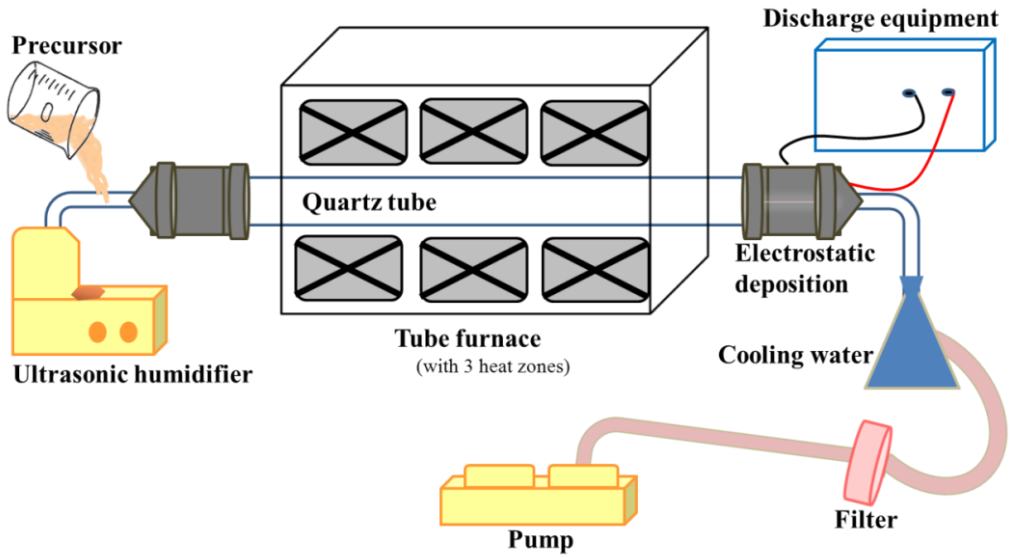


Figure 4.1.2 Schematic diagram of spray pyrolysis.

Table 4.1.2 Comparison of different preparation methods for BGs

		Conventional glass smelting process	**Sol-gel method**	**Spray pyrolysis**
Purity		Low	High	High
Process	Heat treatment	~1400^{o}C	~600^{o}C	~600^{o}C
	Processing time	1-2 days	4-7 days	1-2 days
	Mass production	Yes	No	Yes
Property	Chemical flexibility	Poor	Good	Good
	Structure modification	Difficult	Easy	Easy
	Bioactivity	Narrow range	Broad range	Broad range

To understand structure-properties correlations in BGs one needs to know their structures, and thus in this thesis BGs prepared by spray pyrolysis were studied due to their superior bioactivity and increasing potential for clinical applications.

4.1.2 Structural Analysis of Bioactive Glasses

In this study, two BG particles with different compositions, $60SiO_2$-$35CaO$-$5P_2O_5$ and $80SiO_2$-$15CaO$-$5P_2O_5$, were synthesised by Prof. Shao-Ju Shih and colleagues at the National Taiwan University of Science and Technology using the spray pyrolysis method. The specimens show different bioactivity and the main focus of this study is to correlate the different bioactivities to their structure.

4.1.2.1 Experimental RDF Analysis of Bioactive Glasses

The powders were first transferred onto TEM grids by dispersing in acetone and placing drops of suspensions onto TEM grids coated with a lacey carbon film. A lacey carbon film was chosen to minimize the influence of the carbon support on the data. The specimens were then loaded into JEOL-2100 microscope using the experimental setup described earlier in Section 2.4.1. Figures 4.1.3 (a) and (b) show BG particles imaged at 40,000X magnification with a nanobeam probe size of around 280nm and Figures 4.1.3 (c) and (d) show their corresponding nanobeam diffraction patterns. After RDF analysis was performed, the resulting $\varphi(\boldsymbol{q})$ and $G(\boldsymbol{r})$ of both BG particles are shown in Figure 4.1.4.

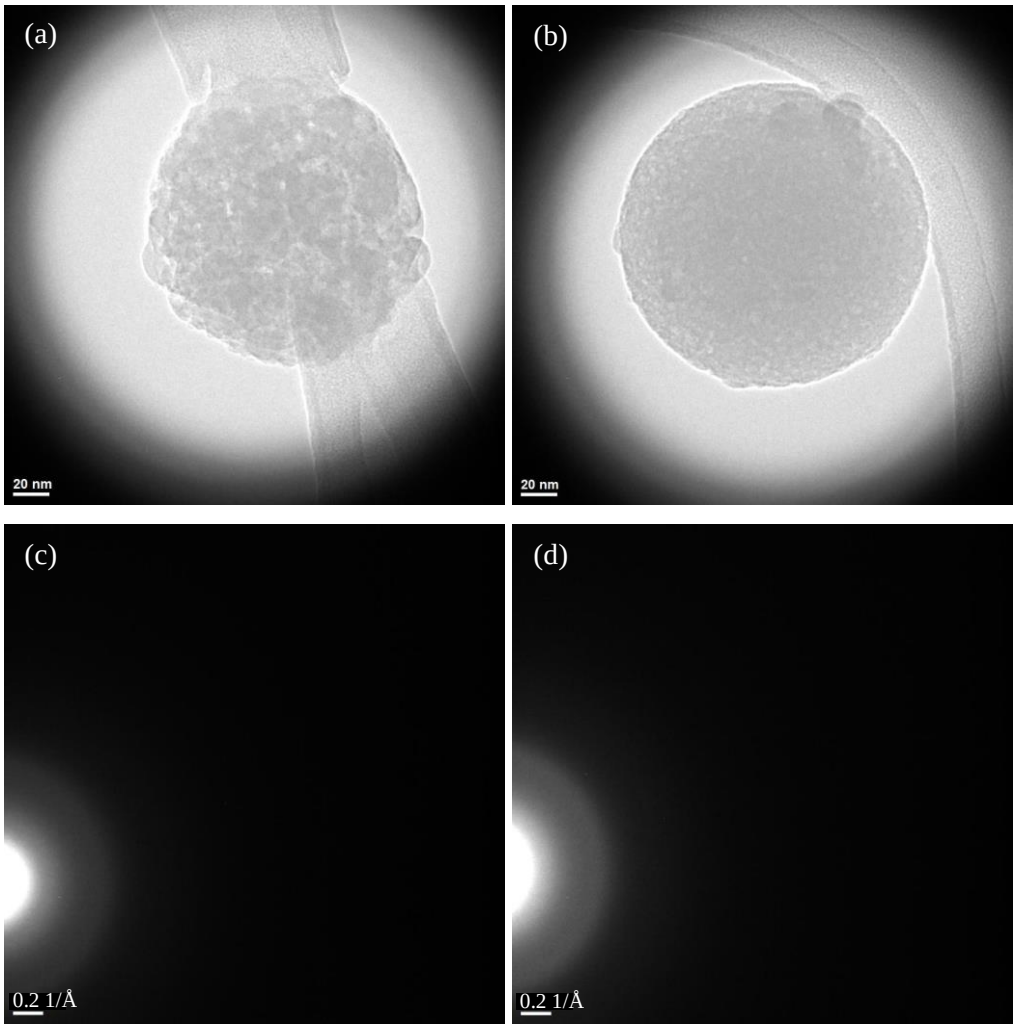


Figure 4.1.3 TEM images of BG particles, (a) 60SiO_2-35CaO-5P_2O_5 and (b) 80SiO_2-15CaO-5P_2O_5, and (c, d) their corresponding diffraction patterns.

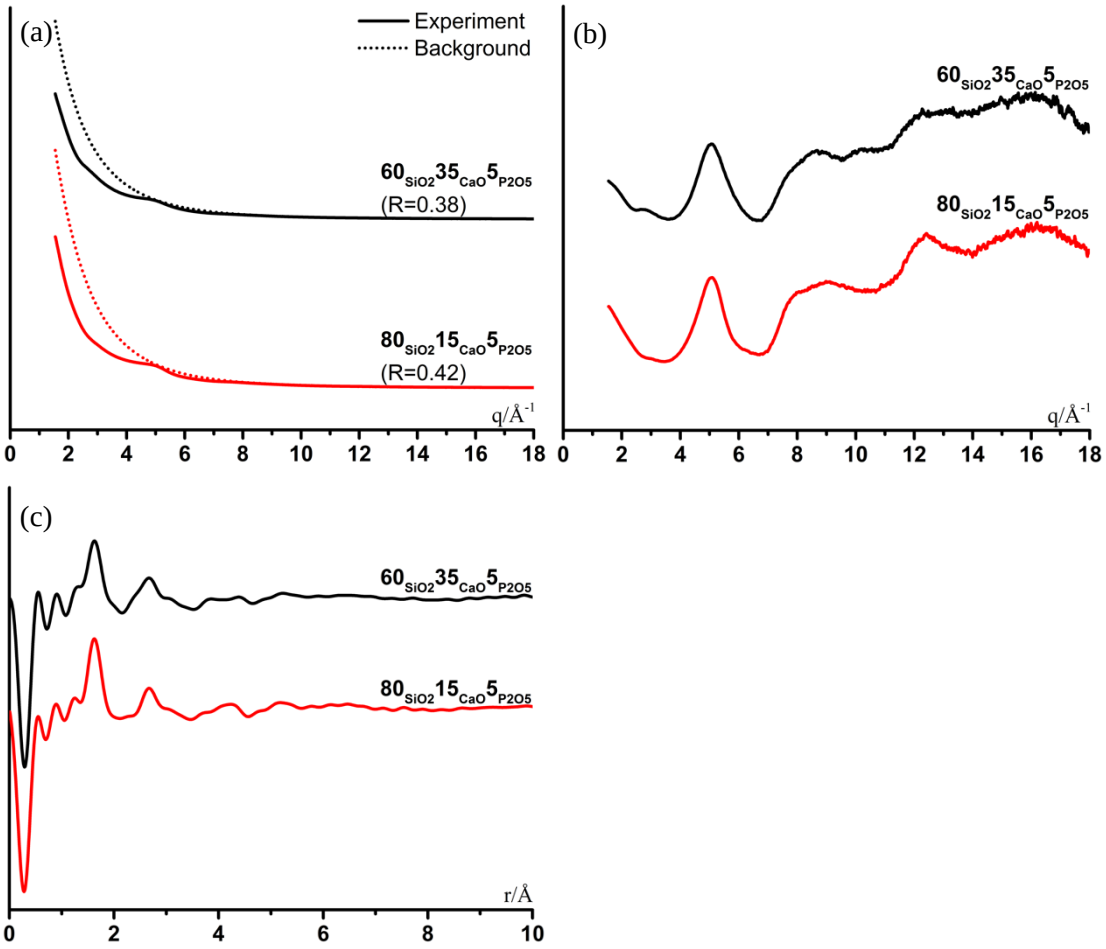


Figure 4.1.4 (a) $I(\boldsymbol{q})$ and background fit, (b) $\varphi(\boldsymbol{q})$ and (c) $G(\boldsymbol{r})$ for BG nanoparticles.

It can be seen from Figures 4.1.3 (a) and (b) that the SP-derived BG particles have a spherical shape. For the RDF analysis, particles with similar size were selected to minimize the level of influence of multiple scattering as discussed in Section 3.2. The diffraction patterns shown in Figures 4.1.3 (c) and (d) were centred at the edge of the camera to acquire intensity to higher scattering angles. However, both particles still have thickness of up to 150nm, which results in poor background fitting (*R* around 0.4) of the atomic scattering as shown in Figure 4.1.4 (a). This poor fitting affects $\varphi(\boldsymbol{q})$ and thus results in a negative peak in the $G(\boldsymbol{r})$ curves as shown in Figure 4.1.4 (b). To correct this,

a Fourier filter described in Section 3.1.3 was applied and the filtered $\varphi(\boldsymbol{q})$ and $G(\boldsymbol{r})$ are shown in Figure 4.1.5.

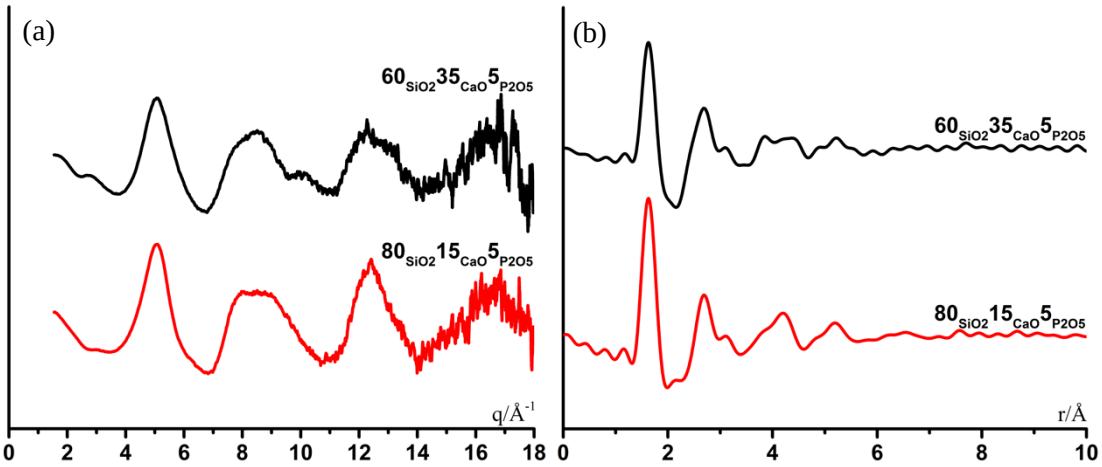


Figure 4.1.5 (a) $\varphi(\boldsymbol{q})$ and (b) $G(\boldsymbol{r})$ extracted from both BG particles after Fourier filtering.

After the Fourier filter was applied, both $\varphi(\boldsymbol{q})$ oscillate around zero as shown in Figure 4.1.5 (a) and the negative peaks are absent in both $G(\boldsymbol{r})$ curves as shown in Figure 4.1.5 (b). It is observed that both $G(\boldsymbol{r})$ curves exhibit peaks around 1.6, 2.6 and 3.1Å which correspond to bonded Si-O and non-bonded O…O, and Si…Si distances, respectively. Comparison of both $G(\boldsymbol{r})$ curves shows that the peak at 1.6Å is higher for $80SiO_2$-$15CaO$-$5P_2O_5$ glass due to larger contribution from Si-O bonds. Moreover, a shoulder at around 2.6Å is evident in $G(\boldsymbol{r})$ of the $60SiO_2$-$35CaO$-$5P_2O_5$ glass which corresponds to the Ca…O first neighbour distances.

4.1.2.2 Simulated DFT Models and RMC Refinement of Bioactive Glasses

For better interpretation of the structural data, DFT simulations along with RMC refinements were carried out. The parameters used for DFT simulation were set as described in Section 3.1.2. Both models were quenched from 3000K to 300K followed by an energy optimisation, Figures 4.1.6 (a) and (b) show the DFT simulated models of both BGs and the $G(\boldsymbol{r})$ curves calculated from the models are shown in Figure 4.1.6 (c).

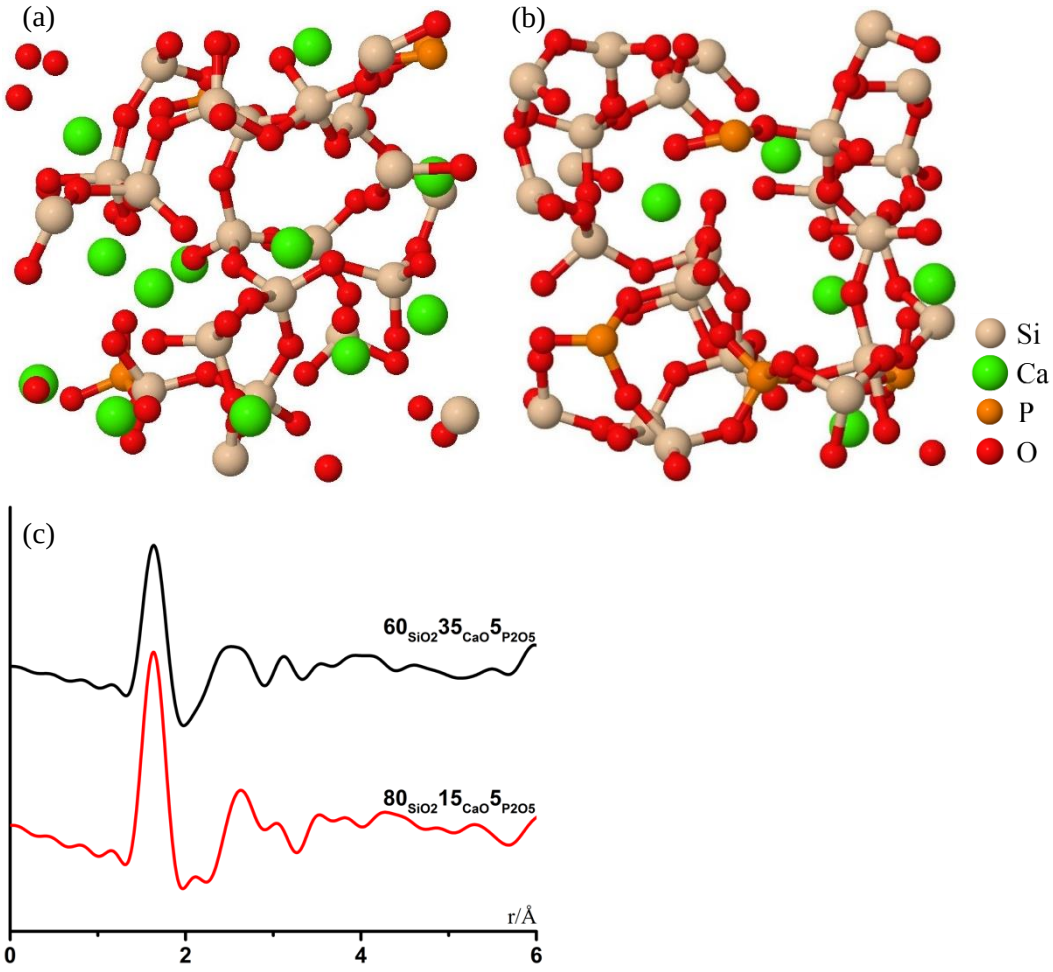


Figure 4.1.6 DFT simulated models of (a) 60%SiO2-35%CaO-5%P2O5 glass and (b) 80%SiO2-15%CaO-5%P2O5 glass. (c) Corresponding $G(\boldsymbol{r})$ curves calculated from these models.

From Figures 4.1.6 (a) and (b), it can be seen that both models consist of tetrahedral SiO_2 units and that the $60SiO_2$-$35CaO$-$5P_2O_5$ glass (Figure 4.1.6 (a)) has more Ca compared to the $80SiO_2$-$15CaO$-$5P_2O_5$ glass (Figure 4.1.6 (b)). In addition, $G(\boldsymbol{r})$ shown in Figure 4.1.6 (c) shows a similar trend to the experimental results discussed in Figure 4.1.5 , *i.e.* the $80SiO_2$-$15CaO$-$5P_2O_5$ glass has a higher first peak at 1.6Å due to more abundant Si-O bonds with a shoulder in $G(\boldsymbol{r})$ from the $60SiO_2$-$35CaO$-$5P_2O_5$ glass at around 2.6Å due to a higher contribution of Ca…O distances.

For more detailed analysis, RMC refinements were then performed using both models as starting structures and the results are shown in Figure 4.1.7 along with the corresponding RDF curves.

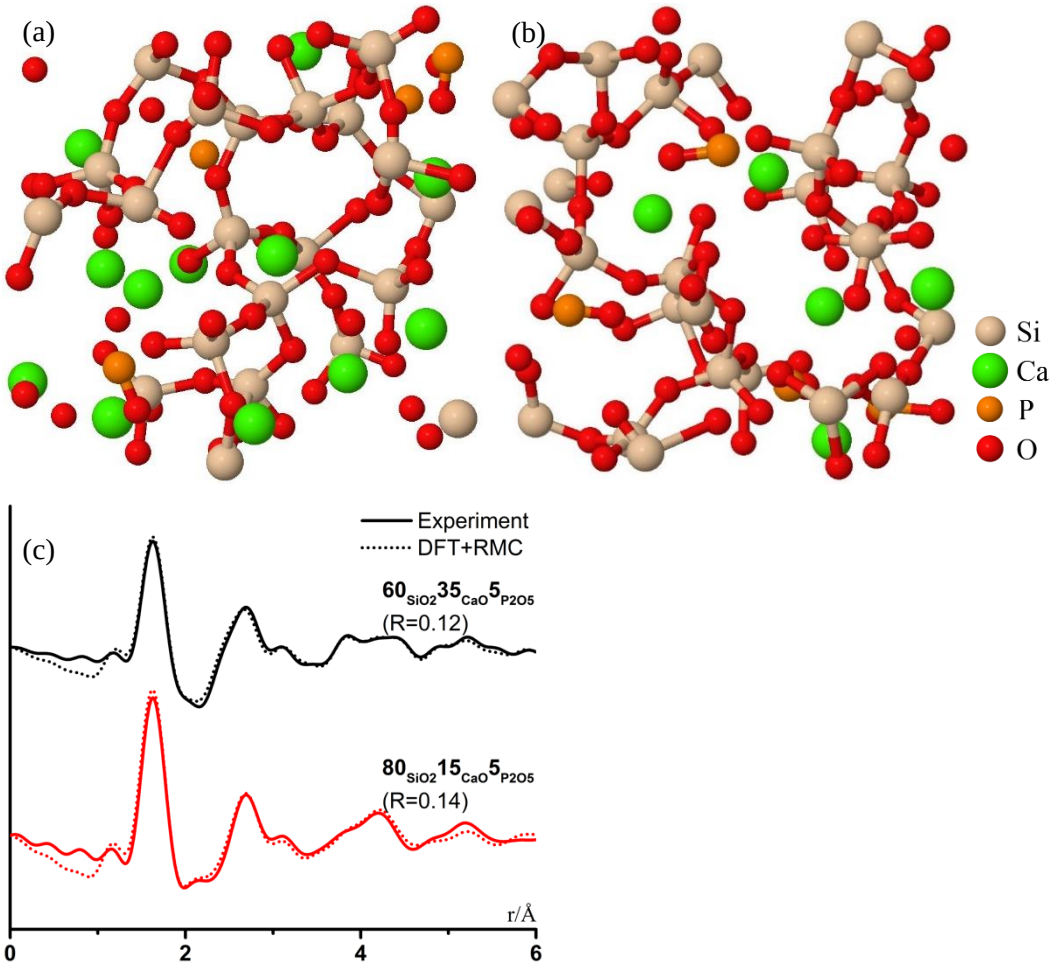


Figure 4.1.7 RMC refined models of (a) 60%SiO_2-35%CaO-5%P_2O_5 glass and (b) 80%SiO_2-15%CaO-5%P_2O_5 glass. (c) Corresponding $G(\boldsymbol{r})$ curves calculated from these models.

After the RMC refinements, it can be seen from Figures 4.1.7 (a) and (b) that the tetrahedral SiO_2 structure of both models remains and their corresponding $G(\boldsymbol{r})$ curves are in good agreement (R = 0.12 and 0.14) with experimental data. The resulting models were then used to calculate partial pair distribution functions as shown in Figure 4.1.8 to compare structural differences in detail.

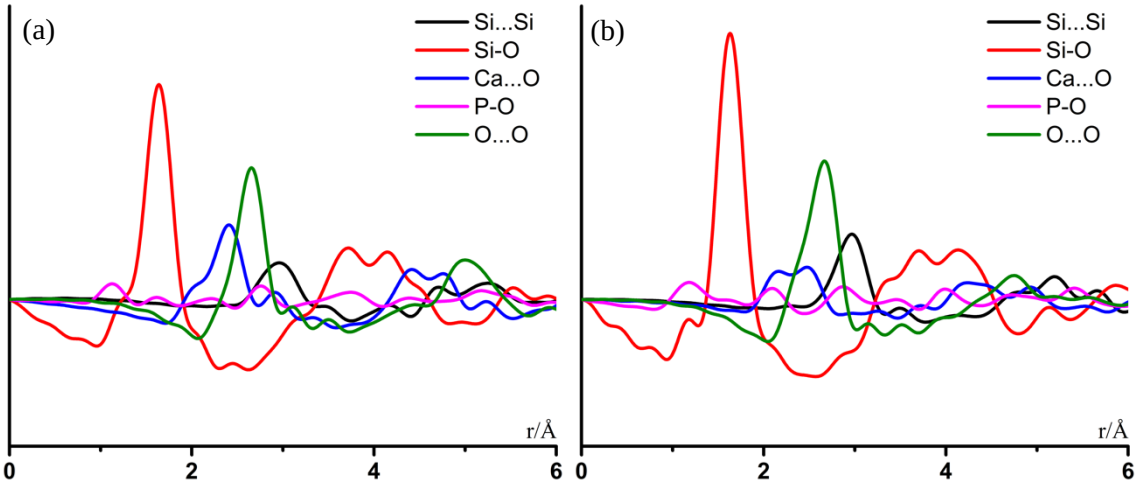


Figure 4.1.8 Partial pair distribution functions calculated from the models of (a) 60SiO_2-35CaO-5P_2O_5 glass and (b) 80SiO_2-15CaO-5P_2O_5 glass.

It can be seen from Figure 4.1.8 that the structures of both glasses exhibit similar contributions from P-O and O…O distances. However, the 60SiO_2-35CaO-5P_2O_5 glass shows fewer Si-O and Si-Si distances but more Ca…O distances compared to the 80SiO_2-15CaO-5P_2O_5 glass. In addition, it can be seen from both data that the contribution of Ca…O can be divided into two peaks around 2.2Å and 2.4Å. The same number of 2.2Å Ca…O distances is observed in both glasses, however, the 60SiO_2-35CaO-5P_2O_5 glass shows more Ca…O distances around 2.4Å than the 80SiO_2-15CaO-5P_2O_5 glass.

4.1.3 Structure-Property Correlations in Bioactive Glasses

After acquiring structural information using experimental RDFs and simulated models, the bioactivity of the glasses was measured to explore structure-property correlations. The in vitro bioactive tests were carried out by Prof. Shao-Ju Shih and colleagues and the detailed procedures are listed below. The BG powders were first immersed into simulated body fluid (SBF) [80], which has an ionic concentration nearly equal to human plasma, with a solid to liquid ratio of 1mg to 1mL and the mixtures were held at 37ºC for various times from 1h to 6h. Secondly, the powders were removed and washed three times, twice with acetone and once with de-ionized water, before drying at room temperature for one day. Finally, the dried powders were characterised using XRD to monitor the formation of hydroxyapatite. XRD patterns of both glasses before and after immersion in the simulated body fluids (SBF) for various durations are shown in Figure 4.1.9 below.

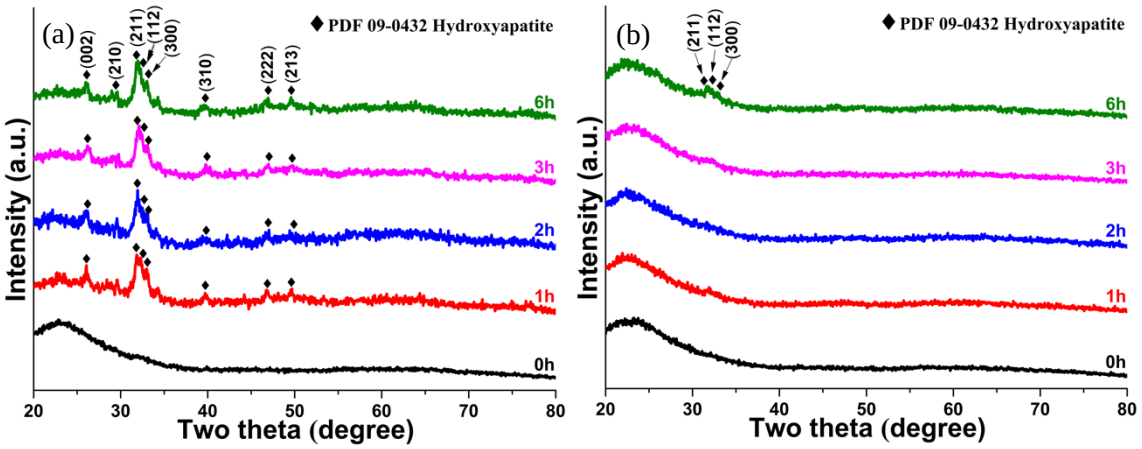


Figure 4.1.9 XRD patterns of BG particles with different compositions before (0h) and after immersion in SBF solutions for various durations (1, 2, 3, 6h). (a) 60%SiO_2-35%CaO-5%P_2O_5 glass and (b) 80%SiO_2-15%CaO-5%P_2O_5 glass.

It can be seen from Figure 4.1.9 that both glasses are XRD amorphous before immersion into the SBF solution. After 1h of immersion, the growth of hydroxyapatite can be observed in the $60SiO_2$-$35CaO$-$5P_2O_5$ glass which shows Bragg peaks at 25.9, 29.3, 31.8, 32.2, 33.7, 39.4, 46.7, and 49.6º which were identified as the (002), (210), (211), (112), (300), (310), (222) and (213) reflections from of hydroxyapatite (JCPDS number: 09-0432). In contrast, the $80SiO_2$-$15CaO$-$5P_2O_5$ glass only has a small peak that appears after immersion for 6h.

In the current bioactivity tests, the hydroxyapatite phase formed notably earlier in the $60SiO_2$-$35CaO$-$5P_2O_5$ glass (after 1h soaking) than in the $80SiO_2$-$15CaO$-$5P_2O_5$ glass (after 6h soaking) as shown in Figure 4.1.9. This suggests that the $60SiO_2$-$35CaO$-$5P_2O_5$ glass has a higher bioactivity than the $80SiO_2$-$15CaO$-$5P_2O_5$ glass. Comparing the average nearest neighbour distances in hydroxyapatite for P-O, 1.5Å, and Ca…O, 2.4Å, (Figure 4.1.10) with the partial pair distribution functions in Figure 4.1.8, shows that the increase of the bioactivity may be due to the presence of a Ca…O distance which are commensurate with the Ca…O distance in hydroxyapatite. It is possible that the Ca…O distances act as a nucleation centre at the early stage of precipitation which helps the $60SiO_2$-$35CaO$-$5P_2O_5$ glass to precipitate the hydroxyapatite phase on its surface.

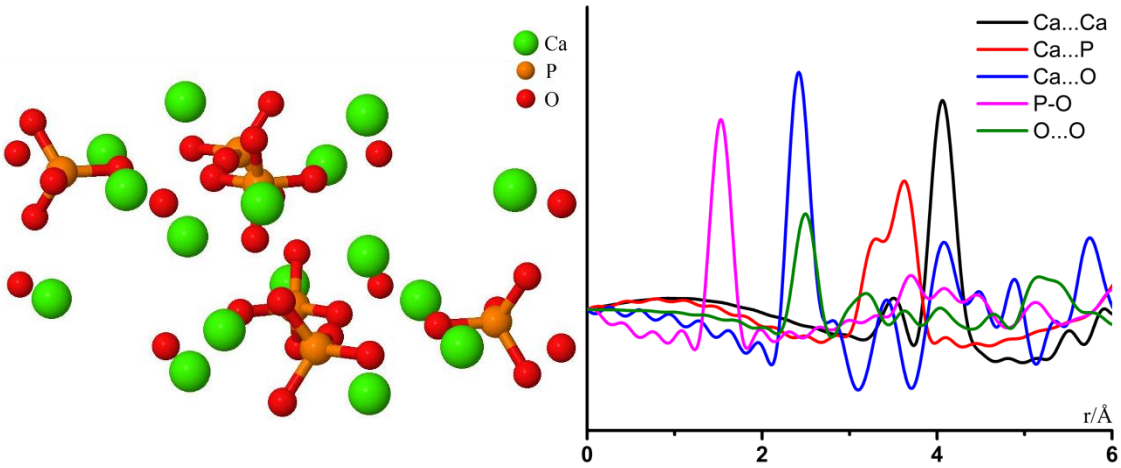


Figure 4.1.10 (a) Hydroxyapatite structure and (b) its corresponding partial pair distribution functions.

Although the present study supports this hypothesis, further studies will be required to test the validity of this idea across a range of specimens.

4.2 Ti-Si Metallic Glasses

4.2.1 Introduction

Metallic glasses, (amorphous alloys), are solid metallic materials which lack long-range order. Due to their amorphous structure and the absence of grain boundaries, metallic glasses possess unique mechanical and chemical properties, which in many cases are superior to crystalline metals [81, 82]. However, several drawbacks such as fracture toughness and fatigue limits have been reported which are highly dependent on material quality, oxygen content and the presence of unwanted phases or partial crystallisation [83, 84].

4.2.1.1 Bulk Metallic Glasses

The first metallic glass was prepared at the California Institute of Technology by Duwez [85] in 1960 . Quenching melted metal constituents at high cooling rates of 10^5-10^6 K/s, bypassed the process of nucleation and crystal growth to form the first metallic glass with a composition $Au_{75}Si_{25}$. Subsequently, glass formation of Pd- [86, 87] and Ti-based alloys [88] has been reported. However, the sample sizes of most metallic glasses are limited to a few millimetres due to the high critical cooling rate required [89].

It is not until 1988, when Inoue et al. [90] demonstrated that bulk metallic glasses (BMGs), with sample sizes in excess of 1 mm, can be fabricated based on a Mg-Ln-M (Ln = Lanthanide metal, M = Ni, Cu or Zn) alloy system by copper mould casting with a lower cooling rate of 1 to 100 K/s. Since then, a number of BMGs have been developed owing to their scientific importance and engineering applications [91-93]. For instance, Zr-based

BMGs that exhibit the high glass forming ability, with sample sizes up to 14 mm, and excellent mechanical properties have been commercialized [94, 95].

For BMGs, an important factor is the glass forming ability (GFA) which is described as the maximum sample size of the amorphous alloy. This factor indicates the ability of a metallic alloy to transform into the amorphous state, which is important for designing and developing new BMGs with larger sample size. To understand this factor, Inoue [96] considered thermodynamic, kinetic and structural aspects and formulated three basic empirical rules for BMG formation: Firstly, the alloy must contain at least three components. Secondly, differences in atomic sizes must be more than 12% among all of the three main constituent elements. Thirdly, the heat of mixing (ΔH_{mix}) of the major constituent elements should be negative. These criteria will cause an increase in structural complexity, optimum packing and bonding states as well as increasing the difficulty of redistributing the constituent elements, thus avoiding formation of a crystalline phase and lead to a higher GFA. Moreover, several glass forming criteria have been proposed, considering different aspects of the GFA, to predict glass formation in alloy systems [97, 98].

4.2.1.2 Thin Film Metallic Glasses

With increasing interest in developing and understanding BMGs, thin film metallic glasses (TFMGs) have also been studied as potential antibiotic coatings and for micro-electro-mechanical system devices such as chips and sensors [99, 100].

Studies of TFMGs started in the 1980s and were mainly focused on immiscible binary systems such as Cu-Ta and Cu-W [101]. It was not until the late 1990s, when many new BMGs with good GFA were developed by Inoue et al. [96], that TFMGs gradually received attention for potential applications [99, 102, 103]. TFMGs prepared by vapour-to-solid deposition are expected to have better GFA than those prepared by a liquid-to-solid melting or casting process owing to the non-equilibrium process. Thus, thin film processing such as sputtering can provide TFMGs with improved GFA and wider composition ranges for glass formation [104].

Owing to their excellent corrosion resistance and mechanical properties, Zr- and Pd-based TFMGs are appropriate candidates for micro-electro-mechanical system applications. For example, Zr-Cu-Al and Pd-Cu-Si ternary TFMGs were sputtered by Hata et al. [99] and Liu et al. [102] for these applications in micro-actuators.

Apart from applications in electronics, Rhinow et al. [103] have proposed a thin film of $Ti_{88}Si_{12}$ metal glass as an alternative to carbon for cryo-electron microscopy. They claimed that Ti-Si support films are able to reduce beam-induced movement owing to their high electrical conductivity. In addition, their high mechanical strength allows Ti-Si films

to be ~10 times thinner than amorphous carbon film such that they would contribute less background noise to recorded images.

Following Rhinow's work, Dr Jefferson Bettini and colleagues have synthesize Ti-Si films with various compositions. They have demonstrated that a Ti-Si thin film with a Ti composition varying from 70 to 90 percent can be used as an option to replace carbon thin films on TEM grids. Within this range, the thin films of Ti-Si are amorphous and show high stability under electron beam irradiation, lower resistivity and low roughness. However, a few specimens have known phase separation within the structure, therefore the present work has investigated the atomic local structure of Ti_xSi_{100-x} (x = 89, 83, 79, 74, 70) thin film samples to provide more information about the texture within the specimens.

4.2.2 Structural Analysis of Ti-Si Metallic Glasses

All Ti-Si metallic glasses studied in this thesis were prepared by Dr Jefferson Bettini and colleagues at Brazilian Nanotechnology National Laboratory.

The following process to prepare TEM samples was used: Thin films of amorphous Ti-Si metallic glasses with different compositions were grown by thermal evaporation using a tungsten boat. An alloy of $Ti_{88}Si_{12}$, which has a lower melting point than pure Ti metal, was used as a Ti source. Si with 99.99% purity was used as the source of Si. The composition of the thin film Ti-Si metallic glasses was controlled by the amount of pure Si added to the boat. The growth rate was measured by a quartz crystal and controlled by the amount of current passing through the tungsten boat which varied between 0.2 - 0.4Å/s. All Ti-Si thin film metallic glasses around 10nm were deposited onto freshly cleaved mica sheets at a pressure ranging between $1 \cdot 10^{-6}$ to $3 \cdot 10^{-5}$ torr. The deposited thin films were then removed from the substrate and placed onto 300mesh TEM grids.

4.2.2.1 Experimental RDF Analysis of Ti-Si Metallic Glasses

Diffraction experiments were carried out using a JEOL-2100 microscope, as described in Section 2.4.1. Figure 4.2.1 shows diffraction patterns of all five Ti-Si films with varying compositions and their corresponding intensity profiles.

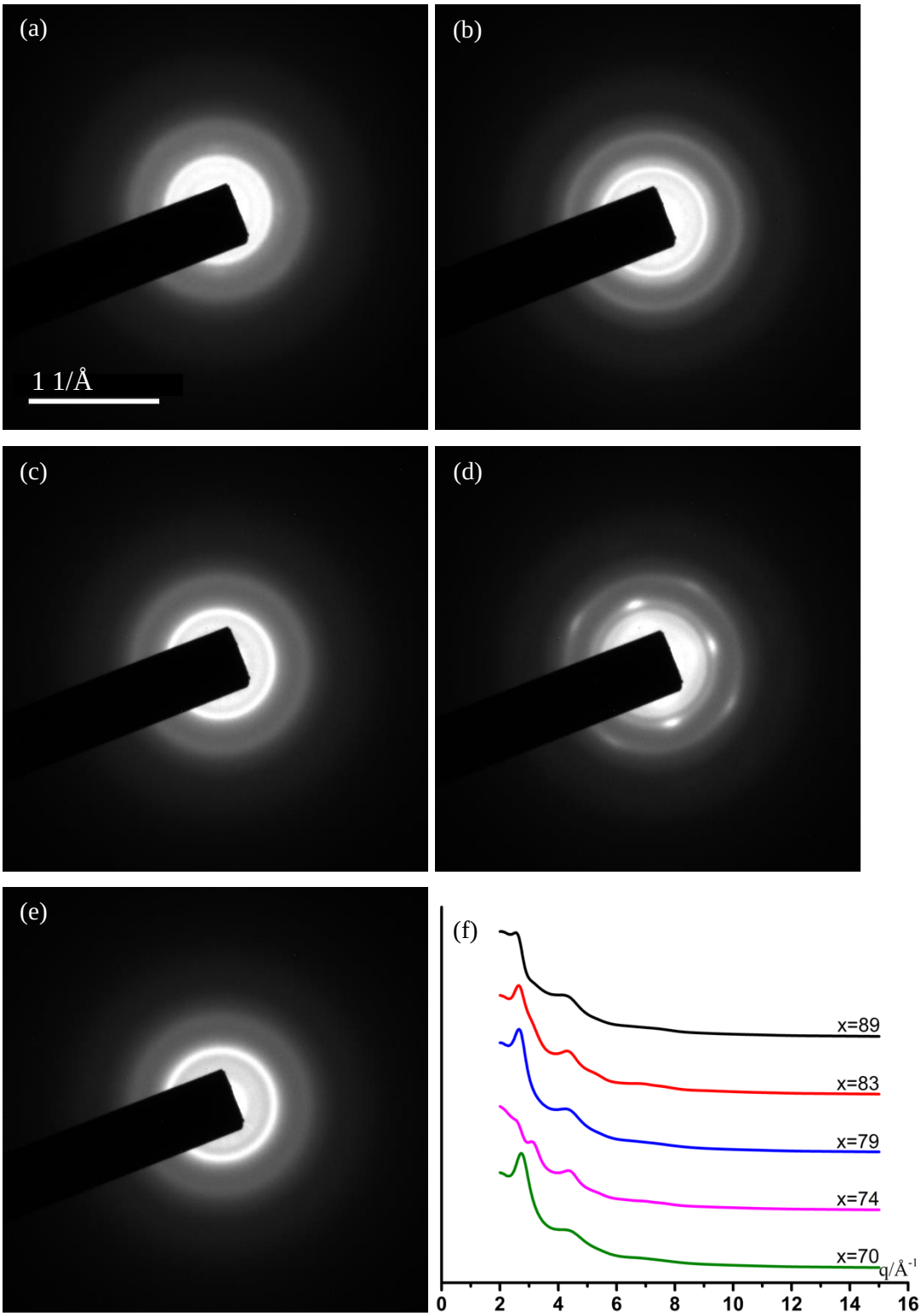


Figure 4.2.1 Electron diffraction patterns of Ti_xSi_{100-x} metallic glass films. (a) x=89, (b) x=83, (c) x=79, (d) x=74, (e) x=70. (f) Corresponding intensity distribution functions.

It can be clearly seen from Figure 4.2.1 that films with Ti fractions of x = 83, 79 and 70 show azimuthally uniform patterns without any obvious diffraction maxima, indicating an amorphous phase. In contrast, films with x = 74 and 89 have faint localised diffraction maxima which are more pronounced in the x = 74 film. By azimuthal averaging these faint spots, the RDF analysis were performed based on their nominal compositions Ti_xSi_{100-x}, this regard the crystallinity as polycrystalline and hence the output might present some deviations. However, the overall nearest neighbour distances will not be affected. Figure 4.2.2 shows the $I(\boldsymbol{q})$ fitting and resulting $\varphi(\boldsymbol{q})$ and $G(\boldsymbol{r})$ curves.

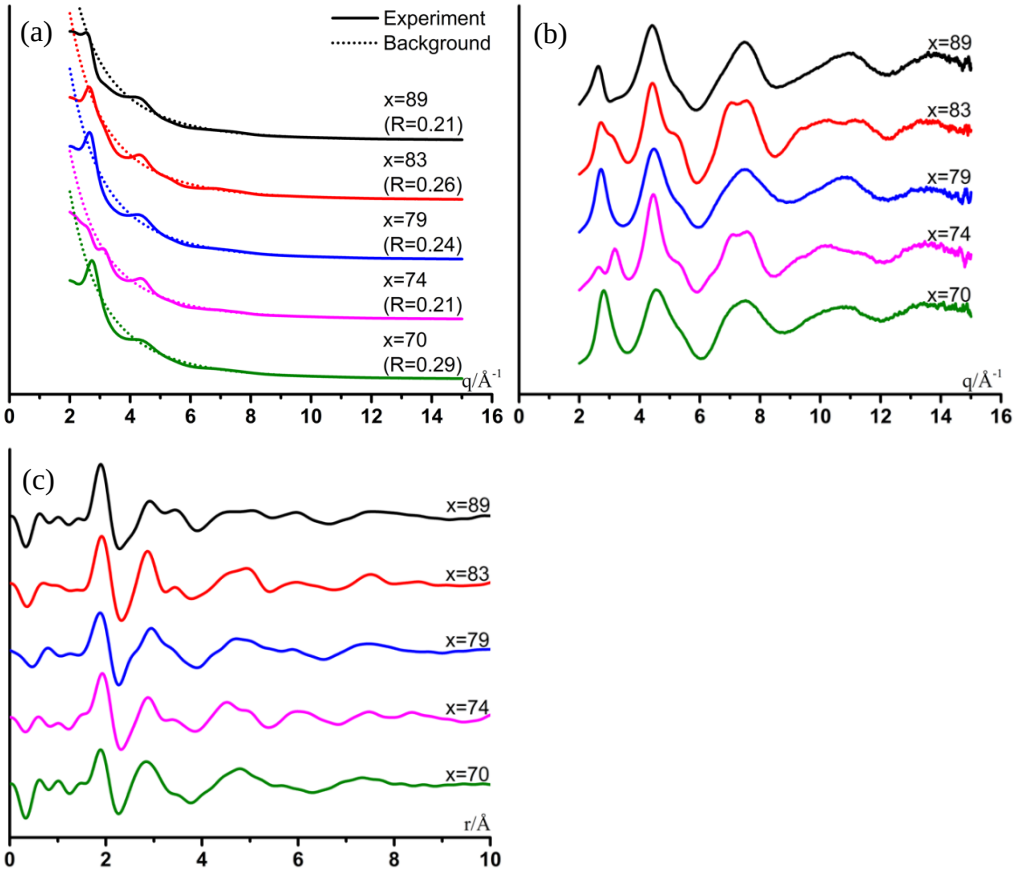


Figure 4.2.2 (a) $I(\boldsymbol{q})$ background fits, (b) $\varphi(\boldsymbol{q})$ and (c) $G(\boldsymbol{r})$ extracted from all five Ti-Si films (RDF fitting based on nominal compositions of Ti_xSi_{100-x}).

All background fittings shown in Figure 4.2.2 (a) indicate R = 0.2 ~ 0.3 of the atomic scattering background with their resultant $\varphi(\boldsymbol{q})$ curves oscillating around zero as shown in Figure 4.2.2 (b). After Fourier transformation, all five G(r) curves are shown in Figure 4.2.2 (c) with the presence of a notable peak at around 1.9Å. However, the atomic covalent radii for Ti and Si are 1.76Å and 1.11Å, respectively, corresponding to a Ti-Si bond length of 2.87Å. Hence, the peak at 1.9Å should not be present in a pure Ti-Si system. After verification using atomic covalent radii, the peak of 1.9Å was assigned to Ti-O bonds, which indicates that the all five films have been oxidised.

Since the Ti-O peak is more intense than all other peaks, it is suggested that all Ti-Si films are oxidised. To confirm this, Energy-dispersive X-ray spectroscopy (EDS) analysis was carried out to characterise their atomic compositions and the results are shown in Figure 4.2.3.

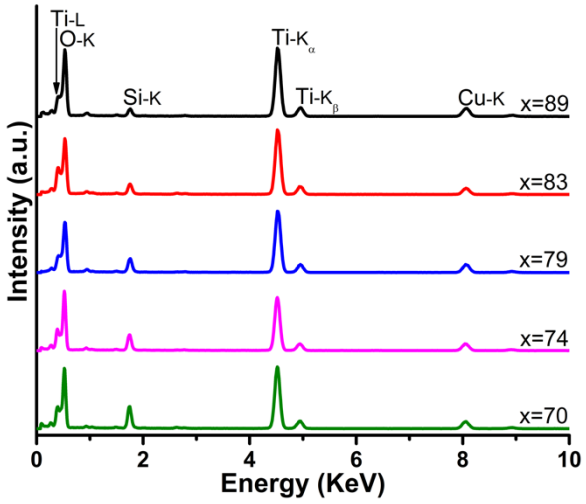


Figure 4.2.3 EDS spectra of Ti_xSi_{100-x} metallic glass specimens.

It can be seen from Figure 4.2.3 that all EDS spectra show peaks at 0.53, 1.76, 4.52, 4.96 and 8.07KeV which correspond to O-K, Si-K, Ti-K_α, Ti-K_β and Cu-K edges, respectively. A small shoulder on O-K edge peak around 0.42KeV is also observed which corresponds to the Ti-L edge.

Quantitative EDS analysis were carried out using the Digital Micrograph Suite Software. By performing background fitting from 0.42-0.6KeV for the O-K edge, 1.62-1.92KeV for the Si-K edge and 4.30-4.72KeV for the Ti-K_α edge, quantitative atomic compositions were calculated as given in Table 4.2.1. For quantitative analysis, Cliff and Lorimer [105] showed that the ratio of elements A and B can be expressed as $C_A/C_B = k_{AB}(I_A/I_B)$ where k_{AB} is a "k-factor" relating the concentration ratio (C_A and C_B) and the ratio of integrated intensities (I_A and I_B). For accurate quantitative analysis, the k-factor needs to be calibrated and in this study the k-factor for Si: O (k_{SiO}) was calibrated using an amorphous SiO2 specimen while k_{TiSi} for the Ti: Si ratio was calibrated using the nominal Ti_xSi_{100-x} ratio.

Table 4.2.1 Quantitative atomic composition from EDS. (a) Before and (b) after k-factor calibration.

(a)	$Ti_{89}Si_{11}$	$Ti_{83}Si_{17}$	$Ti_{79}Si_{21}$	$Ti_{74}Si_{26}$	$Ti_{70}Si_{30}$
Ti	38.1±0.7	41.2±0.9	40.7±1.0	34.5±2.2	36.8±1.0
Si	3.8±0.1	6.3±0.1	8.6±0.1	9.7±0.5	12.4±0.4
O	58.1±0.8	52.5±1.0	50.7±1.1	55.8±2.8	50.8±1.3
Ti: Si ratio	91:9	87:13	83:17	78:22	75:25

Unit: at%

(b)	$Ti_{89}Si_{11}$	$Ti_{83}Si_{17}$	$Ti_{79}Si_{21}$	$Ti_{74}Si_{26}$	$Ti_{70}Si_{30}$
Ti	36.0±0.7	38.8±0.8	38.2±1.1	32.2±2.1	34.2±0.9
Si	4.5±0.1	7.5±0.1	10.2±0.1	11.4±0.7	14.5±0.4
O	59.5±0.8	53.6±0.9	51.6±1.1	56.4±2.8	51.3±1.3
Ti: Si ratio	89:11	84:16	79:21	74:26	70:30

Unit: at%

Table 4.2.1 (a) gives the atomic composition before the k-factor calibration, showing a Ti: Si ratio with an error of less than 5at% to the given Ti_xSi_{100-x} ratio and with the percentage of oxygen in all films greater than 50at%. After the k-factor calibration for Si: O and Ti: Si ratio, the Ti: Si ratio is perfectly matched with the nominal Ti_xSi_{100-x} ratio and the oxygen ratios increased by about 1at% as compared to the non-corrected data.

After acquiring the experimental atomic composition from quantitative EDS analysis, the RDF analysis was repeated using the new atomic composition and the resulting $\varphi(\boldsymbol{q})$ and $G(\boldsymbol{r})$ are shown in Figure 4.2.4.

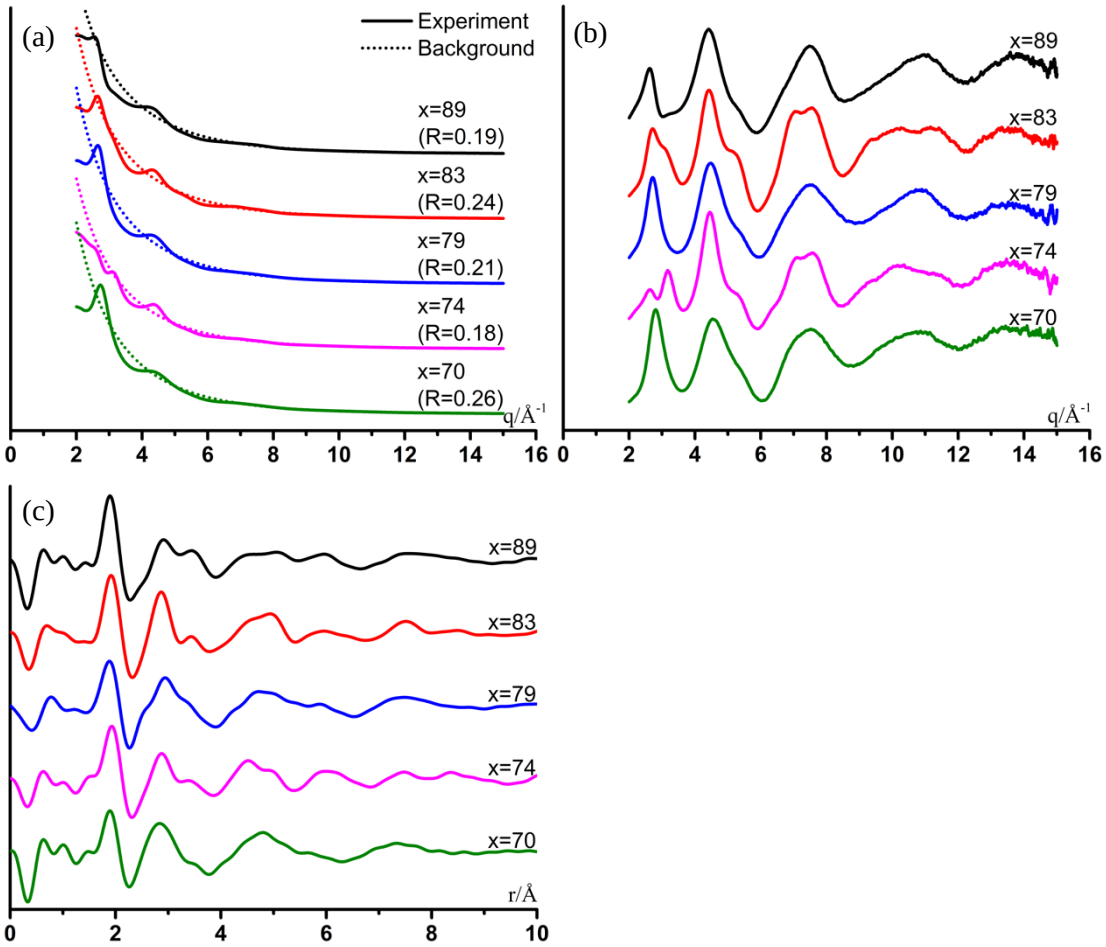


Figure 4.2.4 (a) $I(\boldsymbol{q})$ background fits, (b) $\varphi(\boldsymbol{q})$ and (c) $G(\boldsymbol{r})$ extracted from all five Ti-Si-O films (RDF fitting based on quantitative EDS compositions).

By comparison with Figure 4.2.2 (a), it can be seen from Figure 4.2.4 (a) that the $I(\boldsymbol{q})$ background fits for all films improved by around 2-3% better using quantitative EDS compositions which leads to more accurate $\varphi(\boldsymbol{q})$ and $G(\boldsymbol{r})$ results as shown in Figures 4.2.4 (b) and (c).

4.2.2.2 Simulated DFT Models of Ti-Si Metallic Glasses

Based on the experimental RDF curves and EDS analysis, it can be seen that all five Ti-Si films are partially oxidised. Since the oxidation occurred at the surface of the film, a liquid quench simulation with only one supercell might not be a sufficiently accurate model. Therefore, instead of using one partially oxidised model, two models of pure and fully oxidised films were simulated.

The parameters used for DFT simulation were set as described in Section 3.1.2. Both models were quenched from 3000K to 300K followed by an energy optimisation. However, the resulting structures optimised with a 300eV cut-off energy were not converged, and thus a cut-off energy of 400eV was used. Figure 4.2.5 shows all five pure Ti-Si models and Figure 4.2.6 shows all five oxidised Ti-Si-O models along with their corresponding $G(\boldsymbol{r})$ curves.

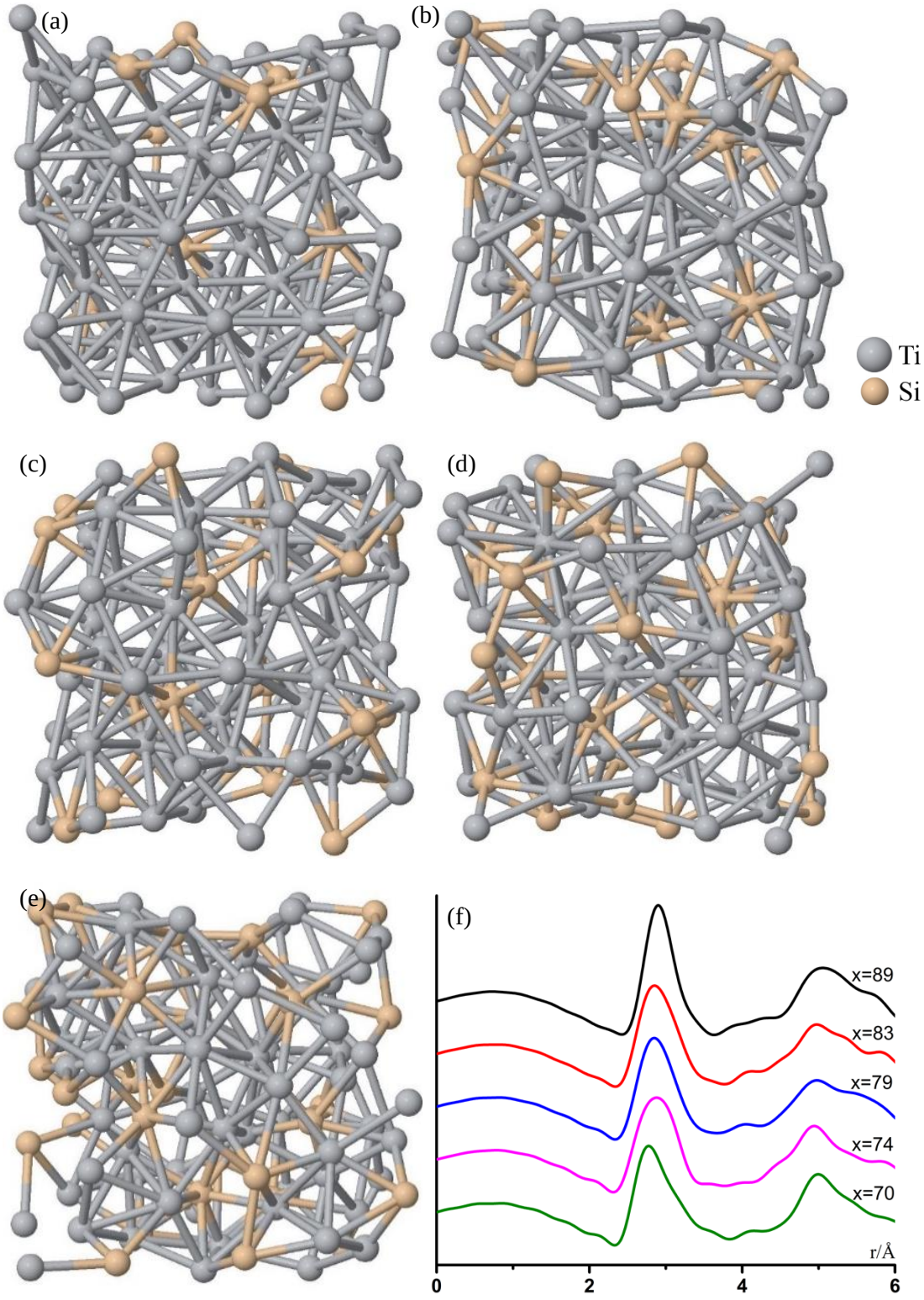


Figure 4.2.5 Simulated models of pure Ti_xSi_{100-x} metallic glasses, (a) x=89, (b) 83, (c) 79, (d) 74 and (e) 70, along with (f) their corresponding $G(\boldsymbol{r})$ curves.

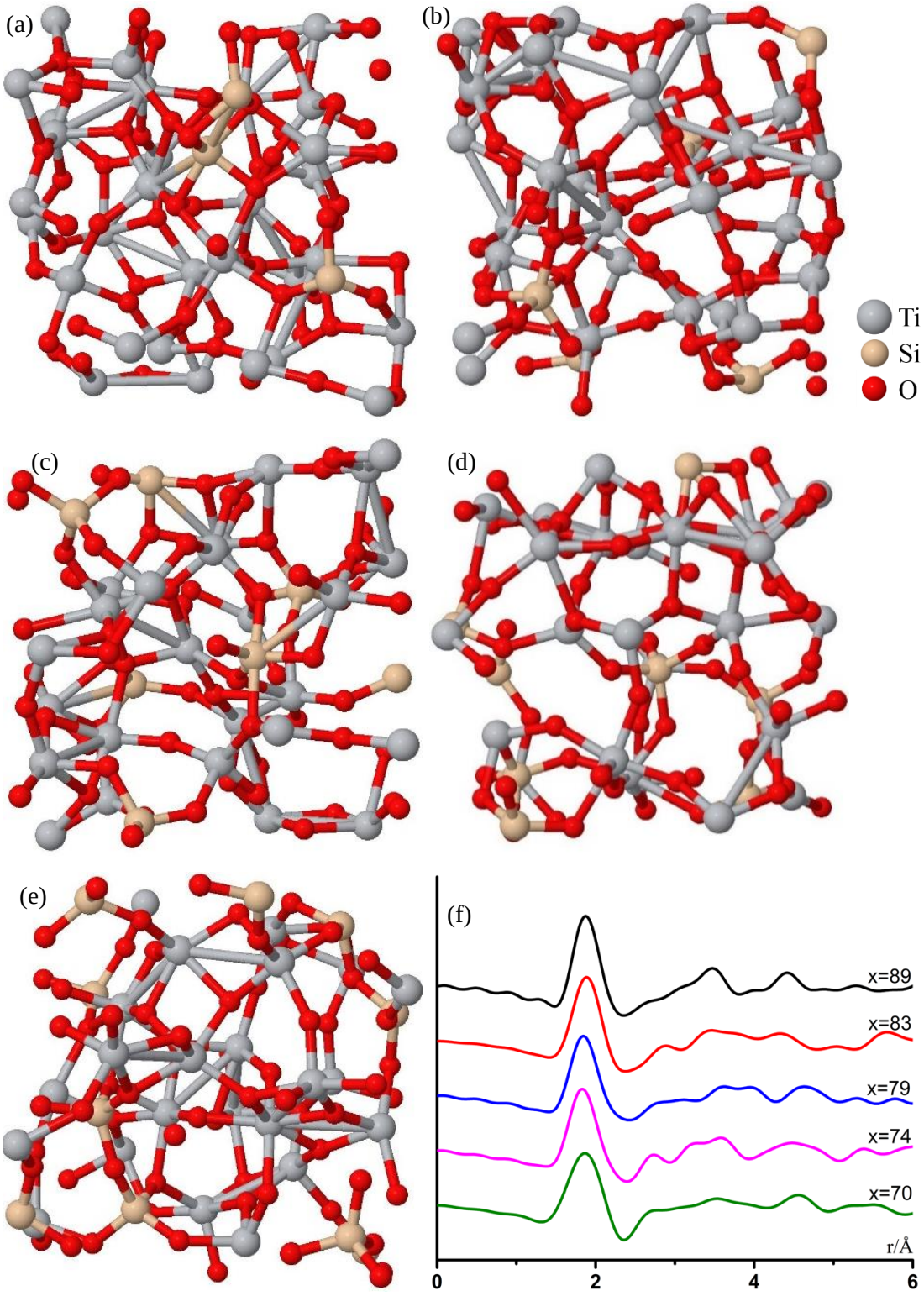


Figure 4.2.6 Simulated models of oxidised $Ti_{0.33x}Si_{33-0.33x}O_{66}$ metallic glasses, (a) x=89, (b) 83, (c) 79, (d) 74 and (e) 70, along with (f) their corresponding $G(\boldsymbol{r})$ curves.

It can be seen from Figure 4.2.5 (f) that there is no peak at 1.9Å in pure Ti-Si glasses, which confirms that the distance of 1.9Å comes from an oxidised Ti-Si system. Meanwhile, a small peak shift of the first peak of about 0.1Å is noticeable when the composition varies between x=74 and x=70 films. The first peak shifts toward shorter distances due to more presence of Si which has a smaller atomic covalent radius than Ti. For the oxidised models, it can be seen from Figure 4.2.6 (f) that the peak at around 1.9Å is due to the presence of Ti-O distances. Although the first peak does not shift with composition variations, the peak is broadened when the concentration of Ti decreases, which is due to the increased contribution from Si-O bonds at 1.6Å.

4.2.2.3 Characterisation of the Oxidation Level

From the pure and oxidised models and their corresponding $G(\boldsymbol{r})$ curves, a compositional fitting was applied to the experimental $G(\boldsymbol{r})$ using both pure and oxidised $G(\boldsymbol{r})$ curves. This provides an estimate of the percentages of the pure and oxidised models. The compositional fitting is based on a least square function approximation as described below,

First, by assuming E is the experimental $G(\boldsymbol{r})$ data, while A and B are compositions in proportions *a* and *b* gives.

$$\sum_i (E_i - aA_i - bB_i)^2 = min \tag{4.1}$$

Since $a + b = 1$, Equation 4.1 can be rewritten as

$$\sum_i (E_i - aA_i - (1-a)B_i)^2 = min \tag{4.2}$$

$$\sum_i (E_i - aA_i - B_i + aBi)^2 = min \tag{4.3}$$

Expanding then gives

$$\begin{aligned} {E_i}^2 - 2aA_iE_i - 2B_iE_i + 2aB_iE_i + a^2{A_i}^2 + 2aA_iB_i - 2a^2A_iB_i \\ + {B_i}^2 - 2a{B_i}^2 + a^2{B_i}^2 = min \end{aligned} \tag{4.4}$$

This functional contains a variable *a* where the solution can be found by equating the first derivative of the functional by *a* to zero

$$\frac{d\left(\sum_i({E_i}^2 - 2aA_iE_i - 2B_iE_i + 2aB_iE_i + a^2{A_i}^2 + 2aA_iB_i - 2a^2A_iB_i\right.}{da} = 0 \tag{4.5}$$

Solving this gives

$$-2A_iE_i + 2B_iE_i + 2aA_i{}^2 + 2A_iB_i - 4aA_iB_i - 2B_i{}^2 + 2aB_i{}^2 = 0 \quad (4.6)$$

Thus

$$aA_i{}^2 - 2aA_iB_i + aB_i{}^2 = A_iE_i - B_iE_i - A_iB_i + B_i{}^2 \quad (4.7)$$

and hence the value of *a* can be derived as

$$a = \frac{A_iE_i - B_iE_i - A_iB_i + B_i{}^2}{A_i{}^2 - 2A_iB_i + B_i{}^2} \quad (4.8)$$

Following Equation 4.8, by assuming A to be the contribution from pure Ti-Si and B as the contribution from the oxidised model, the results of fitting are shown in Figure 4.2.7 together with the contribution from the pure and oxidised models and the goodness of fit index, marked as P, O and R respectively for each fit.

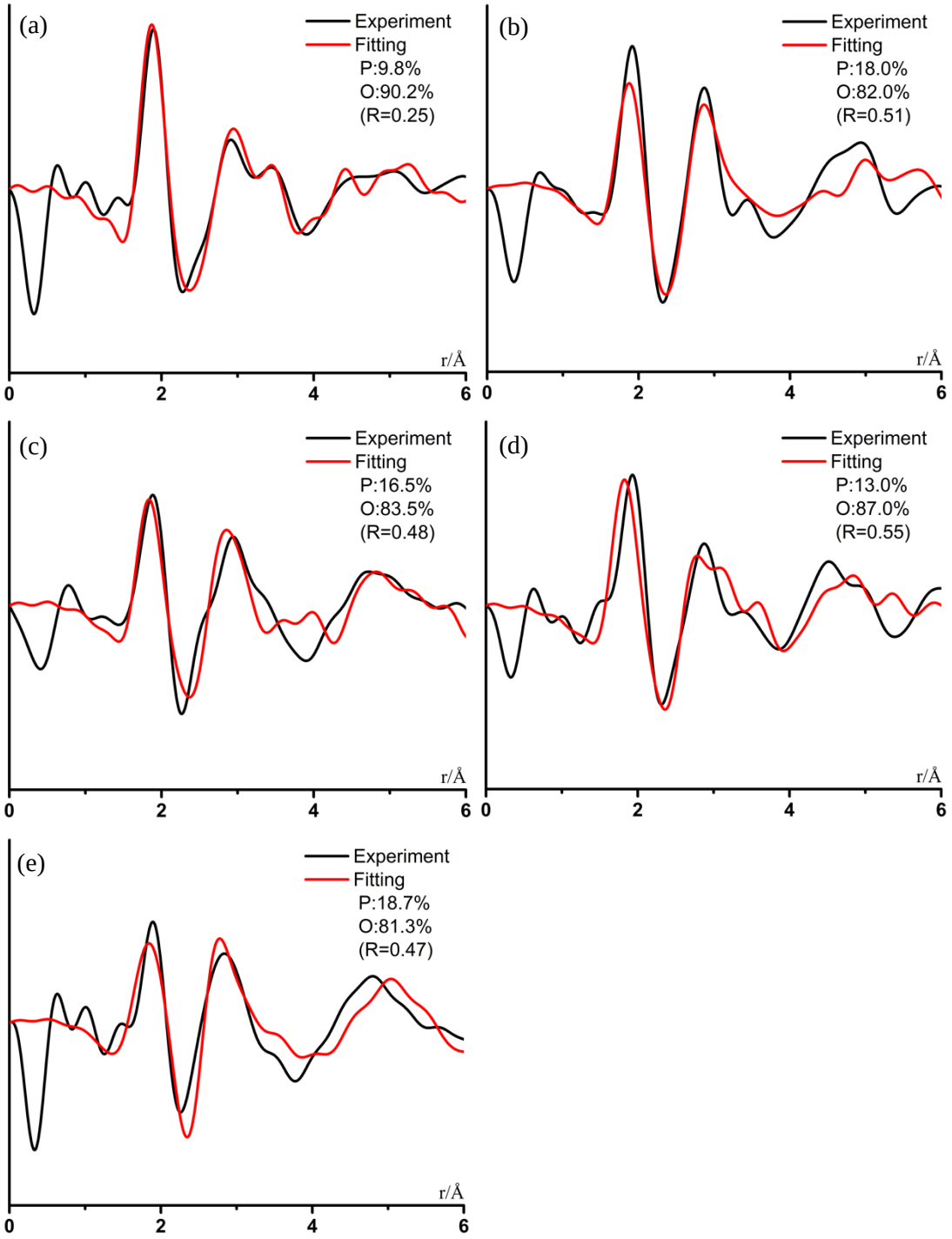


Figure 4.2.7 Compositional fitting to experimental data with $G(\boldsymbol{r})$ from simulated models. (a) x=89, (b) 83, (c) 79, (d) 74 and (e) 70,

It can be seen from Figure 4.2.7 that the fitted results show good agreements in the position of the 1st and 2nd peaks with all experimental $G(\boldsymbol{r})$. However, the simulated models were unable to be refined individually using the RMC process against the partially oxidised experimental data, resulting in a large R ranging from 0.25 to 0.55. In addition, films with x=89 and 74 show higher contributions, up to 90% from the oxidised model while films with x = 83, 79 and 70 show similar contributions from the oxidised model at around 80%. From the fitted contribution from both pure and oxidised models, the atomic compositions can be calculated as shown in Table 4.2.2. These results are compared with the EDS quantitative analysis and plotted in Figure 4.2.8.

Table 4.2.2 Atomic compositions calculated based on compositional fitting.

	$Ti_{89}Si_{11}$	$Ti_{83}Si_{17}$	$Ti_{79}Si_{21}$	$Ti_{74}Si_{26}$	$Ti_{70}Si_{30}$
Ti	36.1	38.2	35.0	31.7	32.1
Si	3.8	7.2	9.4	10.4	13.9
O	60.1	54.6	55.6	57.9	54.1
Ti: Si ratio	90:10	84:16	79:21	75:25	70:30

Unit: at%

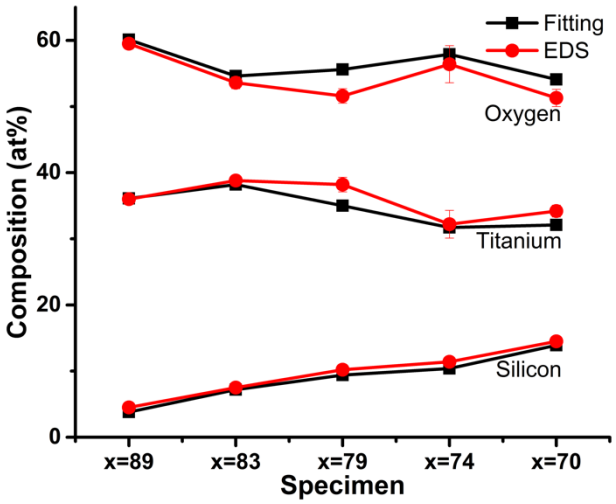


Figure 4.2.8 Comparison of atomic compositions measured using a quantitative EDS analysis (red) and compositional fitting (black).

Table 4.2.2 shows that the Ti: Si ratio is very close to the nominal Ti_xSi_{100-x} ratio with only 1at% difference, while the percentages of oxygen are more than 50at% for all films. Moreover, it can be seen from Figure 4.2.8 that the variation of silicon percentages in all films is less than 1at% while the error for titanium and oxygen is less than 4at% as compared to EDS results. Overall, the compositional fitting presents a similar trend and agrees well within an error of 5at% with the quantitative EDS analysis.

4.2.2.4 Construction of atomic models

Using the contributions from pure and oxidised models calculated in the previous section, atomic models of each film were built. To balance computational time and structural accuracy, models around 2nm along each direction were built. First, large cells were generated by duplicating the DFT simulated models along each direction. The duplicated cells were then cropped into the desired size based on their atomic ratios ($Ti_xSi_{100-x-y}O_y$) while maintaining charge balance of the model. Finally, the cropped models were stacked together into a sandwich structure with an oxidised layer on the top and the bottom. A spacing of 0.5Å was applied between each layer to prevent formation of unphysically short distances. The initial constructed models are shown in Figure 4.2.9 while their corresponding $G(\boldsymbol{r})$ curves plotted against experimental data shown in Figure 4.2.10.

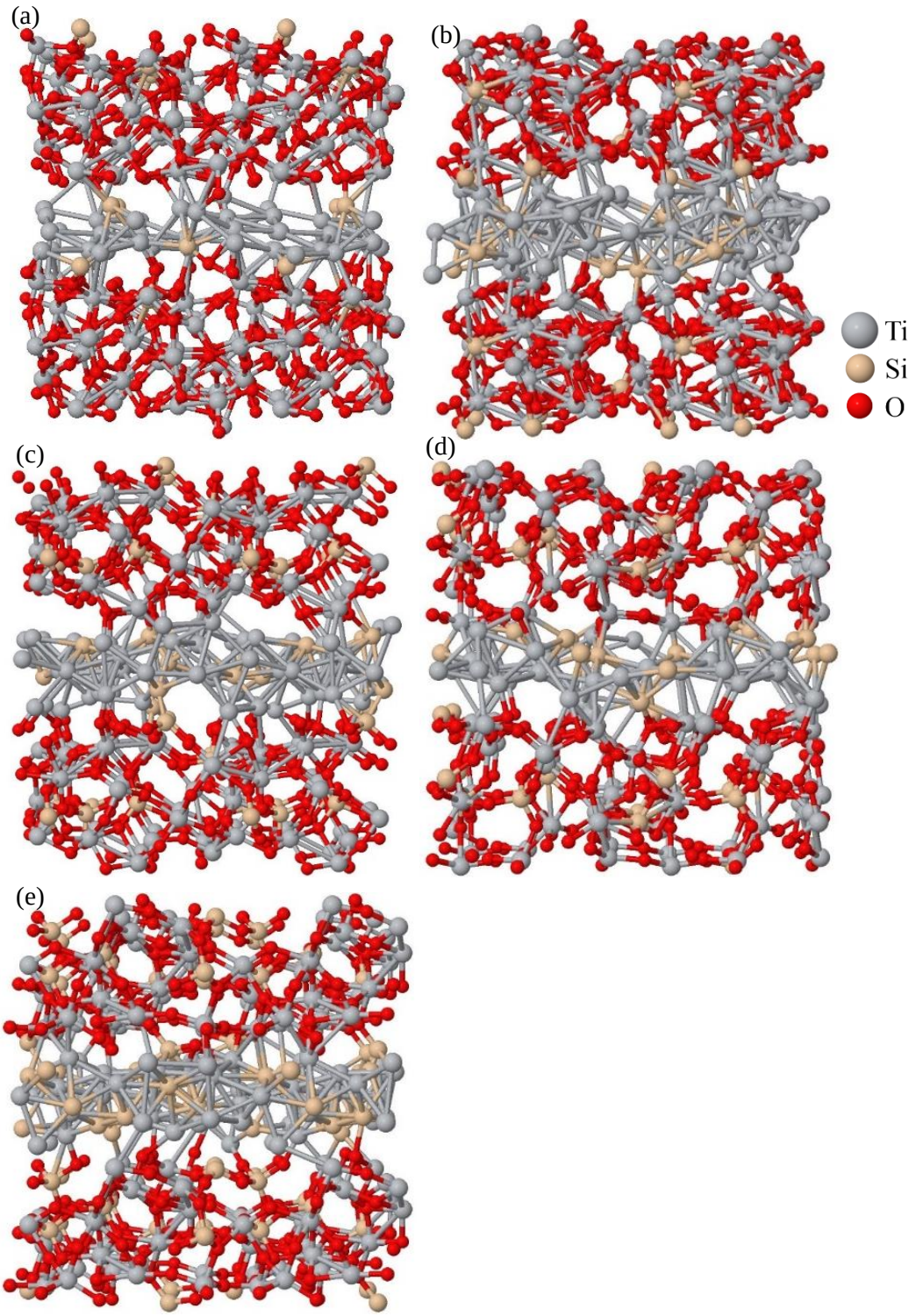


Figure 4.2.9 Initially constructed models of Ti_xSi_{100-x} oxidised metallic glasses, (a) x=89, (b) 83, (c) 79, (d) 74 and (e) 70.

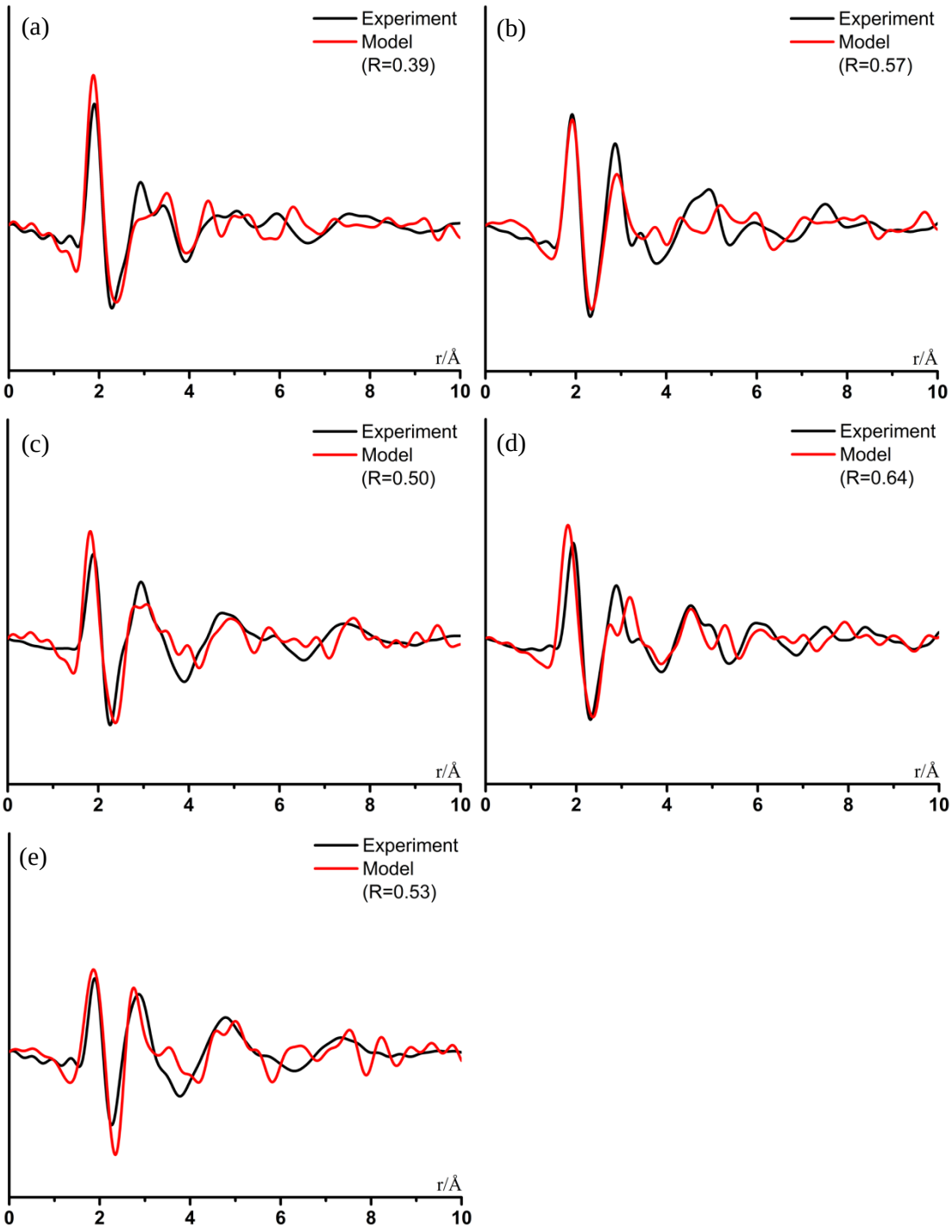


Figure 4.2.10 $G(\boldsymbol{r})$ curves of the initially constructed models shown in Figure 4.2.9. (a) x=89, (b) 83, (c) 79, (d) 74 and (e) 70.

Due to the nature of the DFT models, periodicity can be seen in the models as shown in Figure 4.2.9. Since the models are not refined and possibly due to this periodicity, the $G(\boldsymbol{r})$ curves do not fit well (R ranging from 0.39 to 0.64) with the experimental data. However, it can be seen that all $G(\boldsymbol{r})$ curves show agreement in the peak positions of the 1st and 2nd peaks. The initially constructed models were then refined using the RMC method and the resulting models along with their corresponding $G(\boldsymbol{r})$ curves are shown in Figure 4.2.11 and Figure 4.2.12 respectively.

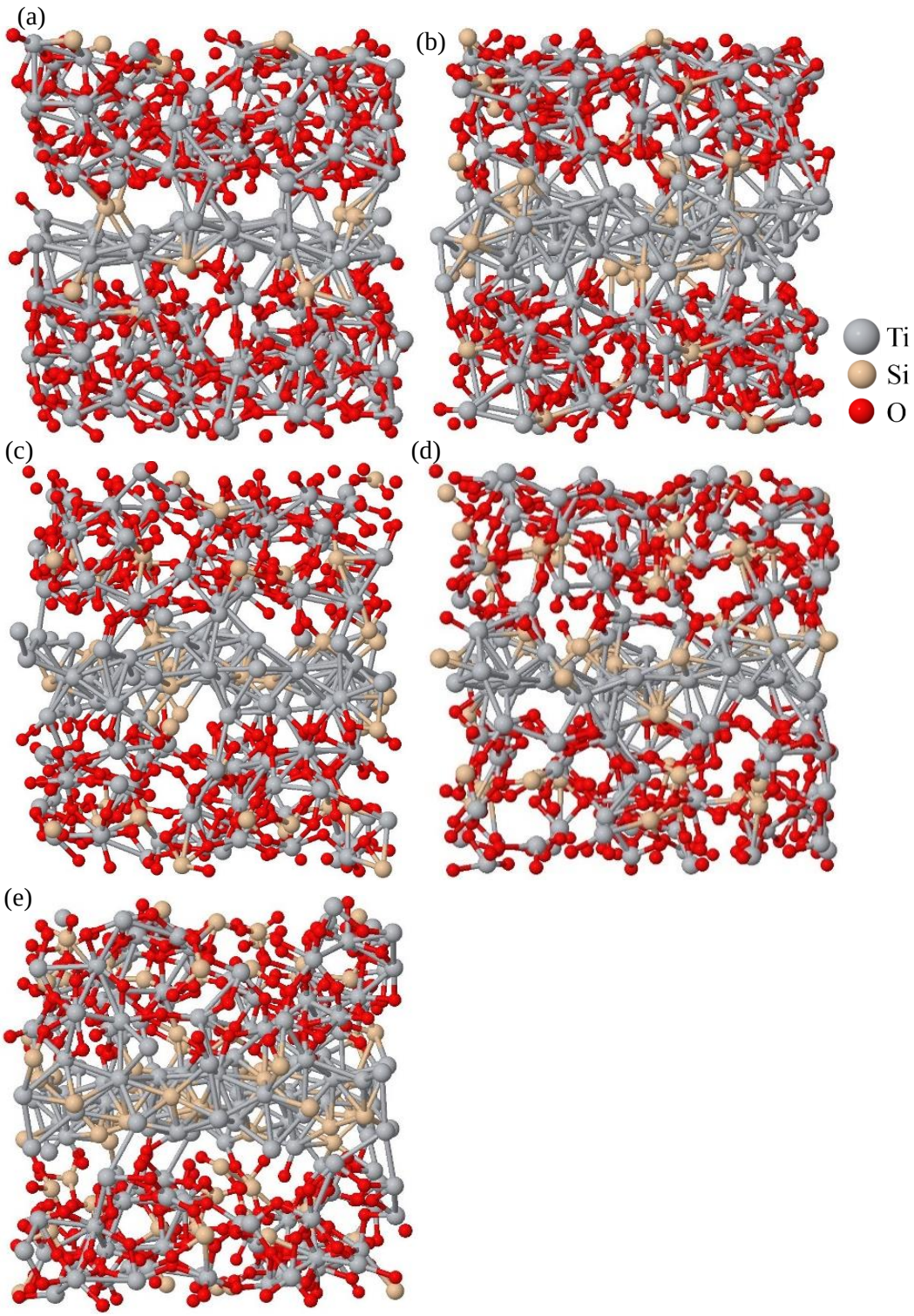


Figure 4.2.11 Refined models of Ti_xSi_{100-x} oxidised metallic glasses after RMC refinement. (a) x=89, (b) 83, (c) 79, (d) 74 and (e) 70.

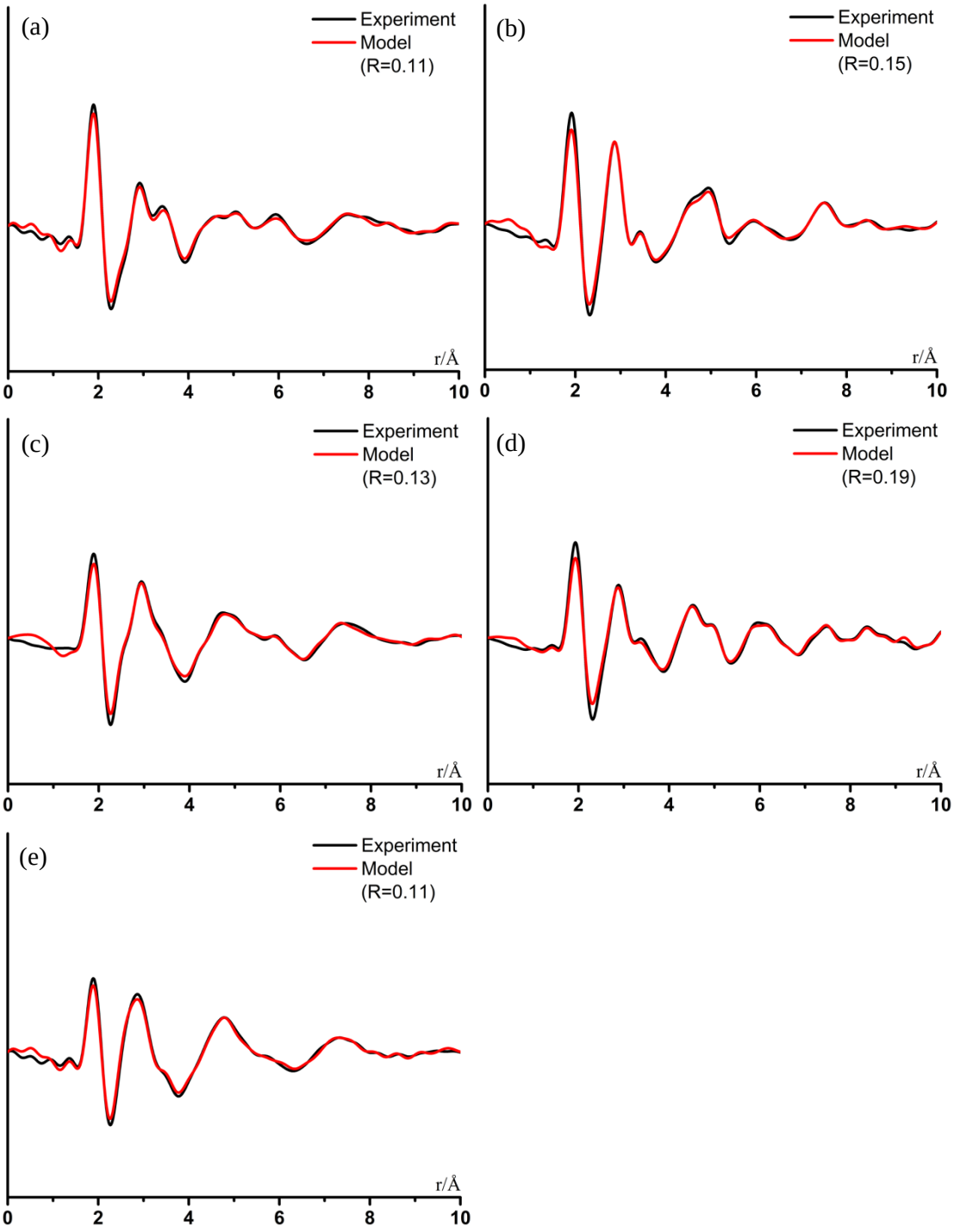


Figure 4.2.12 $G(\boldsymbol{r})$ curves of the refined models shown in Figure 4.2.11. (a) x=89, (b) 83, (c) 79, (d) 74 and (e) 70.

Comparison with the initially constructed models (Figure 4.2.9, Figure 4.2.11) shows the refined models where no periodicities are present. The resulting $G(\boldsymbol{r})$ curves in Figure 4.2.12 show improved agreement with the experimental data with R ranging from 0.11 to 0.19 which is a maximum 45% improvement as compared to the initially constructed models. A detailed comparison between bond angles and bond types for the refined models are shown in Figure 4.2.13.

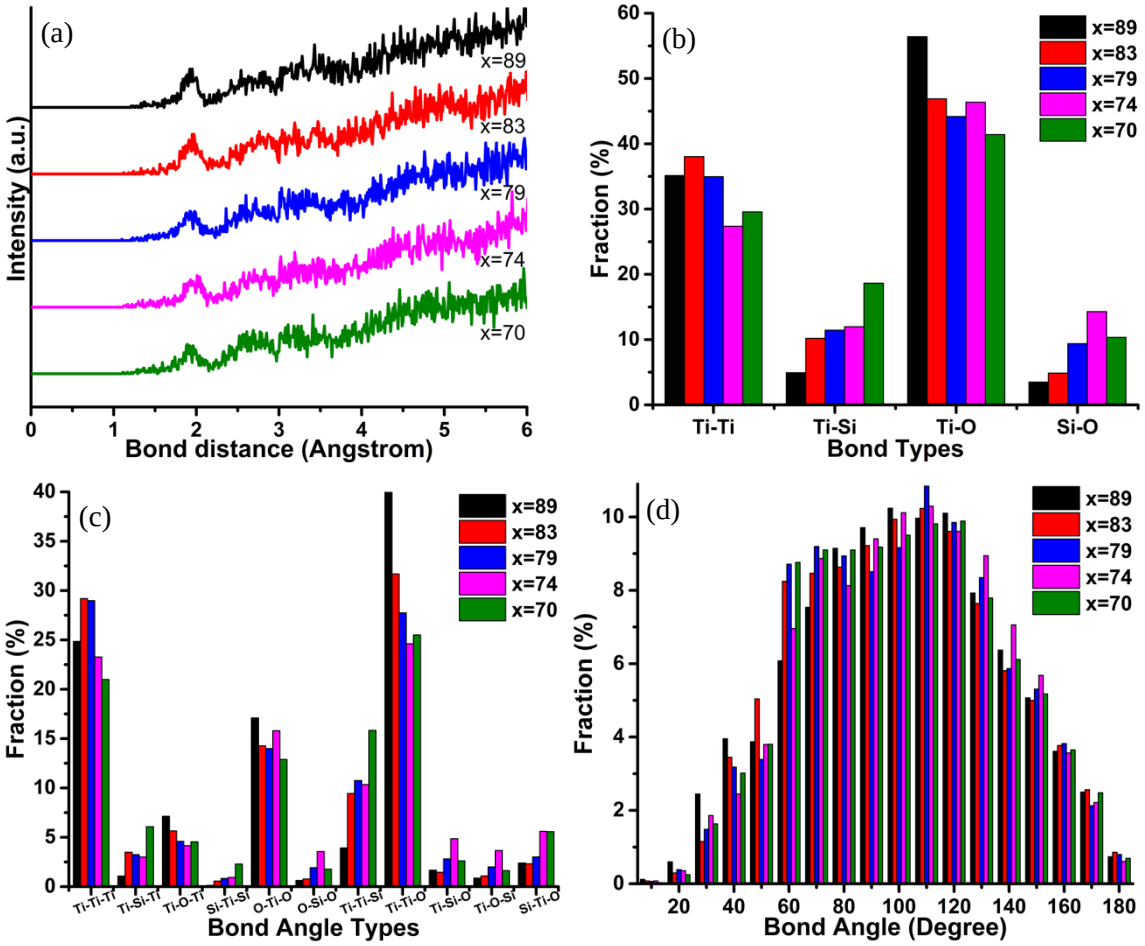


Figure 4.2.13 Comparison of all reconstructed models. (a) Bond distance distributions, (b) Bond distance types, (c) Bond angle types and (d) Bond angle distributions.

Bond distance distributions from the refined models are shown in Figure 4.2.13 (a). This data indicates a similar trend to the experimental $G(\boldsymbol{r})$ curves in that the first peak gets shorter and broader due to the decreased contribution from Ti-O bonds while the contribution from Si-O bonds is increased. Figure 4.2.13 (b) shows the bond type distributions of Ti-Ti, Ti-Si, Ti-O and Si-O bonds. These results demonstrate that films with x = 83, 79 and 70 show a similar trend based on their atomic composition owing to similar oxidation levels. However, due to the higher oxidation level in $Ti_{89}Si_{11}$ and $Ti_{74}Si_{26}$ films, both of these have more Ti-O bonds and less Ti-Ti and Ti-Si bonds. The bond angle type distributions are shown in Figure 4.2.13 (c) which show a similar trend to the bond type distributions, *i.e.* more Ti-O related angles such as O-Ti-O and Ti-Ti-O are found in x = 89 and 74 films while less Ti-Ti- and Ti-Si- related angles were observed. Finally, Figure 4.2.13 (d) shows the bond angle distributions for all specimens. It is clear that the distributions for the weakly oxidised specimens (x = 83, 79 and 70) are very similar with no more than a 2% difference. In contrast, the strongly oxidised specimens (x = 89 and 74) have fewer bond angles at 60-70 degrees which mainly arise from Ti-Ti-Ti angles. In addition, the $Ti_{89}Si_{11}$ glass shows more bond angles at 30-40 degrees which correspond to Ti-Ti-O distances while the $Ti_{74}Si_{26}$ glass shows more bond angles at 130-150 degrees due to Si-O- related bonds.

Using both experimental RDF analysis and DFT simulations, structural information from all five metallic glass specimens have been measured and atomic models have been proposed which show good agreement with the experimental data.

4.3 Summary of Key Findings

4.3.1 Bioactive Glasses

The analysis described leads to the following conclusions about the bioactive glass specimens.

(1) Nanobeam diffraction patterns of both BGs were captured on the edge of the sensor to achieve higher scattering intensities up to 18Å^{-1}. Due to the large sample thickness of up to 150nm, the RDF analysis resulted in poor $I(\boldsymbol{q})$ background fitting (R around 0.4). This affected the resulting $\varphi(\boldsymbol{q})$ and gave a large negative peak in the $G(\boldsymbol{r})$ curves. Therefore, a Fourier filter was applied to remove the negative peaks from the $G(\boldsymbol{r})$ curves caused by the poor background fitting.

(2) RDF analysis appears to be sufficiently sensitive to detect structural differences in bioactive glass particles with different compositions. The higher calcium oxide concentration in the 60SiO_2-35CaO-5P_2O_5 glass results in the appearance of a shoulder on the peak around 2.6Å. In contrast, the higher silicon oxide concentration in the 80SiO2-15CaO-5P_2O_5 glass results in higher peaks at 1.6 and 4.0Å corresponding to Si-O and Si…Si distances respectively.

(3) Atomic models have been constructed using DFT simulation. Models of both bioactive glasses were quenched from melt to room temperature with a cooling rate of $2\cdot10^{14}$K/s. The as-simulated amorphous models show similar trends to the

experimental data such as differences in the Si-O peak and the Ca…O shoulder. Using RMC refinements, final structural models were calculated for both bioactive glasses that showed good agreement to the experimental data.

(4) The bioactive tests carried out by by Prof. Shih and his colleague, show that the $60SiO_2$-$35CaO$-$5P_2O_5$ glass has a higher bioactivity with the ability to form hydroxyapatite after only 1h immersion in SBF. However, the $80SiO_2$-$15CaO$-$5P_2O_5$ glass shows limited growth of hydroxyapatite even after 12h of immersion. By comparing the structural data from both specimens, it is proposed that the higher bioactivity shown by the $60SiO_2$-$35CaO$-$5P_2O_5$ glass is due to the presence of more Ca…O distances acting as nucleation centres than in the $80SiO_2$-$15CaO$-$5P_2O_5$ glass which favours the precipitation of the hydroxyapatite phase at the surface.

4.3.2 Metallic Glasses

The following summarises the findings on the metallic glasses.

(1) Electron diffraction patterns of five metallic glass thin films were obtained and RDF analysis were performed with good $I(\boldsymbol{q})$ background fitting ($R < 0.3$) owing to their small thicknesses. However, all five films were found to be severely oxidised as demonstrated by the presence of a first peak at 1.9Å which corresponds to a Ti-O bonded distance.

(2) Quantitative analysis of EDS spectra confirmed that the abundance of oxygen in all films is more than 50at%. In addition, films of $Ti_{89}Si_{11}$ and $Ti_{74}Si_{26}$ showed higher oxidation of up to 59at% and 56at%. The RDF analysis of each film was performed with a refined composition which resulted in better background fitting (R improved by 2-3%) and more accurate $G(\boldsymbol{r})$ curves.

(3) To build atomic models, both pure and fully oxidised models were simulated using DFT for a best estimation of partially oxidised films. Simulated pure models showed an absence of the peak at 1.9Å while in the simulated oxidised models this peak is present which supports the oxidation of all Ti-Si films. In addition, compositional fitting was performed to estimate the contribution of pure and oxidised models to the experimental data. The results of this show that all films exhibit a contribution of up to 80% from the oxidised model with higher

contributions of 90% and 87% for $Ti_{89}Si_{11}$ and $Ti_{74}Si_{26}$ films. In addition, the atomic compositions derived from the fitted contributions of both models gave an error within 4% compared to the quantitative EDS analysis.

(4) Following compositional fitting, models for each film were constructed and the initially constructed models showed close agreement in the peak positions with the experimental data. RMC refinements were then carried out which resulted in final structural models with better agreements ($R < 0.2$) to the experimental data.

Chapter 5 Conclusions and Future Work

5.1 Conclusions

Amorphous materials have been used for many years in various application fields. Compared to the relatively clear understanding of the crystalline structure, the structure of amorphous materials remains elusive with no clear evidence demonstrating the exact structure. In Chapter 1, some industrial important components that are made of amorphous materials are listed and general methods for characterisation of amorphous materials are discussed. Among those methods, diffraction techniques are commonly used.

This thesis has explored the robustness of RDF analysis based on electron diffraction for studying amorphous structures. Chapter 2 is studies the effects of calculation parameters on the RDF. The results indicates that if the parameters show only small changes in the peak position and amplitude of the RDF curves are small. Chapter 3 examined the effects of several experimental factors on the RDF including sample thickness, noise, coherence and dose. The results show that sample thickness of up to 200Å is robust against multiple scattering with an error of less than 10%. It is also demonstrated that artefacts caused by noise can be removed by using an electron-counting detector. Variations in coherence length from 9 to 20Å along with different radiation conditions with a lowest dose of $10.76e^{-}/Å^{2}$ were examined and their influence on the RDF appears to also be negligible. From all the characterisations examined, the RDF analysis is demonstrated as a robust tool for studying amorphous materials.

Chapter 4 described the structural studies of two different amorphous materials, bioactive glasses and metallic glasses. The structures of SiO_2-CaO-P_2O_5-based bioactive glasses were characterised combining both experimental and simulation approaches. Through the examination of the structural information of the bioactive glasses, it is found that the structure of $60SiO_2$-35CaO-$5P_2O_5$ glasses is more favourable for the deposition of hydroxyapatite as compared to $80SiO_2$-15CaO-$5P_2O_5$ glasses. Finally, a structure-property correlation of bioactive glasses was proposed from their atomic models and bioactivities.

In the study of Ti-Si metallic glasses, the RDF analysis indicates an analytical capability showing that all specimens are partially oxidised. Moreover, with the help of DFT simulations, composition characterisation was demonstrated with less than 5% error compared to quantitative EDS analysis. Using both pure and oxidised models along with their compositions, the complex structures of partially oxidised Ti-Si metallic glasses were constructed.

To summarise, this thesis has demonstrated that the RDF analysis is a powerful technique and highly valuable for examining the structure of amorphous materials. In addition, its analytical capability provides accurate composition which also helps the construction of atomic models for complex structures.

5.2 Future Work

Although the influences of several experimental factors on the RDF analysis have been demonstrated in Chapter 3, there are some parts which require further work. For experiments, more thicknesses could be examined as well as additional degrees of coherence. In addition, other factors such as inelastic scattering were not tested. For simulations, the multislice method has proved its ability to extract RDF from the models with good agreements compared to the experiments. Therefore, this should be incorporated into the RMC refinement process to make the refined models more realistic when compared to the experimental data.

The structural information from bioactive glasses were characterised in Chapter 4 and a correlation with bioactive property was proposed. Similarly, it would be interesting to know how the structural information of other bioactive glasses produced using different methods compares with glasses prepared by spray pyrolysis.

I have demonstrated the construction of atomic models of a complex system using both experimental data and simulated models. However, the experimental data reveals average structural information which is not sufficient to study phase separation phenomenon present in some specimens. It would be interesting to perform fluctuation electron microscopy and combine this with modelling to gain a better understand of structure-property correlations.

References

[1] J. Senior, Optical fiber communications: Principles and practice, Prentice Hall International, (1992).

[2] B. Lee, Review of the present status of optical fiber sensors, Opt. Fiber Technol., 9 (2003) 57-79.

[3] K. Tanaka, K. Shimakawa, Chalcogenide glasses in japan: A review on photoinduced phenomena, Phys. Status Solidi B, 246 (2009) 1744-1757.

[4] D.P. San-Román-Alerigi, D.H. Anjum, Y. Zhang, X. Yang, A. Benslimane, T.K. Ng, M.N. Hedhili, M. Alsunaidi, B.S. Ooi, Electron irradiation induced reduction of the permittivity in chalcogenide glass (as2s3) thin film, J. Appl. Phys., 113 (2013) 044116.

[5] R.E. Simpson, FonsP, A.V. Kolobov, FukayaT, KrbalM, YagiT, TominagaJ, Interfacial phase-change memory, Nat Nano, 6 (2011) 501-505.

[6] V. Murthy, Structure and properties of engineering materials, Tata McGraw-Hill Education, (2003).

[7] T. Kokubo, S. Ito, Z.T. Huang, T. Hayashi, S. Sakka, T. Kitsugi, T. Yamamuro, Ca, p-rich layer formed on high-strength bioactive glass-ceramic a-w, J. Biomed. Mater. Res., 24 (1990) 331-343.

[8] L.L. Hench, R.J. Splinter, W.C. Allen, T.K. Greenlee, Bonding mechanisms at the interface of ceramic prosthetic materials, J. Biomed. Mater. Res., 5 (1971) 117-141.

[9] W.H. Zachariasen, The atomic arrangement in glass, J. Am. Chem. Soc., 54 (1932) 3841-3851.

[10] D.J. Gardiner, Introduction to raman scattering, Springer, 232 (1989).

[11] D. Tuschel, Why are the raman spectra of crystalline and amorphous solids different?, Spectroscopy, 32 (2017) 26-33.

[12] H. Maekawa, T. Maekawa, K. Kawamura, T. Yokokawa, The structural groups of alkali silicate glasses determined from 29si mas-nmr, J. Non-Cryst. Solids, 127 (1991) 53-64.

[13] W.J. Malfait, W.E. Halter, Y. Morizet, B.H. Meier, R. Verel, Structural control on bulk melt properties: Single and double quantum 29si nmr spectroscopy on alkali-silicate glasses, Geochim. Cosmochim. Ac., 71 (2007) 6002-6018.

[14] Q. Shabir, A. Pokale, A. Loni, D.R. Johnson, L.T. Canham, R. Fenollosa, M. Tymczenko, I. Rodríguez, F. Meseguer, A. Cros, A. Cantarero, Medically biodegradable hydrogenated amorphous silicon microspheres, Silicon, 3 (2011) 173-176.

[15] W.H. Bragg, W.L. Bragg, The reflection of x-rays by crystals, P. Roy. Soc. Lond. A Mat., 88 (1913) 428-438.

[16] N.W. Ashcroft, N.D. Mermin, Solid state physics, Saunders College Philadelphia, (1976).

[17] E.J. Kirkland, Advanced computing in electron microscopy, Springer Science & Business Media, (2010).

[18] P.J. Goodhew, J. Humphreys, R. Beanland, Electron microscopy and analysis, CRC Press, (2000).

[19] B.D. Williams, C.B. Carter, The transmission electron microscope, Springer US, (1996) 3-17.

[20] P. Debye, The scattering of x-rays, J. Math. Phys., 4 (1925) 113.

[21] B.E. Warren, X-ray diffraction, Courier Dover Publications, (1969).

[22] D.J.H. Cockayne, The study of nanovolumes of amorphous materials using electron scattering, Ann. Rev. Mater. Res., 37 (2007) 159-187.

[23] D.J.H. Cockayne, D.R. McKenzie, Electron diffraction analysis of polycrystalline and amorphous thin films, Acta Crystallogr. A, 44 (1988) 870-878.

[24] M. Affatigato, Modern glass characterization, John Wiley & Sons (2015).

[25] C.W.B. Grigson, On scanning electron diffraction†, J. Electron. Control, 12 (1962) 209-232.

[26] S.C. Moss, J.F. Graczyk, Evidence of voids within the as-deposited structure of glassy silicon, Phys. Rev. Lett., 23 (1969) 1167.

[27] J.F. Graczyk, S.C. Moss, Scanning electron diffraction attachment with electron energy filtering, Rev. Sci. Instrum., 40 (1969) 424-433.

[28] D.J.H. Cockayne, D.R. McKenzie, D. Muller, Electron diffraction of amorphous thin films using peels, Microsc. Microanal. Microstruct., 2 (1991) 359-366.

[29] D. Heinemann, W. Mader, Electron scattering experiments using a post-column imaging electron energy filter, Ultramicroscopy, 74 (1998) 113-122.

[30] R.L. Mozzi, B.E. Warren, The structure of vitreous silica, J. Appl. Crystallogr., 2 (1969) 164-172.

[31] W.E. McBride, D.J.H. Cockayne, C.M. Goringe, Reduced density function analysis using convergent electron illumination and iterative blind deconvolution, Ultramicroscopy, 76 (1999) 115-123.

[32] W. McBride, D.J.H. Cockayne, K. Tsuda, Deconvolution of electron diffraction patterns of amorphous materials formed with convergent beam, Ultramicroscopy, 94 (2003) 305-308.

[33] N. Mori, T. Oikawa, T. Katoh, J. Miyahara, Y. Harada, Application of the "imaging plate" to tem image recording, Ultramicroscopy, 25 (1988) 195-201.

[34] W. McBride, D.J.H. Cockayne, D. Nguyen-Manh, Electron diffraction from nanovolumes of amorphous material using coherent convergent illumination, Ultramicroscopy, 96 (2003) 191-200.

[35] M.E. Barnett, Image formation in optical and electron transmission microscopy, J. Microscopy, 102 (1974) 1-28.

[36] E. Hecht, A. Zajac, Optics, Addison-Wesley, (1974).

[37] G.R. Anstis, Z. Liu, M. Lake, Investigation of amorphous materials by electron diffraction - the effects of multiple scattering, Ultramicroscopy, 26 (1988) 65-69.

[38] T.C. Petersen, W. McBride, D.G. McCulloch, I.K. Snook, I. Yarovsky, Refinements in the collection of energy filtered diffraction patterns from disordered materials, Ultramicroscopy, 103 (2005) 275-283.

[39] D.R. McKenzie, D. Muller, B.A. Pailthorpe, Z.H. Wang, E. Kravtchinskaia, D. Segal, P.B. Lukins, P.D. Swift, P.J. Martin, G. Amaratunga, P.H. Gaskell, A. Saeed, Properties of tetrahedral amorphous carbon prepared by vacuum arc deposition, Diam. Relat. Mater., 1 (1991) 51-59.

[40] D.G. McCulloch, D.R. McKenzie, C.M. Goringe, D.J.H. Cockayne, W. McBride, D.C. Green, Experimental and theoretical characterization of structure in thin disordered films, Acta Crystallogr. A, 55 (1999) 178-187.

[41] Y.G. Shen, Y.W. Mai, Structural studies of amorphous and crystallized tungsten nitride thin films by efed, xrd and tem, Appl. Surf. Sci., 167 (2000) 59-68.

[42] Y. Hirotsu, T. Ohkubo, I.T. Bae, M. Ishimaru, Electron diffraction structure analysis for amorphous materials, Mater. Chem. Phys., 81 (2003) 360-363.

[43] J. Shanmugam, K.B. Borisenko, Y.-J. Chou, A.I. Kirkland, Erdf analyser: An interactive gui for electron reduced density function analysis, SoftwareX, 6 (2017) 185-192.

[44] R. Kaplow, S.L. Strong, B.L. Averbach, Radial density functions for liquid mercury and lead, Phys. Rev., 138 (1965) A1336-A1345.

[45] J.H. Konnert, J. Karle, The computation of radial distribution functions for glassy materials, Acta Crystallogr. A, 29 (1973) 702-710.

[46] P.A. Doyle, P.S. Turner, Relativistic hartree-fock x-ray and electron scattering factors, Acta Crystallogr. A, 24 (1968) 390-397.

[47] I. Lobato, D. Van Dyck, A complete comparison of simulated electron diffraction patterns using different parameterizations of the electron scattering factors, Ultramicroscopy, 155 (2015) 11-19.

[48] A. Weickenmeier, H. Kohl, Computation of absorptive form factors for high-energy electron diffraction, Acta Crystallogr. A, 47 (1991) 590-597.

[49] L.-M. Peng, G. Ren, S.L. Dudarev, M.J. Whelan, Robust parameterization of elastic and absorptive electron atomic scattering factors, Acta Crystallogr. A, 52 (1996) 257-276.

[50] S.J. Clark, M.D. Segall, C.J. Pickard, P.J. Hasnip, M.I. Probert, K. Refson, M.C. Payne, First principles methods using castep, Z. Krist.-Cryst. Mater., 220 (2005) 567-570.

[51] J.P. Perdew, K. Burke, M. Ernzerhof, Generalized gradient approximation made simple, Phys. Rev. Lett., 77 (1996) 3865-3868.

[52] G.J. Martyna, M.L. Klein, M. Tuckerman, Nosé–hoover chains: The canonical ensemble via continuous dynamics, J. Chem. Phys., 97 (1992) 2635-2643.

[53] R.L. McGreevy, Reverse monte carlo modelling, J. Phys.: Condens. Mat., 13 (2001) R877.

[54] T. Malis, S.C. Cheng, R.F. Egerton, Eels log-ratio technique for specimen-thickness measurement in the tem, J. Electron Micr. Tech., 8 (1988) 193-200.

[55] J.M. Cowley, A.F. Moodie, The scattering of electrons by atoms and crystals. I. A new theoretical approach, Acta Crystallogr., 10 (1957) 609-619.

[56] P. Goodman, A.F. Moodie, Numerical evaluations of n-beam wave functions in electron scattering by the multi-slice method, Acta Crystallogr. A, 30 (1974) 280-290.

[57] S. Le Roux, V. Petkov, Isaacs - interactive structure analysis of amorphous and crystalline systems, J. Appl. Crystallogr., 43 (2010) 181-185.

[58] J.M. Cowley, Electron diffraction techniques, Oxford University Press, 1 (1992).

[59] R.F. Egerton, Control of radiation damage in the tem, Ultramicroscopy, 127 (2013) 100-108.

[60] R.M. Glaeser, Limitations to significant information in biological electron microscopy as a result of radiation damage, J. Ultra. Mol. Struct. R., 36 (1971) 466-482.

[61] C. Huang, K.B. Borisenko, A.I. Kirkland, Exit wave reconstruction of radiation-sensitive materials from low-dose data, Journal of Physics: Conference Series, 522 (2014) 012052.

[62] L.L. Hench, J.M. Polak, Third-generation biomedical materials, Science, 295 (2002) 1014-1017.

[63] S. Hulbert, J. Bokros, L.L. Hench, J. Wilson, G. Heimke, Ceramics in clinical applications, past, present and future, High Tech Ceramics.(Part A), (1986) 189-213.

[64] L.L. Hench, Biomaterials: A forecast for the future, Biomaterials, 19 (1998) 1419-1423.

[65] J.-M. Bouler, R.Z. LeGeros, G. Daculsi, Biphasic calcium phosphates: Influence of three synthesis parameters on the ha/ß-tcp ratio, J. Biomed. Mater. Res., 51 (2000) 680-684.

[66] L. Grover, J. Knowles, G. Fleming, J. Barralet, In vitro ageing of brushite calcium phosphate cement, Biomaterials, 24 (2003) 4133-4141.

[67] T. Kokubo, S. Ito, S. Sakka, T. Yamamuro, Formation of a high-strength bioactive glass-ceramic in the system mgo-cao-sio2-p2o5, J. Mater. Sci., 21 (1986) 536-540.

[68] L.L. Hench, Bioactive ceramics: Theory and clinical applications, Bioceramics, 7 (1994) 3-14.

[69] J. Sun, Y. Li, L. Li, W. Zhao, L. Li, J. Gao, M. Ruan, J. Shi, Functionalization and bioactivity in vitro of mesoporous bioactive glasses, J. Non-Cryst. Solids, 354 (2008) 3799-3805.

[70] C.J. Shih, H.T. Chen, L.F. Huang, P.S. Lu, H.F. Chang, I.L. Chang, Synthesis and in vitro bioactivity of mesoporous bioactive glass scaffolds, Mater. Sci. Eng. C, 30 (2010) 657-663.

[71] L.L. Hench, Bioceramics: From concept to clinic, J. Am. Ceram. Soc., 74 (1991) 1487-1510.

[72] D.M. Sanders, L.L. Hench, Mechanisms of glass corrosion, J. Am. Ceram. Soc., 56 (1973) 373-377.

[73] A.E. Clark, C.G. Pantano, L.L. Hench, Auger spectroscopic analysis of bioglass corrosion films, J. Am. Ceram. Soc., 59 (1976) 37-39.

[74] K. de Groot, Bioceramics of calcium phosphate, J. Clin. Eng., 9 (1984) 52.

[75] M. Vallet-Regí, Ceramics for medical applications, J. Chem. Soc. Dalton, (2001) 97-108.

[76] R. Li, A. Clark, L.L. Hench, An investigation of bioactive glass powders by sol-gel processing, J. Appl. Biomater., 2 (1991) 231-239.

[77] W. Xia, J. Chang, Well-ordered mesoporous bioactive glasses (mbg): A promising bioactive drug delivery system, J. Control. Release, 110 (2006) 522-530.

[78] S.-J. Shih, Y.-J. Chou, I.-C. Chien, One-step synthesis of bioactive glass by spray pyrolysis, J. Nanopart. Res., 14 (2012) 1-8.

[79] G.L. Messing, S.-C. Zhang, G.V. Jayanthi, Ceramic powder synthesis by spray pyrolysis, J. Am. Ceram. Soc., 76 (1993) 2707-2726.

[80] T. Kokubo, Surface chemistry of bioactive glass-ceramics, J. Non-Cryst. Solids, 120 (1990) 138-151.

[81] A.L. Greer, E. Ma, Bulk metallic glasses: At the cutting edge of metals research, MRS Bull., 32 (2011) 611-619.

[82] J. Eckert, J. Das, S. Pauly, C. Duhamel, Mechanical properties of bulk metallic glasses and composites, J. Mater. Res., 22 (2011) 285-301.

[83] C.A. Schuh, T.C. Hufnagel, U. Ramamurty, Mechanical behavior of amorphous alloys, Acta Mater., 55 (2007) 4067-4109.

[84] C.J. Gilbert, R.O. Ritchie, W.L. Johnson, Fracture toughness and fatigue-crack propagation in a zr–ti–ni–cu–be bulk metallic glass, Appl. Phys. Lett., 71 (1997) 476-478.

[85] W. Klement Jun, R.H. Willens, P.O.L. Duwez, Non-crystalline structure in solidified gold-silicon alloys, Nature, 187 (1960) 869.

[86] P. Duwez, R.H. Willens, R.C. Crewdson, Amorphous phase in palladium-silicon alloys, J. Appl. Phys., 36 (1965) 2267-2269.

[87] H.S. Chen, Thermodynamic considerations on the formation and stability of metallic glasses, Acta Metall. Mater., 22 (1974) 1505-1511.

[88] A. Inoue, H.M. Kimura, T. Masumoto, C. Suryanarayana, A. Hoshi, Superconductivity of ductile ti-nb-si amorphous alloys, J. Appl. Phys., 51 (1980) 5475-5482.

[89] A. Takeuchi, A. Inoue, Classification of bulk metallic glasses by atomic size difference, heat of mixing and period of constituent elements and its application to characterization of the main alloying element, Mater. Trans., 46 (2005) 2817-2829.

[90] A. Inoue, Amorphous, quasicrystalline and nanocrystalline alloys in al- and mg-based systems, Elsevier, 24 (1997) 83-219.

[91] X.H. Lin, W.L. Johnson, Formation of ti–zr–cu–ni bulk metallic glasses, J. Appl. Phys., 78 (1995) 6514-6519.

[92] A. Inoue, J.S. Gook, Fe-based ferromagnetic glassy alloys with wide supercooled liquid region, Mater. Trans. JIM, 36 (1995) 1180-1183.

[93] T. Zhang, A. Inoue, Thermal and mechanical properties of ti-ni-cu-sn amorphous alloys with a wide supercooled liquid region before crystallization, Mater. Trans. JIM, 39 (1998) 1001-1006.

[94] A. Peker, W.L. Johnson, A highly processable metallic glass: $Zr_{41.2}ti_{13.8}cu_{12.5}ni_{10.0}be_{22.5}$, Appl. Phys. Lett., 63 (1993) 2342-2344.

[95] A. Inoue, A. Takeuchi, Recent development and application products of bulk glassy alloys, Acta Mater., 59 (2011) 2243-2267.

[96] A. Inoue, Stabilization of metallic supercooled liquid and bulk amorphous alloys, Acta Mater., 48 (2000) 279-306.

[97] Z.P. Lu, C.T. Liu, A new glass-forming ability criterion for bulk metallic glasses, Acta Mater., 50 (2002) 3501-3512.

[98] T. Egami, Universal criterion for metallic glass formation, Mater. Sci. Eng. A, 226-228 (1997) 261-267.

[99] S. Hata, K. Sato, A. Shimokohbe, Fabrication of thin film metallic glass and its application to microactuators, Asia Pacific Symposium on Microelectronics and MEMS, 3892 (1999) 12.

[100] P. Sharma, W. Zhang, K. Amiya, H. Kimura, A. Inoue, Nanoscale patterning of zr-al-cu-ni metallic glass thin films deposited by magnetron sputtering, J. Nanosci. NanoTechno., 5 (2005) 416-420.

[101] M. Nastasi, F.W. Saris, L.S. Hung, J.W. Mayer, Stability of amorphous cu/ta and cu/w alloys, J. Appl. Phys., 58 (1985) 3052-3058.

[102] L. Yongdong, H. Seiichi, W. Kouichi, S. Akira, Thermal, mechanical and electrical properties of pd-based thin-film metallic glass, Jpn. J. Appl. Phys., 40 (2001) 5382.

[103] D. Rhinow, W. Kühlbrandt, Electron cryo-microscopy of biological specimens on conductive titanium–silicon metal glass films, Ultramicroscopy, 108 (2008) 698-705.

[104] C.J. Chen, J.C. Huang, H.S. Chou, Y.H. Lai, L.W. Chang, X.H. Du, J.P. Chu, T.G. Nieh, On the amorphous and nanocrystalline zr–cu and zr–ti co-sputtered thin films, J. Alloy Compd., 483 (2009) 337-340.

[105] G. Cliff, G.W. Lorimer, The quantitative analysis of thin specimens, J. Microscopy, 103 (1975) 203-207.